University of California
Santa Barbara

Eroding Uncertainty: Towards Understanding Flows Interacting with Mobile Sediment Beds Using Grain-Resolving Simulations

A dissertation submitted in partial satisfaction
of the requirements for the degree

Doctor of Philosophy
in
Mechanical Engineering

by

Edward Kristopher Biegert

Committee in charge:

Professor Eckart Meiburg, Chair
Professor Frédéric Gibou
Professor Matthew Helgeson
Professor Paolo Luzzatto-Fegiz

March 2018

The Dissertation of Edward Kristopher Biegert is approved.

Professor Frédéric Gibou

Professor Matthew Helgeson

Professor Paolo Luzzatto-Fegiz

Professor Eckart Meiburg, Committee Chair

March 2018

Eroding Uncertainty:

Towards Understanding Flows Interacting with Mobile Sediment Beds Using Grain-Resolving Simulations

by

Edward Kristopher Biegert

This work is dedicated to:

My family, who have always stood behind me

Eckart, who has supported me

Bernhard, who has guided me

My friends, who have filled my life with joy

Acknowledgements

This work was made possible only through the help and support of many other people. I would like to thank my advisor, Eckart Meiburg, who has given me so many opportunities as a graduate student, from learning and networking at workshops and conferences to participating in departmental functions to enjoying team-building outdoor excursions. I have been very fortunate to have an advisor who cares about these other aspects of graduate studies, beyond simply doing research. His patience, support, and encouragement have gotten me to where I am today, as well as to La Cumbre Peak, Mt. Whitney Peak, and through the Grand Canyon in the middle of August.

I would also like to thank Bernhard Vowinckel, who was always there to provide words of encouragement and guidance towards solutions whenever I faced difficult problems. I also am thankful for all the help and motivation Mohamad "Momo" Nasr-Azadani gave me in my early years. I have had the best labmates a grad student could ask for. Almost every day, I looked forward to coming into lab to be with a great group of people who could spontaneously engage in stimulating research discussions or entertain with the latest Youtube videos.

My family has been the solid foundation upon which I stand. They gave me the education and morals that made me who I am today, and their love and support have always kept me firmly on my feet. They knew when to stop asking me when I would graduate and how to welcome me home with open arms. I love them for all the love they have given me.

I have also had wonderful friends, from Santa Barbara, from Rice University, and earlier. They have provided a welcome respite from my studies, have been great companions, and have given me truly enjoyable experiences over the last few years. Without them, I would not have traveled to Peru, climbed snow shutes in the Sierra Nevada, or

seen the Channel Island foxes. Through them, I found the energy and motivation to work through the toughest research problems.

I would like to thank my dissertation committee members, who provided valuable feedback during my candidacy exam and who I enjoy having the occasional spontaneous conversation with in the hallway. I also appreciate the time É. Guazelli took to discuss particle-laden flow rheology with me and thank her for sharing experimental data. I similarly enjoyed my stimulating discussions with J. Jenkins. I would also like to thank P. Gondret, N. Mordant, and A. Ten Cate for their prompt responses and for kindly providing their experimental data.

I would also like to thank Dr. Ping Ge and the ORISE team for all their help and support with the Department of Energy (DOE) Office of Science Graduate Fellowship Program (DOE SCGF). I am very thankful and honored to have been able to participate in this program, which helped fund my research for three years, taught me about the national labs, and allowed me to make new friends/contacts at other graduate programs around the country. Dr. Ge and the ORISE team were instrumental in making the whole experience a positive one. The DOE SCGF Program was made possible in part by the American Recovery and Reinvestment Act of 2009. The DOE SCGF program is administered by the Oak Ridge Institute for Science and Education for the DOE. ORISE is managed by Oak Ridge Associated Universities (ORAU) under DOE contract number DE-AC05-06OR23100. All opinions expressed in this document are mine and do not necessarily reflect the policies and views of DOE, ORAU, or ORISE.

My work was also supported by the Petroleum Research Fund, administered by the American Chemical Society, grant number 54948-ND9. Computational resources for this work used the National Energy Research Scientific Computing Center, which is supported by the Office of Science of the U.S. Department of Energy under Contract No. DE-AC02-05CH11231, as well as the Extreme Science and Engineering Discovery

Environment (XSEDE), which was supported by the National Science Foundation, USA, Grant No. TG-CTS150053.

Curriculum Vitæ

Edward Kristopher Biegert

Education

2018	Ph.D. in Mechanical Engineering (Expected), University of California, Santa Barbara.
2011	B.S. in Mechanical Engineering, Rice University.

Publications

E. Biegert, B. Vowinckel, and E. Meiburg, *High-resolution simulations of turbidity currents*, *Progress in Earth and Planetary Science* **4** (dec, 2017) no. 1 33.

E. Biegert, B. Vowinckel, and E. Meiburg, *A collision model for grain-resolving simulations of flows over dense, mobile, polydisperse granular sediment beds*, *Journal of Computational Physics* **340** (jul, 2017) 105–127.

Abstract

Eroding Uncertainty:

Towards Understanding Flows Interacting with Mobile Sediment Beds Using Grain-Resolving Simulations

by

Edward Kristopher Biegert

Dense particle-laden flows play an important role in many environmental processes, including the shaping of rivers and the formation of landslides. Despite decades of study, researchers have not been able to accurately predict the onset of erosion and the amount of sediment transported by flows, due in part to the difficulty in measuring dense particle-laden flows. Highly-resolved numerical simulations, on the other hand, allow us to study the physics of particle-fluid and particle-particle interactions in much more detail.

We develop a code to accurately simulate dense, polydisperse, particle-laden flows as well as methods by which to analyze them. The code solves the Navier-Stokes equations for the fluid phase and resolves the flow around each individual particle using an immersed boundary method. We also develop a collision model to accurately resolve particle-particle interactions within the fluid. We then perform simulations of a pressure-driven flow over a bed of spherical particles that agree with experimental results for particle velocities and flow rates. Using a control volume momentum balance, we analyze fluid and particle stresses within the simulations, which reveal the mechanisms by which the particle bed expands and contracts during changes in flow rates. These same stresses also allow us to measure the rheology of the particle-laden flows, where we find some agreement with existing constitutive models but also reveal the need to develop these models further.

Contents

Chapter 1

Introduction

The flow over dense, mobile granular beds plays a central role in multiple applications in environmental, mechanical, and process engineering. Prime examples include turbidity currents and powder snow avalanches, for which resuspension of particles essentially determines the dynamics of the flow [1], and fluvial systems, in which erosion and deposition can change the shapes of rivers and estuaries [2]. These flows also play a role in the formation of landslides [3]. Of key importance to a quantitative understanding of these systems is the ability to predict when the sediment bed will start to move, how much sediment is entrained into the flow above, and at what rate the sediment is transported downstream. Identifying a rheology to describe these fluid/particle mixtures can help answer these questions as well as improve models for these flows [4, 5, 6]. Historically, models for sediment entrainment [7, 8] and transport [9, 10] have depended on the resuspension threshold, quantified by the Shields number [11], which is the ratio of the hydrodynamic drag force to the weight of the particle. The critical Shields parameter, however, has proven to be a poor predictor for the onset of particle erosion [12], and substantial efforts have been made in hydraulic engineering to overcome this difficulty [2]. Progress has been slow, in part due to experimental difficulties of measuring

dense particle-laden flows [13]. Advances in index-matching techniques and numerical simulations, however, have shed new light on the field.

Recently, many researchers have focussed their efforts on developing constitutive models to describe the particle phase or the fluid/particle mixture as a continuum. Descriptions include kinetic theory for turbulent flows with energetic particle collisions [14, 15] and continuum modeling for laminar shear flows [16] and turbulent flows [5]. With correct models accounting for fluid-particle and particle-particle interactions, these equations can predict e.g. the amount of sediment mobilized into the fluid and transported downstream. Furthermore, experiments using index-matched particles, fluorescent dye, and laser sheets have enabled researchers to probe the velocities of fluid and particles deep within the particle bed [17, 18, 19, 20]. In particular, Aussillous et al. [19] demonstrated the potential for constitutive models to predict experimental data, but they also demonstrated the shortcomings of rheological models for fluid/particle mixtures. Indeed, the rheology of particle suspensions has a long history, yet it is still an active field of research [21, 22, 23, 24, 5]. However, it has generally focussed on the bulk properties of neutrally-buoyant suspensions inside Couette flow rheometers. To our knowledge, only Houssais et al. [20] have made any attempt to directly measure the rheology of flows over sediment beds, leaving unanswered questions related to the applicability of existing rheology models.

At the same time, numerical simulations, which can provide much more detailed information, especially in regard to stresses, have contributed to our understanding of these flows [23, 25, 26, 5, 27]. Phase-resolved simulations, which resolve the interface between particles and the fluid, accurately account for the two-way fluid-particle coupling and thereby rely on modeling only for collisions. For this reason, they are useful for situations involving dense particle-laden flows, including flows over sediment beds. They have been used to study the dynamics of bedforms in a turbulent flow [28] and sediment

fluxes under laminar conditions [29]. However, again little attention has been given to understanding sediment bed rheology, with the exception of Maurin et al. [5], who examined a simplified turbulent flow but did not use a phase-resolved approach.

We have focussed our efforts on developing numerical tools to make progress towards predicting sediment transport. To this end, we have built our own code, PARTIES (PARTicle-laden flows via immersed boundarIES), which implements an interface-resolving Immersed Boundary Method (IBM). We also developed an improved collision model, allowing us to accurately simulate flows over a sediment bed, as well as a momentum balance method, allowing us to accurately measure particle and fluid stresses within the bed and to describe the state of the bed during dilation and contraction. With all of these tools in place, we then performed a detailed analysis of the rheology of our simulated sediment beds, which may eventually lead to improved rheology models and hence better predictive sediment transport models.

This document describes the methods we employed and tools we developed to analyze sediment beds, along with their validations. Chapter 2 presents the equations of motion governing the fluid and particles. In Chapter 3, we describe our implementation of the IBM and then validate it against experiments involving single settling spheres. We present our collision model, which improves upon the work of others, in Chapter 4, where we then demonstrate its ability to reproduce immersed particle-wall collisions and discuss its important features in regard to sediment beds. Chapter 5 then validates the ability of PARTIES to accurately represent sheared sediment beds under laminar flow conditions. Having then established our simulation methods, we proceed to our analysis techniques. In Chapter 6, we discuss our implementation of the coarse-graining method, which we use to convert the discrete particle quantities into continuum fields. In Chapter 7, we develop a rigorous momentum balance that allows us to analyze stresses on the scale of individual particles. Finally, we show how all our methods together can be used to start

investigating the rheology of sediment beds in Chapter 8. After this, we end with a few closing thoughts in Chapter 9.

Chapter 2

Governing equations

2.1 Fluid motion

The fluid flow is governed by the incompressible Navier-Stokes equation,

$$\rho_f \left(\frac{\partial \mathbf{u}}{\partial t} + \nabla \cdot (\mathbf{u}\mathbf{u}) \right) = \nabla \cdot \boldsymbol{\tau} + \mathbf{f}_b + \mathbf{f}_{IBM}, \tag{2.1}$$

and the continuity equation,

$$\nabla \cdot \mathbf{u} = 0, \tag{2.2}$$

where we have also assumed a constant fluid density ρ_f, and $\boldsymbol{\tau}$ is the hydrodynamic stress tensor

$$\boldsymbol{\tau} = -p\,\mathbf{I} + \mu_f \left[\nabla \mathbf{u} + (\nabla \mathbf{u})^T \right]. \tag{2.3}$$

We utilize typical nomenclature: $\mathbf{u}$ is the fluid velocity, p is the pressure, $\mathbf{I}$ is the identity tensor, and μ_f is the dynamic viscosity. The body force $\mathbf{f}_b$ acts as a source term, which we use to mimic a constant pressure gradient in simulations involving periodic boundaries.

We treat the presence of the rigid particles as an extension of the fluid domain. The

forcing term $\mathbf{f}_{IBM}$ enforces the no-slip condition on the particle surface:

$$\mathbf{u} = \mathbf{u}_p + \boldsymbol{\omega}_p \times \mathbf{r} \quad \text{on } \Gamma_p, \tag{2.4}$$

where $\mathbf{u}_p$ and $\boldsymbol{\omega}_p$ are the translational and angular velocities, respectively, of particle p, and $\mathbf{r}$ is the position vector from the particle center of mass to a point on the particle's surface, Γ_p.

2.2 Particle motion

The motion of the particles is governed by conservation of linear momentum,

$$m_p \frac{\mathrm{d}\mathbf{u}_p}{\mathrm{d}t} = \underbrace{\int_{\Gamma_p} \boldsymbol{\tau} \cdot \mathbf{n} \, \mathrm{d}A}_{\mathbf{F}_{h,p}} + \underbrace{\int_{\Omega_p} \mathbf{f}_b \, \mathrm{d}V}_{\mathbf{F}_{b,p}} + \underbrace{V_p(\rho_p - \rho_f)\mathbf{g}}_{\mathbf{F}_{g,p}} + \mathbf{F}_{c,p}, \tag{2.5}$$

and angular momentum,

$$I_p \frac{\mathrm{d}\boldsymbol{\omega}_p}{\mathrm{d}t} = \underbrace{\int_{\Gamma_p} \mathbf{r} \times (\boldsymbol{\tau} \cdot \mathbf{n}) \, \mathrm{d}A}_{\mathbf{T}_{h,p}} + \mathbf{T}_{c,p}, \tag{2.6}$$

where m_p, I_p, V_p, and ρ_p are the mass, moment of inertia, volume, and density, respectively, of the particle, and Ω_p is the volume domain of the particle. Along the particle surface Γ_p, $\mathbf{n}$ is the outward surface normal vector. The forces and torques acting on particle p are $\mathbf{F}_{h,p}$ and $\mathbf{T}_{h,p}$, which arise from the hydrodynamic stresses acting on the particle surface, $\mathbf{F}_{b,p}$, the volume force that acts on both the fluid and particles, $\mathbf{F}_{g,p}$, the buoyancy force, and $\mathbf{F}_{c,p}$ and $\mathbf{T}_{c,p}$, which arise from collision forces with the walls and other particles. We will describe the collisions in more detail in Chapter 4.

The hydrodynamic stresses in (2.5) and (2.6) can be difficult and expensive to evaluate accurately. To work around this problem, we follow the procedure of Tschisgale et al. [30], who explain that the immersed boundary force leads to a jump condition between the fluid stresses inside, $\boldsymbol{\tau}^-$, and outside, $\boldsymbol{\tau}^+$, the particle:

$$-\int_{L_p} \mathbf{f}_{IBM}\,\mathrm{d}V = \int_{\Gamma_p} \boldsymbol{\tau}^+ \cdot \mathbf{n}\,\mathrm{d}A - \int_{\Gamma_p} \boldsymbol{\tau}^- \cdot \mathbf{n}\,\mathrm{d}A, \tag{2.7}$$

where L_p is the shell volume surrounding the particle surface and whose width is determined by the width of the Dirac delta function used for the IBM. From the material derivative of the fluid within the particle, we can obtain

$$\int_{\Gamma_p} \boldsymbol{\tau}^- \cdot \mathbf{n}\,\mathrm{d}A = \frac{\mathrm{d}}{\mathrm{d}t}\int_{\Omega_p} \rho_f \mathbf{u}\,\mathrm{d}V - \int_{\Omega_p} \mathbf{f}_b\,\mathrm{d}V, \tag{2.8}$$

where $\mathbf{f}_b$ is the body force acting on the fluid, such as an imposed pressure gradient. Thus, using (2.7) and (2.8), (2.5) becomes

$$m_p\frac{\mathrm{d}\mathbf{u}_p}{\mathrm{d}t} = \underbrace{\frac{\mathrm{d}}{\mathrm{d}t}\int_{\Omega_p} \rho_f \mathbf{u}\,\mathrm{d}V}_{\mathbf{F}_{r,p}} \underbrace{- \int_{L_p} \mathbf{f}_{IBM}\,\mathrm{d}V}_{\mathbf{F}_{IBM,p}} + \underbrace{V_p(\rho_p - \rho_f)\mathbf{g}}_{\mathbf{F}_{g,p}} + \mathbf{F}_{c,p}, \tag{2.9}$$

and (2.6) becomes

$$I_p\frac{\mathrm{d}\boldsymbol{\omega}_p}{\mathrm{d}t} = \underbrace{\frac{\mathrm{d}}{\mathrm{d}t}\int_{\Omega_p} \rho_f \mathbf{r}\times\mathbf{u}\,\mathrm{d}V}_{\mathbf{T}_{r,p}} \underbrace{- \int_{L_p} \mathbf{r}\times\mathbf{f}_{IBM}\,\mathrm{d}V}_{\mathbf{T}_{IBM,p}} + \mathbf{T}_{c,p}. \tag{2.10}$$

Here we define $\mathbf{F}_{r,p}$ and $\mathbf{T}_{r,p}$ to be the rigid body force and torque, $\mathbf{F}_{IBM,p}$ and $\mathbf{T}_{IBM,p}$ to be the IBM force and torque acting on particle p. Kempe and Fröhlich [31] demonstrated the

importance of $\mathbf{F}_{r,p}$ and $\mathbf{T}_{r,p}$ for capturing the transient particle motions, i.e. that $\mathbf{F}_{IBM,p}$ and $\mathbf{T}_{IBM,p}$ alone do not account for the full effects of the IBM acting on the particles. Note that the body force term, $\mathbf{f}_b$ drops out of the particle momentum equations (2.9) and (2.10). Thus, forcing the fluid inside the particles with $\mathbf{f}_b$ implicitly applies this body force to the particles through $\mathbf{f}_{IBM}$.

The terms $\mathbf{F}_{r,p}$, $\mathbf{T}_{r,p}$, $\mathbf{F}_{IBM,p}$, and $\mathbf{T}_{IBM,p}$ in (2.9) and (2.10) are much more straightforward to evaluate numerically than the terms $\mathbf{F}_{h,p}$ and $\mathbf{T}_{h,p}$ in (2.5) and (2.6). Furthermore, Kempe and Fröhlich [31] showed that this simpler formulation of the hydrodynamic terms allows for the use of a wider range of fluid/particle density ratios, including values $\rho_p/\rho_f \approx 1$, compared to other methods, such as that of Uhlmann [32]. In the next chapter, we will describe the discretization of these governing equations for the fluid and particle motion.

Chapter 3

Fluid-particle coupling

3.1 Introduction

In this chapter, we describe the methods used to solve the equations of motion for the fluid, (2.1) and (2.2), as well as for the particles, (2.9) and (2.10). This description includes a detailed explanation of the IBM, which couples the fluid and particle equations of motion.

Researchers have developed a number of methods to simulate interface-resolved particle-laden flows [33, 34, 32, 35, 36, 37]. "Body-conforming methods" modify the fluid mesh so that fluid nodes are coincident on the particle surface, allowing a simple and accurate representation of the boundary conditions [38, 39]. However, if the particles move within the domain, then the fluid mesh needs to be regenerated at every timestep, a procedure that can be both difficult to implement and computationally expensive [39]. Many recent developments have instead focused on "immersed methods," which use a fixed fluid mesh through which the particle-fluid interface moves [40, 39]. Though extra care must be taken to properly represent the interface, remeshing is not required, resulting in smaller computational costs, especially when many particles are involved. These methods fall

into two classes:

- Volume methods: those that enforce rigid body motion of the fluid inside the particle domain.
- Boundary methods: those that enforce the no-slip boundary condition at the surface of the particle domain. The fluid motion within the particle is typically meaningless.

3.1.1 Volume methods

Glowinski et al. [33] and Patankar et al. [41] developed a distributed Lagrange multiplier (DLM)/fictitious domain approach, which treats the entire domain (actual fluid plus particles) as a fluid, using another variable (a Lagrange multiplier) to enforce rigid body motion within the particle domain. They developed a fractional step method to couple the particle and fluid motions in a finite element formulation.

Apte et al. [42, 36] later adopted the DLM method, reformulating it for use with finite difference methods and extending its stability to a larger range of fluid-particle density ratios. Taira and Colonius [43] created an alternate framework for directly solving for the Lagrange multiplier in a finite difference formulation. Theirs is the only version of this method that simultaneously creates a divergence-free velocity field and rigid body motion of the particles (expressed through the fluid velocity field).

Volume methods have the advantages that the fluid inside the particle domain represents the particle motion well and that the method has been shown to work for very large density ratios. The disadvantage is that the computational cost scales with the cube of the number of grid cells in each dimension ($1/h^3$), whereas boundary methods, which only act on the surface, scale with the square ($1/h^2$).

3.1.2 Boundary methods

Zhang and Prosperetti [44, 45] developed PHYSALIS, a method that enforces the no-slip condition using the analytical solution for Stokes flow ($\mathrm{Re} = 0$) around a sphere. The authors argue that the Stokes flow condition is valid near the surface of the sphere even for moderate particle Reynolds numbers ($\mathrm{Re}_p \to 100$).

Another class of methods is based on applying a force near the particle surface to enforce the no-slip condition. Peskin [46] is credited as starting this group of immersed boundary methods, developing a "continuous forcing approach," which assumes elastic bodies, to simulate flow around human heart valves. Mohd-Yusof [47] developed the "direct forcing approach," which uses a mirroring technique to directly enforce the no-slip condition at the boundary. While sharply-resolving the interface, this method has problems with mass conservation around the boundary [48], which Kim and Choi [49] fix using mass source/sinks near the boundary.

Uhlmann developed an immersed boundary method that enforces the no-slip condition less directly [32]. Similarly to other immersed boundary methods, he creates a set of evenly-spaced points on the surface of the particle, called Lagrangian marker points, where the no-slip condition is applied. Differently from other immersed boundary methods, he uses Dirac Delta functions to smooth the application of the no-slip condition onto the Eulerian grid. This smoothing counteracts the oscillatory behavior encountered with other methods but leads to a less-sharp particle-fluid interface.

We have chosen to implement the IBM of Kempe and Fröhlich [31], who improved upon Uhlmann's method to allow for a larger range of stable particle/fluid density ratios. Our reasons for choosing this method were its ease of implementation, apparent numerical efficiency, and proven track record by several groups in producing accurate results [32, 31, 50]. The methods we employ make two general assumptions: spherical particles and

a uniform cubic Eulerian mesh ($\Delta x = \Delta y = \Delta z = h$). While the IBM in fact works without these assumptions (e.g. ellipsoidal particles [51] and nonuniform mesh[52]), they make many of the algorithms easier to implement and more efficient to run. Furthermore, many of our initial problems of interest involve spherical particles.

3.2 Fluid solver

In order to solve the fluid governing equations (2.1,2.2), we have implemented methods similar to those of Uhlmann [32] and Kempe and Fröhlich [31]. The fluid equations of motion are discretized onto a staggered grid, the velocity components stored at the cell faces, and the pressure stored at the cell center. A second-order central finite difference scheme is used to calculate the convective and viscous terms. Using a low-storage three-step Runge-Kutta (RK) method, we solve the Navier-Stokes equations using the following pressure-projection method:

$$\frac{\mathbf{u}^* - \mathbf{u}^{k-1}}{\alpha_k \Delta t} = \nu_f \nabla^2 \left(\mathbf{u}^* + \mathbf{u}^{k-1}\right) - \frac{2}{\rho_f}\nabla p^{k-1} - \frac{\gamma_k}{\alpha_k}\nabla \cdot (\mathbf{uu})^{k-1} - \frac{\zeta_k}{\alpha_k}\nabla \cdot (\mathbf{uu})^{k-2} \tag{3.1a}$$

$$\nabla^2 \phi = \frac{\nabla \cdot \mathbf{u}^*}{2\alpha_k \Delta t} \tag{3.1b}$$

$$\mathbf{u}^k = \mathbf{u}^* - 2\alpha_k \Delta t \, \nabla \phi \tag{3.1c}$$

$$p^k = p^{k-1} + \rho_f \phi, \tag{3.1d}$$

where ν_f is the kinematic viscosity of the fluid. Here, we advance the equations of motion from RK substep $k-1$ to substep k, where $k = \{1, 2, 3\}$ is the set of substeps that span one simulation timestep of duration Δt. The RK coefficients are given by $\alpha_k = \left\{\frac{4}{15}, \frac{1}{15}, \frac{1}{6}\right\}$, $\gamma_k = \left\{\frac{8}{15}, \frac{5}{12}, \frac{3}{4}\right\}$, and $\zeta_k = \left\{0, -\frac{17}{60}, -\frac{5}{12}\right\}$ for the respective substeps [53].

In equation (3.1a), we treat the nonlinear advection terms explicitly and the linear viscous terms implicitly to obtain a preliminary velocity field $\mathbf{u}^*$. This implicit equation is

solved using the conjugate-gradient method without preconditioning. We then solve the Poisson equation (3.1b) for the pressure-correction term ϕ using a direct solver based on fast Fourier transforms. This pressure-correction term adjusts the velocity and pressure fields in equations (3.1c, 3.1d) in order to satisfy continuity.

3.3 Immersed boundary method

3.3.1 Immersed boundary force

We can summarize Uhlmann's method for creating the IBM force as follows:

1. Interpolate the fluid velocity onto the Lagrangian marker points using the Dirac Delta function $\delta_h(\mathbf{r})$.

$$\mathbf{U}_l = \sum_k \sum_j \sum_i \delta_h(\mathbf{x}_{i,j,k} - \mathbf{X}_l)\, \mathbf{u}_{i,j,k}\, h^3, \tag{3.2}$$

   where $\mathbf{U}_l$ is the interpolated velocity at the Lagrangian marker, $\mathbf{X}_l$ is the coordinate of the marker, $\mathbf{u}_{i,j,k}$ is the fluid velocity at grid location i, j, k, and $\mathbf{x}_{i,j,k}$ is the coordinate of that fluid velocity.

2. At each marker point, there is a small discrepancy between the interpolated fluid velocity $\mathbf{U}_l$ and the rigid body motion of the sphere at that point $\mathbf{U}_l^d$. We calculate a force to rectify this difference, which will be our IB force.

$$\mathbf{F}_l = \rho_f \frac{\mathbf{U}_l^d - \mathbf{U}_l}{\Delta t} \tag{3.3}$$

   This technique effectively applies a spring force correction to the fluid velocity field, where the spring constant is equal to $\rho_f/\Delta t$. We can iterate this entire method in

hopes of obtaining convergence, which we explore in Section 3.6.2. However, other methods of convergence exist, such as that of Goza and Colonius [54], who used Newton-Raphson iterations on $\mathbf{F}_l$ to minimize the velocity error $\mathbf{U}_l^d - \mathbf{U}_l$.

3. The IB force of each marker point is spread to the Eulerian grid.

$$\mathbf{f}_{IBM}(\mathbf{x}_{i,j,k}) = \sum_{p}^{N_p} \sum_{l}^{N_l} \delta_h(\mathbf{X}_l - \mathbf{x}_{i,j,k})\, \mathbf{F}_l\, V_l, \tag{3.4}$$

where V_l is the marker volume described in the next section.

4. The total force on the particle due to the IBM is the sum of the forces from all the marker points.

$$\mathbf{F}_{IBM,p} = -\sum_{l}^{N_l} \mathbf{F}_l\, V_l \tag{3.5a}$$

$$\mathbf{T}_{IBM,p} = -\sum_{l}^{N_l} (\mathbf{X}_l - \mathbf{x_p}) \times \mathbf{F}_l\, V_l \tag{3.5b}$$

Thus, using the Dirac Delta function, we can move between the Eulerian and Lagrangian grids to satisfy the no-slip condition at the particle's surface. With equations (3.4) and (3.5), we have numerical approximations for the forcing term $\mathbf{f}_{IBM}$ in our governing equations (2.1), (2.9), and (2.10).

3.3.2 Generating Lagrangian marker points

In order to create a set of Lagrangian marker points on the surface of a sphere, we need to establish:

- The number of marker points N_l
- How to distribute the marker points along the sphere's surface

We determine the number of marker points using the same approach as Uhlmann [32]. Each marker has around it a "volume of influence" V_l, which represents the area over which the IB force is spread. In order for the IBM to work well, we would like to make V_l as close to the volume of a fluid grid cell h^3 as possible. Assuming that each marker's V_l protrudes a distance of $\frac{h}{2}$ into and out of the sphere's surface (see Figure 3.1), the volume of the marker is given by

$$V_l = \frac{\frac{4\pi}{3}\left[(R_p + \frac{h}{2})^3 - (R_p - \frac{h}{2})^3\right]}{N_l}, \tag{3.6}$$

where N_l is the number of Lagrangian markers. Specifying that $V_l \approx h^3$, we get

$$N_l \approx \frac{\pi}{3}\left[12\left(\frac{R_p}{h}\right)^2 + 1\right]. \tag{3.7}$$

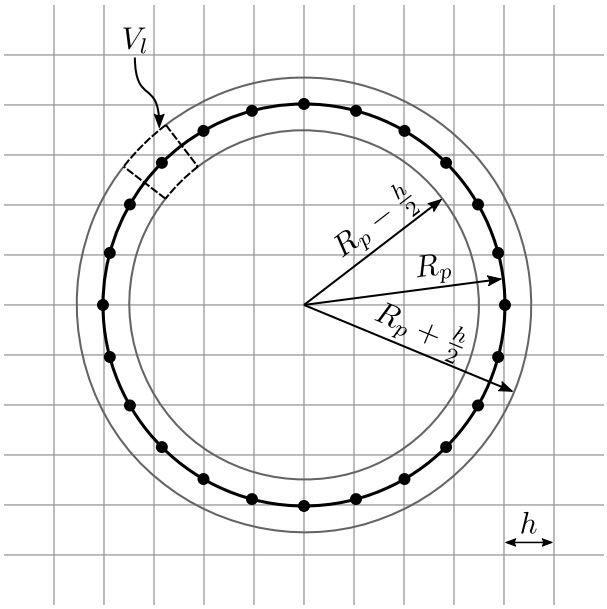

Figure 3.1: Volume of influence V_l of Lagrangian markers for a sphere with radius R_p and fluid domain with grid size h.

Now that we know how many Lagrangian markers we need, we must find a way to place them. A number of methods exist for evenly distributing a set of points on the

surface of a sphere. Uhlmann [32] used an iterative method that treats the markers as charged particle free to move along the surface and allows them to settle into a minimum energy configuration. Saff and Kuijlaars [55] developed a method that places the markers in a spiral pattern, which works well for a large number of markers. We employ Leopardi's algorithm [56], which places the markers in a series of rings and also works well for a large number of markers.

3.3.3 Interpolation and spreading between Eulerian and Lagrangian grids

To carry out interpolation and spreading operations, PARTIES uses the Dirac Delta function of Roma et al. [57]:

$$\delta(r) = \begin{cases} \frac{1}{6}\left[5 - 3|r| - \sqrt{-3(1-|r|)^2+1}\right] & 0.5 \le |r| \le 1.5 \\ \frac{1}{3}\left[1 + \sqrt{-3|r|^2+1}\right] & |r| \le 0.5 \\ 0 & |r| \ge 1.5 \end{cases} . \tag{3.8}$$

This function has several properties [57]:

1. $\delta(r)$ is continuous $\forall\, r \in \mathbb{R}$
2. $\delta(r) = 0$ for $|r| \ge 1.5$
3. $\sum_{i\in\mathbb{Z}} \delta(r-i) = 1 \;\forall\, r \in \mathbb{R}$
4. $\sum_{i\in\mathbb{Z}} (r-i)\delta(r-i) = 0 \;\forall\, r \in \mathbb{R}$
5. $\sum_{i\in\mathbb{Z}} [\delta(r-i)]^2 = \frac{1}{2} \;\forall\, r \in \mathbb{R}$

The significance of these properties is as follows:

1. Allows for smooth interpolation/spreading
2. Limits the support of the function to three grid cells
3. Guarantees the conservation of the spread quantity, which leads to conservation of linear momentum
4. Together with property 3, guarantees conservation of angular momentum
5. Ensures that the effect of one Lagrangian marker on another is maximized when both points coincide

We then define another function based on this Dirac Delta function:

$$\delta_h^{1\mathrm{D}}(r) = \frac{1}{h}\delta\left(\frac{r}{h}\right) \tag{3.9a}$$

$$\delta_h(\mathbf{r}) = \delta_h^{1\mathrm{D}}(x)\,\delta_h^{1\mathrm{D}}(y)\,\delta_h^{1\mathrm{D}}(z), \tag{3.9b}$$

where $\mathbf{r} = (x, y, z)$ is a position vector and $h = \Delta x = \Delta y = \Delta z$ is the grid spacing. This function scales $\delta(r)$ to have a support of three fluid grid cells.

We can use this function to interpolate an Eulerian quantity onto a Lagrangian point, such as the fluid velocity in equation (3.2), where $\mathbf{x}_{i,j,k}$ is the coordinate of the velocity node and $\mathbf{X}_l$ is the coordinate of the Lagrangian marker. Due to the staggered grid, we must carry out this interpolation separately for each velocity component.

Similarly, we can spread a Lagrangian quantity onto the Eulerian mesh, such as the IB force in equation (3.4). Here, V_l represents the "volume of influence" of the Lagrangian marker. Again, $\mathbf{f}_{IBM}(\mathbf{x}_{i,j,k})$ acts at different coordinates for each velocity component, requiring that we calculate this spreading separately for the u-, v-, and w-momentum equations.

3.4 Particle motion

The framework in place, we discretize the particle equations of motion, (2.9) and (2.10), as follows:

We discretize $\mathbf{F}_{r,p}$ and $\mathbf{T}_{r,p}$ by

$$\frac{\mathrm{d}}{\mathrm{d}t}\int\limits_{\Omega_p} \rho_f\,\mathbf{u}\,\mathrm{d}V \approx \frac{\rho_f}{2\alpha_k\Delta t}\left(\int\limits_{\Omega_p^k} \mathbf{u}^k\,\mathrm{d}V - \int\limits_{\Omega_p^{k-1}} \mathbf{u}^{k-1}\,\mathrm{d}V\right) \tag{3.10a}$$

$$\frac{\mathrm{d}}{\mathrm{d}t}\int\limits_{\Omega_p} \rho_f\,\mathbf{r}\times\mathbf{u}\,\mathrm{d}V \approx \frac{\rho_f}{2\alpha_k\Delta t}\left(\int\limits_{\Omega_p^k} \mathbf{r}\times\mathbf{u}^k\,\mathrm{d}V - \int\limits_{\Omega_p^{k-1}} \mathbf{r}\times\mathbf{u}^{k-1}\,\mathrm{d}V\right), \tag{3.10b}$$

where k is the Runge-Kutta substep and the RHS volume integrals are evaluated according to equation (3.22).

As developed in Section 3.3.1, we approximate the IBM forces acting on the particle as:

$$\int\limits_{\Omega_p} \mathbf{f}_{IBM}\,\mathrm{d}V \approx \sum_l^{N_l} \mathbf{F}_l\,V_l \tag{3.11}$$

$$\int\limits_{\Omega_p} \mathbf{r}\times\mathbf{f}_{IBM}\,\mathrm{d}V \approx \sum_l^{N_l} (\mathbf{X}_l - \mathbf{x_p})\times\mathbf{F}_l\,V_l. \tag{3.12}$$

Following the example of Kempe and Fröhlich [31], we fully couple the governing equations (2.1), (2.2), (2.9), and (2.10) through the following steps:

1. Determine desired velocity of Lagrangian marker points

$$\mathbf{U}_l^d = \mathbf{u}_p^{k-1} + \boldsymbol{\omega}_p^{k-1}\times\left(\mathbf{X}_l - \mathbf{x}_p^{k-1}\right) \tag{3.13}$$

2. Calculate a preliminary velocity field.

$$\frac{\widetilde{\mathbf{u}} - \mathbf{u}^{k-1}}{\alpha_k \Delta t} = 2\nu_f \nabla^2 \mathbf{u}^{k-1} - \frac{2}{\rho_f}\nabla p^{k-1} - \frac{\gamma_k}{\alpha_k}\nabla\cdot(\mathbf{uu})^{k-1} - \frac{\zeta_k}{\alpha_k}\nabla\cdot(\mathbf{uu})^{k-2} + \frac{2}{\rho_f}\mathbf{f}_b \quad (3.14)$$

3. Apply IBM forcing to enforce the no-slip condition

$$\mathbf{U}_l = \sum_k \sum_j \sum_i \widetilde{\mathbf{u}}(\mathbf{x}_{i,j,k})\delta_h(\mathbf{x}_{i,j,k} - \mathbf{X}_l)h^3 \quad (3.15a)$$

$$\mathbf{F}_l = \rho_f \frac{\mathbf{U}_l^d - \mathbf{U}_l}{2\alpha_k \Delta t} \quad (3.15b)$$

$$\mathbf{f}_{IBM}(\mathbf{x}_{i,j,k}) = \sum_p^{N_p} \sum_l^{N_l} \delta_h(\mathbf{x}_{i,j,k} - \mathbf{X}_l)\,\mathbf{F}_l\,V_l \quad (3.15c)$$

$$\mathbf{F}_{IBM,p} = -\sum_l^{N_l} \mathbf{F}_l\,V_l \quad (3.15d)$$

$$\mathbf{T}_{IBM,p} = -\sum_l^{N_l} (\mathbf{X}_l - \mathbf{x_p}) \times \mathbf{F}_l\,V_l \quad (3.15e)$$

4. Solve the Helmholtz equation in order to evaluate viscous terms using the Crank Nicholson method.

$$\frac{\widehat{\mathbf{u}} - \widetilde{\mathbf{u}}}{\alpha_k \Delta t} = \nu_f \nabla^2 \widehat{\mathbf{u}} - \nu_f \nabla^2 \mathbf{u}^{k-1} + \frac{2}{\rho_f}\mathbf{f}_{IBM} \quad (3.16)$$

5. Apply additional IBM forcing to further enforce the no-slip condition, now that the

fluid velocity field has been modified. This will be further explained in Section 3.6.2.

$$\mathbf{u}^{(0)} = \widehat{\mathbf{u}} \tag{3.17a}$$

for $m = 1 : n_f$ {

$$\mathbf{U}_l = \sum_k \sum_j \sum_i \delta_h(\mathbf{x}_{i,j,k} - \mathbf{X}_l)\, \mathbf{u}_{i,j,k}^{(m-1)}\, h^3 \tag{3.17b}$$

$$\mathbf{F}_l = \rho_f \frac{\mathbf{U}_l^d - \mathbf{U}_l}{2\alpha_k \Delta t} \tag{3.17c}$$

$$\mathbf{f}_{IBM}(\mathbf{x}_{i,j,k}) = \sum_p^{N_p} \sum_l^{N_l} \delta_h(\mathbf{x}_{i,j,k} - \mathbf{X}_l)\, \mathbf{F}_l\, V_l \tag{3.17d}$$

$$\mathbf{u}^{(m)} = \mathbf{u}^{(m-1)} + 2\rho_f \alpha_k \Delta t\, \mathbf{f}_{IBM} \tag{3.17e}$$

$$\mathbf{F}_{IBM,p} = \mathbf{F}_{IBM,p} - \sum_l^{N_l} \mathbf{F}_l\, V_l \tag{3.17f}$$

$$\mathbf{T}_{IBM,p} = \mathbf{T}_{IBM,p} - \sum_l^{N_l} (\mathbf{X}_l - \mathbf{x_p}) \times \mathbf{F}_l\, V_l \tag{3.17g}$$

}

$$\mathbf{u}^* = \mathbf{u}^{(n_f)} \tag{3.17h}$$

6. Solve the Poisson equation for the pressure correction term to enforce continuity.

$$\nabla^2 \phi = \frac{\nabla \cdot \mathbf{u}^*}{2\alpha_k \Delta t} \tag{3.18}$$

7. Apply the pressure correction to the pressure and velocity fields.

$$\mathbf{u}^k = \mathbf{u}^* - 2\alpha_k \Delta t\, \nabla \phi \tag{3.19a}$$

$$p^k = p^{k-1} + \rho_f \phi \tag{3.19b}$$

8. Evaluate all hydrodynamic forces acting on the particle.

$$\mathbf{F}_{f,p} = \underbrace{\frac{\rho_f}{2\alpha_k \Delta t}\left(\int\limits_{\Omega_p^k} \mathbf{u}^k \,\mathrm{dV} - \int\limits_{\Omega_p^{k-1}} \mathbf{u}^{k-1} \,\mathrm{dV}\right)}_{\mathbf{F}_{r,p}} + \mathbf{F}_{IBM,p} \tag{3.20a}$$

$$\mathbf{T}_{f,p} = \underbrace{\frac{\rho_f}{2\alpha_k \Delta t}\left(\int\limits_{\Omega_p^k} \mathbf{r} \times \mathbf{u}^k \,\mathrm{dV} - \int\limits_{\Omega_p^{k-1}} \mathbf{r} \times \mathbf{u}^{k-1} \,\mathrm{dV}\right)}_{\mathbf{T}_{r,p}} + \mathbf{T}_{IBM,p} \tag{3.20b}$$

9. Solve particle equations of motion using fluid forces ($\mathbf{F}_{f,p}$), buoyant forces ($\mathbf{F}_{g,p}$), and collision forces ($\mathbf{F}_{c,p}$), the latter of which will be discussed in Chapter 4.

$$\mathbf{u}_p^k = \mathbf{u}_p^{k-1} + \frac{2\alpha_k \Delta t}{m_p}\left(\mathbf{F}_{f,p} + \mathbf{F}_{g,p} + \mathbf{F}_{c,p}\right) \tag{3.21a}$$

$$\boldsymbol{\omega}_p^k = \boldsymbol{\omega}_p^{k-1} + \frac{2\alpha_k \Delta t}{I_p}\left(\mathbf{T}_{f,p} + \mathbf{T}_{c,p}\right) \tag{3.21b}$$

$$\mathbf{x}_p^k = \mathbf{x}_p^{k-1} + \alpha_k \Delta t\left(\mathbf{u}_p^k + \mathbf{u}_p^{k-1}\right) \tag{3.21c}$$

$$\tag{3.21d}$$

3.5 Volume fraction

One method for numerically evaluating the volume integrals in equation (3.10) requires the volume fraction $\phi_{i,j,k}$ of the particles in the Eulerian grid. For each fluid grid cell (i, j, k), this volume fraction gives us the fraction of the cell occupied by the particle ($\phi = 1$ inside the particle), allowing us to numerically evaluate a volume integral as

$$\int\limits_{\Omega_p} \mathbf{u} \,\mathrm{d}V \approx \sum_k \sum_j \sum_i \phi_{i,j,k}\, \mathbf{u}_{i,j,k}\, V_{i,j,k}, \tag{3.22}$$

where $V_{i,j,k}$ is the volume of cell (i, j, k). Note, however, that due to the staggered grid arrangement, this volume fraction will have to be evaluated separately for each velocity component.

To calculate the volume fraction, we employ the level-set method used by Kempe and Fröhlich [58], which allows for efficient evaluation but at a lower accuracy compared to other methods. The volume fraction is given by

$$\phi_{i,j,k} = \frac{\sum_{m=1}^{8} -\varphi_m \, H(-\varphi_m)}{\sum_{m=1}^{8} |\varphi_m|}, \tag{3.23}$$

where $H(\varphi)$ is the heavyside function

$$H(\varphi) = \begin{cases} 0, & \varphi \leq 0 \\ & \\ 1, & \varphi > 0 \end{cases}, \tag{3.24}$$

and φ is the level-set function, which is evaluated at the eight corners m of the control volume for $\phi_{i,j,k}$. $\varphi = 0$ represents the surface of the sphere, with $\varphi < 0$ being inside the sphere and $\varphi > 0$ being outside the sphere. For a sphere, the level-set function is

$$\varphi = \frac{\sqrt{(x - x_p)^2 + (y - y_p)^2 + (z - z_p)^2}}{R_p} - 1, \tag{3.25}$$

where (x, y, z) is the coordinate of φ and $\mathbf{x}_p = (x_p, y_p, z_p)$ is the position of the center of sphere p.

3.6 Validation

3.6.1 Settling velocity

To validate the fluid-particle coupling, we will use the case of a single sphere settling under gravity in a fluid. In this situation, the important parameter to consider is the particle Reynolds number

$$\mathrm{Re}_p = \frac{u_\infty D_p}{\nu_f}, \tag{3.26}$$

where D_p is the particle diameter ν_f is the kinematic viscosity, and u_∞ is the settling velocity. We also utilize a reference time scale and velocity scale based on gravity to nondimensionalize the results:

$$t_{ref} = \sqrt{\frac{D_p}{g}} \tag{3.27a}$$

$$u_{ref} = \sqrt{D_p\, g}. \tag{3.27b}$$

Note that, consistent with the nondimensionalization of Uhlmann [32], these reference scales do not use a reduced gravity, which depends on the relative particle/fluid densities. Mordant and Pinton [59] carried out a series of moderate Reynolds number experiments ($12 < \mathrm{Re}_p < 376$) involving the settling of a single sphere under gravity in a large tank. ten Cate et al. [60] carried out experiments at lower Renolds numbers ($1.5 < \mathrm{Re}_p < 32$), observing the settling velocity as the sphere approaches the lower wall of a large tank.

We also consider the work of Brown and Lawler [61], who aggregated the results of many experiments into an empirical correlation for the settling velocity of a sphere:

$$u_* = \frac{d_*^2\,(22.5 + d_*^{2.046})}{0.0258 d_*^{4.046} + 2.81 d_*^{3.046} + 18 d_*^{2.046} + 405}, \tag{3.28}$$

where d_* and u_* are, respectively, a non-dimensional diameter and settling velocity of

Re_p	Experiment	R_p (m)	ρ_p/ρ_f	ν_f (m^2/s)	g (m/s^2)
41	Mordant & Pinton	1/12	2.5677	5.416×10^{-3}	9.81
360	Mordant & Pinton	1/12	2.5677	1.042×10^{-3}	9.81
12	ten Cate et al.	0.0075	1.164	1.175×10^{-4}	9.81
32	ten Cate et al.	0.0075	1.167	6.042×10^{-5}	9.81

Table 3.1: Simulation parameters to match Mordant and Pinton. [59] and ten Cate et al. [60].

Re_p	Domain size (m) ($L_x \times L_y \times L_z$)	Domain boundary conditions	y_0 (m)	N_x	D_p/h	Timestep
41	$1.25 \times 10 \times 1.25$	s × p × s	9.0	76, 150, 226	10, 20, 30	CFL = 0.5
360	$1.25 \times 10 \times 1.25$	s × p × s	9.0	76, 150, 226	10, 20, 30	CFL = 0.5
12	$0.1 \times 0.2 \times 0.1$	p × ns × p	0.13	92, 128, 192	14, 19, 29	CFL = 0.5
32	$0.1 \times 0.2 \times 0.1$	p × ns × p	0.131	92, 128, 192	14, 19, 29	CFL = 0.5

Table 3.2: Simulation setup to match experiments of Table 3.1. Boundary conditions can be periodic (p), slip (s), or no-slip (ns). The number of grid cells in the x-direction is N_x, and the initial position of the center of the sphere is y_0.

the sphere:

$$d_* = 2R_p \left[\frac{g\rho_f(\rho_p - \rho_f)}{\mu_f^2} \right]^{1/3} \tag{3.29a}$$

$$u_* = u_\infty \left[\frac{\rho_f^2}{g\mu_f(\rho_p - \rho_f)} \right]^{1/3}. \tag{3.29b}$$

This correlation fits 97% of the studied experimental data to within a 5% error margin. Using the parameters in Table 3.1 and the simulation setup in Table 3.2, we conducted simulations to match the experiments of Mordant and Pinton [59] and ten Cate et al. [60].

3.6.2 Number of forcing loop iterations

The method developed by Kempe and Fröhlich [31] includes an additional forcing loop after the solution of the Helmholtz equation, shown in equation (3.17). These authors state that this loop is necessary to ensure the no-slip condition is satisfied, recommending

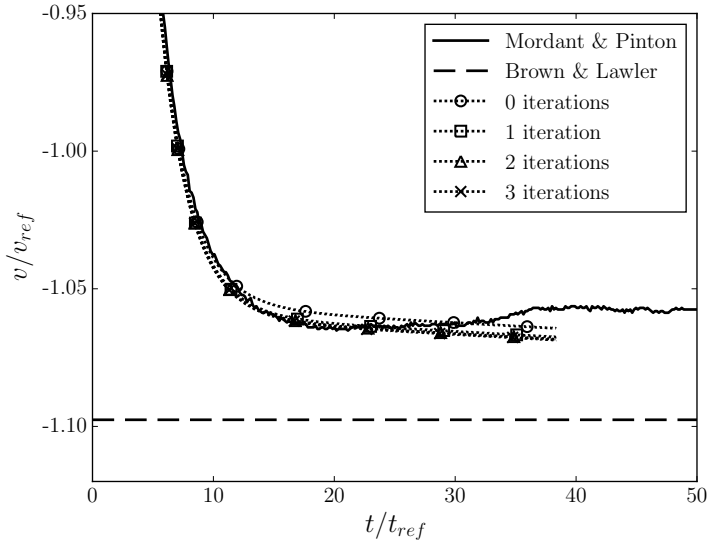

Figure 3.2: Effect of number of forcing loop iterations for $\mathrm{Re}_p = 41$ at 20 grid cells/diameter. We have zoomed in along the vertical axis to highlight the differences.

three iterations. However, in our experience working with Peskin's Dirac Delta function, we noticed that interpolating and forcing several times in a row can lead to less-smooth or oscillatory results. We also noticed that the number of forcing loops can greatly affect the results for particle-wall collisions. We therefore conducted our own brief study of the number of forcing loop iterations.

For this study, we considered the $\mathrm{Re}_p = 41$ settling sphere case, where we studied the effect of changing the number of forcing loop iterations on the settling velocity. The results are shown in Figure 3.2. Adding more than one iteration results in very small changes in the overall behavior, certainly smaller than the effect of changing the grid resolution. Based on these results, our desire to not impose the forcing too frequently, and the sake of computational efficiency, we have decided to utilize one forcing loop iteration for our simulations, including all those mentioned in this document.

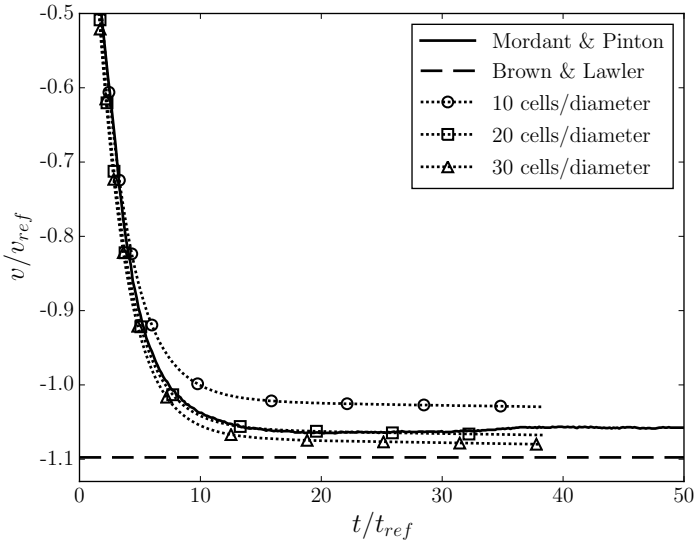

Figure 3.3: Comparison of settling velocities for $\mathrm{Re}_p = 41$.

3.6.3 Settling velocity at different Reynolds numbers

Figures 3.3–3.6 show the convergence of the settling velocity to these experiments for a range of Reynolds numbers. In Figure 3.3 the transient sphere velocity matches well with Mordant and Pinton's experiment for $\mathrm{Re}_p = 41$ and that, with grid refinement, the steady-state velocity appears to converge more towards Brown and Lawler's relationship (3.28). However, the converged settling velocity is within 5% of both Mordant and Pinton's experiment and Brown and Lawler's correlation.

For the $\mathrm{Re}_p = 360$ case shown in Figure 3.4, unsteady behavior emerges in the 30 cells/diameter simulation. Above Reynolds numbers of 210, the flow past a fixed sphere loses its axisymmetry [62], and in the range of Reynolds numbers from 270 to 300 the flow becomes unsteady [63]. The Mordant and Pinton results represent the average velocity for a number of experiments, whereas the simulation results represent single instances.

Again, the simulation results tend to converge towards the Brown and Lawler relationship (3.28). However, in the 30 cells/diameter simulation, the sphere tumbles out

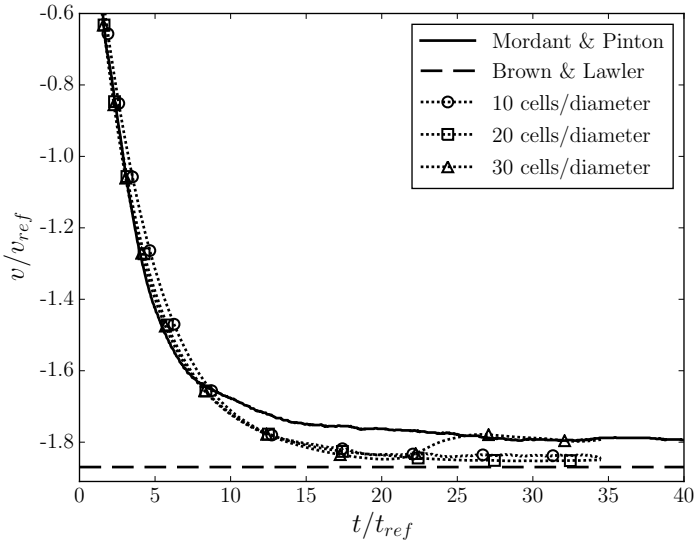

Figure 3.4: Comparison of settling velocities for $\mathrm{Re}_p = 360$.

of its path and, no longer supported by its long wake, slows down to the Mordant and Pinton mean settling velocity.

Figures 3.5 and 3.6 demonstrate our code's ability to capture sphere-wall interactions and settling velocities at lower Reynolds numbers compared to the experiments of ten Cate et al. In both figures, we can see that the simulation does an excellent job, capturing the transient motion in ten Cate's experiments and converging to the experiments with grid refinement.

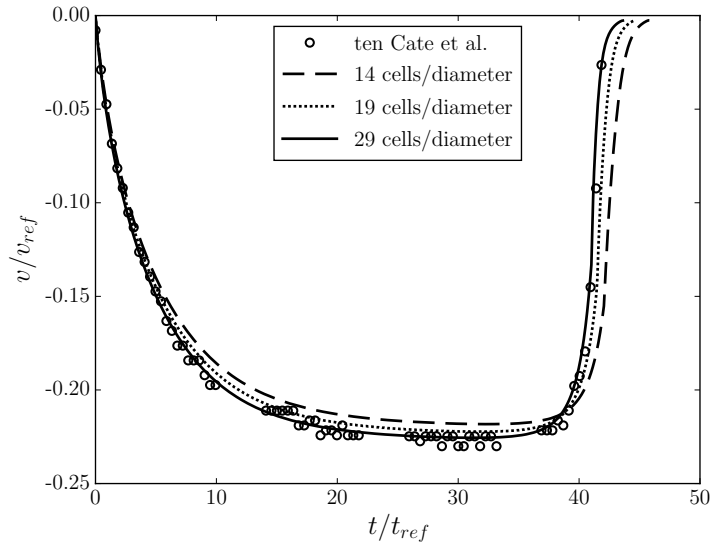

Figure 3.5: Comparison of settling velocities for $\mathrm{Re}_p = 12$.

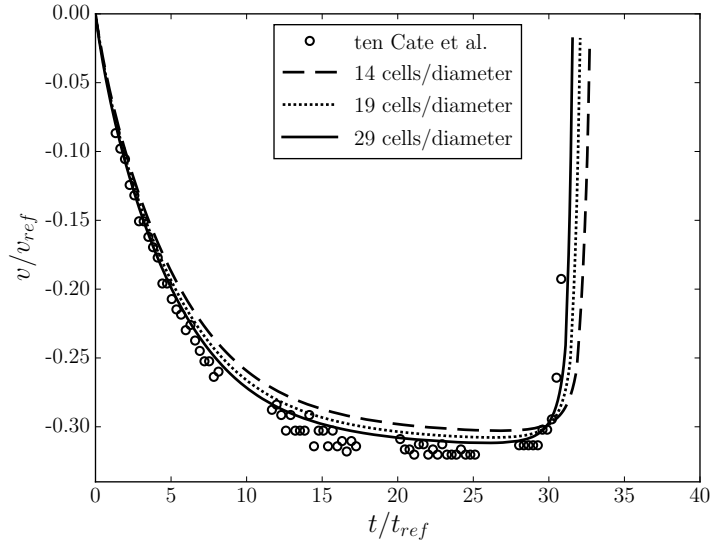

Figure 3.6: Comparison of settling velocities for $\mathrm{Re}_p = 32$.

3.6.4 Effect of radius retraction

An interesting paper was put forth by Wim-Paul Breugem [50], who proposed a method for increasing the accuracy of this IBM. Noticing that the method we have implemented tends to overpredict the drag on the particles, he proposed to retract the Lagrangian markers to a radius inside the particle in order to offset the effectively-larger particle that results from the Dirac Delta function smoothing the IBM force out into the surrounding fluid. Based on a set of experiments, Breugem established an empirical retraction distance of $r_d = 0.3h$.

We conducted our own experiments with this method, which only involves moving the location of the Lagrangian markers. For lower Reynolds numbers ($\mathrm{Re}_p = 12$–41), the results were very promising, as demonstrated in Figure 3.7.

In this figure, the trajectories have collapsed onto one another when compared to the results of the normal method shown in Figure 3.3, though they again converge towards the Brown and Lawler relationship. Thus, the effect of the larger effective particle radius at lower grid resolutions seems to have been counteracted.

However, we see a different picture at higher Reynolds numbers. Figure 3.8 shows the results at $\mathrm{Re}_p = 360$, where the curves do not collapse nearly as well. The results also seem to overpredict the settling velocity, the sphere experiencing less drag than it should.

While this method seems to work well in a viscous, laminar regime, we have seen evidence that it may be much less effective at larger Reynolds numbers. Given this observation and the fact that this method is based on empirical results at low Reynolds numbers, we will not be implementing it in PARTIES.

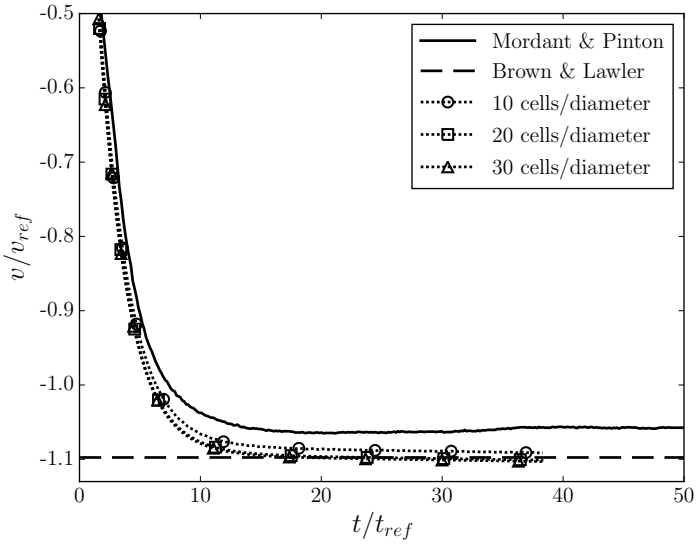

Figure 3.7: Settling velocities with retracted Lagrangian markers at $\mathrm{Re}_p = 41$.

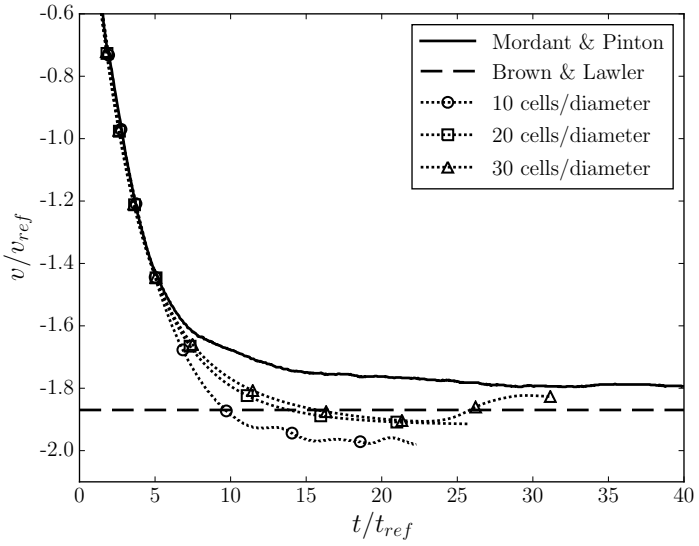

Figure 3.8: Settling velocities with retracted Lagrangian markers at $\mathrm{Re}_p = 360$.

Chapter 4

Collision modeling

4.1 Introduction

Although there exists a variety of phase-resolving methods, the choice of collision models, on the other hand, has not been as diverse. Derksen [64, 65] used a hard-sphere model, which resolves collisions instantaneously. Glowinski et al. [33] have developed a repulsive potential (RP) model that prevents particles from overlapping by applying a repulsive force at some small distance before the particles come in contact. Many other authors have adopted this model for simulations involving dilute suspensions of particles. For example, Uhlmann [66] and Santarelli and Fröhlich [67] investigated particles in a vertical turbulent channel flow, Lucci et al. [68] studied the impact of finite size particles on isotropic turbulence, and Breugem [50] and Picano et al. [69] have presented results for a horizontal flow laden with neutrally-buoyant particles. In these simulations, particles rarely came in contact, and thus were successfully governed mostly by the IBM, using the repulsive potential only to prevent overlap.

For the situation involving shear flow over a densely-packed sediment bed, however, particle-particle contact becomes ubiquitous [70]. Hard sphere models cannot maintain

simultaneous collisions or enduring contacts between multiple interacting particles, but instead represent sediment beds as particles in constant, minute motion [65]. However, they have been used to reproduce critical erosion conditions for a laminar shear flow [64]. The drawbacks of the RP model for the situation of sediment transport have been clearly-elaborated by Kempe et al. [71]. Using the RP in the framework of the IBM introduces an artificial gap of two times the grid cell size between colliding particles so that the fluid in the gap between the particle surfaces can still be resolved [72]. For the situation of sediment transport, however, the artificial gap also introduces an unphysical protrusion of the particles into the horizontal flow, which is critical as the protrusion has been acknowledged to be a very sensitive parameter for particle mobilization [73]. In addition, the RP model introduces a material stiffness k_n which has to be calculated *a priori* to design a collision model that is numerically stable. If the value of k_n is chosen too high, the repulsive force is overestimated and the particle would experience an unphysical high rebound velocity. On the other hand, if k_n is too low, the duration of the particle collision would be too large. The resuspension mechanisms, however, generate a high variety of particle impact velocities u_{in} for the collisions, typically characterized by the nondimensional Stokes number $\mathrm{St} = \rho_p u_{in} D_p / (9\,\rho_f\,\nu_f)$, where ρ_p and ρ_f are the particle and fluid density, respectively, D_p is the particle diameter, and ν_f is the kinematic viscosity of the fluid. In fact, for bed-load transport in water the variety can span from $\mathrm{St} \gg 10$ (saltating particles, [74]) to $\mathrm{St} = \mathcal{O}(10)$ (rolling particles, [8]) to $\mathrm{St} \ll 1$ (enduring contact within the sediment bed). Hence, selecting a stiffness that is stable for high-impact velocities results in excessively low stiffnesses within the bed, which acts as an unphysical dampening of the system.

Although there are studies of particle-laden horizontal flows such as Shao et al. [75] and Kidanemariam et al. [76] in which the model by Glowinski et al. [33] has been employed, these had to be limited to small volume fractions and conclusions about particle-

particle interaction have not been possible. Kidanemariam and Uhlmann [29] used an improved repulsive linear spring-dashpot model that solves the issues with calibrating k_n, but still relies on an artificial gap distance. Thus, in order to obtain appropriate bulk sediment transport quantities, they calibrated the dry restitution coefficient $e_{dry} = -u_{out}/u_{in}$, where u_{out} is the rebound velocity as soon as the collision process is finished, although this parameter can be set exactly as a material property. It describes the dissipation of kinetic energy due to the inelastic mechanics of the dry contact and is typically in the range of $0.8 \leq e_{dry} < 1$ for silicate materials Joseph et al. [77]. In the study of Kidanemariam and Uhlmann [29], a rather unphysical value of $e_{dry} = 0.3$ was used to match the bulk transport rates of glass spheres from the experiments of Aussillous et al. [19].

More recently, a more consistent approach has been advocated in the literature for which the artificial gap size is no longer needed [78, 58, 79, 80, 81]. This approach uses a lubrication force when the particles come in close contact ($0 < \zeta_n \leq 2h$, where ζ_n is the distance between the two surfaces), and a contact force when the surfaces come in contact and slightly overlap ($\zeta_n \leq 0$). The lubrication force, which is based on lubrication theory, models the fluid forces acting on the particle that cannot be resolved by the computational mesh. The contact force models material deformations and friction through components that are, respectively, normal and tangent to the surface. Since these models attempt to address the actual physics of the collision, they have had much success in reproducing the desired restitution coefficients over a range of Stokes numbers for the experiments by Joseph et al. [77]. Simeonov and Calantoni [78] performed a detailed analysis breaking down the individual effects from lubrication forces, contact forces, and hydrodynamic forces. However, only Kempe and Fröhlich [58] and Costa et al. [80] have demonstrated that their models were able to reproduce the trajectories of a particle-wall impact provided by the benchmark experiments of Gondret et al. [82]. Both

studies show that the good agreement with the rebound trajectories is made possible by slightly stretching the collision process in time: long enough to resolve the response of the fluid field to the particle kinematics but shorter than any relevant physical timescale in the flow. In addition, both modeling approaches use an adaptive procedure to obtain mathematically-rigorous solutions to the ordinary differential equations governing particle motion during contact. Using the model of Kempe and Fröhlich [58], a breakthrough was achieved by Vowinckel et al. [28], who successfully carried out numerical simulations of turbulent horizontal channel flow laden with tens of thousands of particles.

In this chapter, we build on the model proposed by Kempe and Fröhlich [58] to extend it to situations of very dense packing fractions. For example, in order for their collision model to work as designed, Kempe and Fröhlich [58] neglect the hydrodynamic forces acting on a particle while it is in contact with another object. This was addressed implicitly by Kempe et al. [71], even though it was not stated in their paper, by including the hydrodynamic forces in the equation of motion regardless of the type of collision (Kempe & Fröhlich, 2016, private communication). Furthermore, their model for the tangential contact force, which is designed to exactly enforce zero slip between particles, does not converge to a steady-state configuration for enduring contact. While this model worked well for simulations involving thin beds of particles at higher Reynolds numbers and Stokes numbers, we would like to extend it to work for thick beds of particles at a range of different Stokes numbers. At this point, models from the Discrete Element Method (DEM) community, who simulate dry granular flows, seem to be more appropriate, as they introduce a "memory" of the friction required to reach steady-state conditions [83]. Costa et al. [80] proposed a scheme with an enhanced treatment of lubrication forces, which can also be applied to smaller Stokes numbers as well as a variety of impact angles ψ_{in}. In this reference, however, they neither considered the situation of enduring contact nor conducted a validation on a larger scale addressing the collective effects of particle

motion.

Finally, another aspect that has received far less attention so far is the situation of a sediment consisting of particles with varying particle diameters. Interestingly, all of the references cited so far deal with spherical monodisperse particles. To our knowledge the only study considering horizontal channel flows laden with polydisperse sediment has been performed by Fukuoka et al. [84] using a front-tracking technique, but neither did the authors account for the feedback of the particles on the flow nor have they provided a validation for the experimental standard benchmark test cases such as particles settling in an ambient fluid or colliding with a wall. The absence of studies addressing polydisperse sediment with fully coupled IBM simulations is ever the more surprising, since its impact has been acknowledged as a key issue in the development and evolution of bedforms by segregation effects as reviewed by Charru et al. [85].

As a consequence, we aim to resolve the problems mentioned above. Among the key challenges identified are i) deriving collision models for polydisperse sediment, ii) avoiding the introduction of an artificial gap between colliding particles, iii) adaptively-calibrating the particle stiffness to simulate a wide range of Stokes numbers in a consistent manner, iv) introducing suitable criteria to extend existing models towards the numerically-challenging situation of enduring contact for both normal and oblique collisions, and v) minimizing the number of tunable parameters within the model framework. We achieve our goals by presenting an implementation of collision models for polydisperse sediment. We use the adaptive procedure proposed by Kempe and Fröhlich [58] for normal forces and the tangential model of Thornton et al. [86], which stems from DEM. Furthermore, we extend both of these approaches for the situation of enduring contact. In particular, for enduring contact, we took care to retain all the governing terms of the momentum balance of a particle, i.e. hydrodynamic forces, buoyant weight, and collision forces. This measure turns out to be crucial when simulating flows over sediment beds, as the Shields

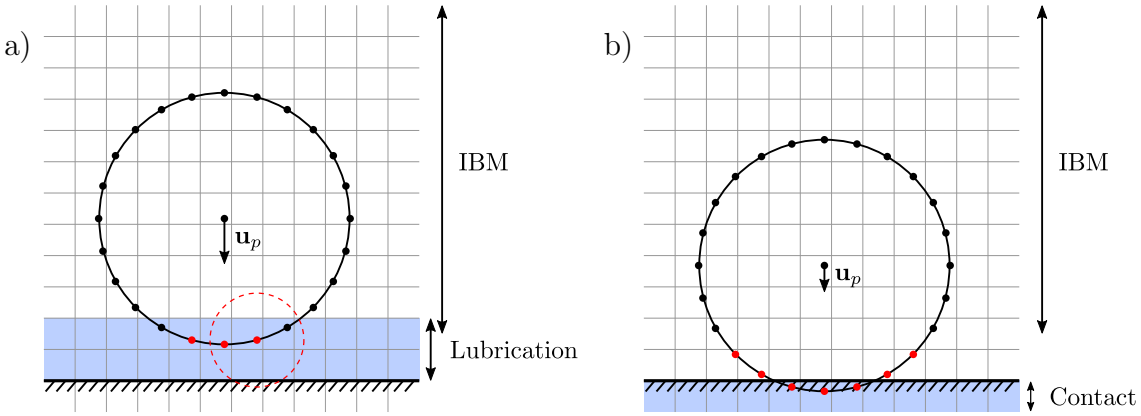

Figure 4.1: Regions where short-range interactions occur. Points on particle surface represent Lagrangian markers. Red markers have been turned off. a) Lubrication region where red dashed circle illustrates support of Dirac delta function and b) Contact region.

parameter is based on the ratio of hydrodynamic to buoyant forces. The proposed enhancements allow us to reproduce several laboratory benchmark test cases for binary collisions.

The chapter is structured as follows. We briefly describe the structure of the collision model in Section 4.1.1, followed by the mathematical description of the collision model employed in Section 4.2. We then present necessary enhancements to the collision model to deal with small Stokes numbers (Section 4.3) and to simulate dense granular packings with the gross of the particles in enduring contact (Section 4.4). In sections 4.3 and 4.4 we also validate our methods using collisions between a single particle and a wall.

4.1.1 Structure of the collision model

As mentioned in the introduction, one of the major advantages of the IBM is the direct computation of long-range interactions between the particles. Only short-range interactions and collisions need to be modeled. For example, consider a particle approaching and colliding with a wall, as shown in Figure 4.1. As the particle comes close to the wall, two problems need to be dealt with: first, the smoothed Dirac delta functions used for

the IBM overlap with the wall, and second, the discrete mesh can no longer resolve the fluid being squeezed out from between the two surfaces.

We can solve the first problem by disabling Lagrangian marker points whose supports overlap with the wall (red dashed circle in Figure 4.1a), as was done by Kempe and Fröhlich [31]. This means that the forcing by these select markers on both the fluid and the particles is ignored, preventing the particle from using undefined information from outside of the domain and from competing with the wall for enforcing the no-slip condition. Figure 4.1 illustrates the red markers that have been disabled. Similarly, overlapping markers between two particles are disabled. We solve the second problem by adding a lubrication force, which models the subgrid forces on the particle due to the narrow gap and also accounts for some of the fluid forces from the disabled Lagrangian markers. We apply this force when the particle-wall distance is less than two grid cells ($0 < \zeta_n \leq 2h$), illustrated by the blue region in Figure 4.1a. Once the particle comes into contact with the wall ($\zeta_n \leq 0$), we apply a contact force to prevent particles from overlapping too much and to account for proper momentum transfer and energy loss. This contact force involves components both normal and tangent to the two surfaces, representing material deformations and friction, respectively.

Hence, the following case distinctions can be made for the normal collision forces

$$\mathbf{F}_n = \begin{cases} 0 & \zeta_n > 2h \\ \text{lubrication model (4.5)} & 0 < \zeta_n \leq 2h \\ \text{normal contact model (4.6)} & \zeta_n \leq 0 \end{cases} \tag{4.1}$$

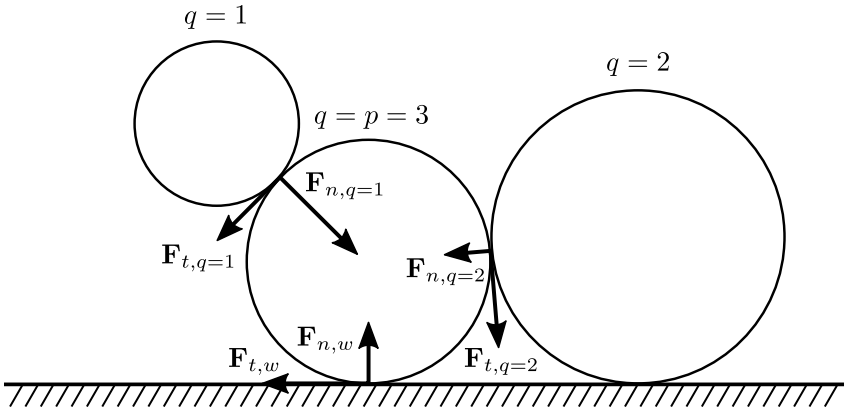

Figure 4.2: Sketch of polydisperse particles in a mobile granular bed and the resulting interactions due to collisions.

and the tangential collision forces

$$\mathbf{F}_t = \begin{cases} 0 & \zeta_n > 0 \\ \text{tangential contact model (4.10)} & \zeta_n \leq 0. \end{cases} \tag{4.2}$$

The interactions of a single particle with its environment, however, are in general more diverse. Let us consider a particle p embedded in a mobile granular bed of polydisperse, spherical particles (Figure 4.2). The dynamics of this particle are mainly determined by all the collision forces exerted upon it by particles $q, q \neq p$ as well as the wall. The total force $\mathbf{F}_{c,p}$ acting on a particle p during the collision process may be decomposed as

$$\mathbf{F}_{c,p} = \sum_{q,\, q \neq p}^{N_p} (\mathbf{F}_{n,q} + \mathbf{F}_{t,q}) + \mathbf{F}_{n,w} + \mathbf{F}_{t,w} \quad , \tag{4.3}$$

where N_p is the number of particles simulated, $\mathbf{F}_{n,q}$ and $\mathbf{F}_{n,w}$ are the normal collision forces described by (4.1) with particle q and the wall, respectively, and $\mathbf{F}_{t,q}$ and $\mathbf{F}_{t,w}$ are the tangential collision forces described by (4.2) with particle q and the wall, respectively. In what follows, the mathematical expressions are formulated for both particle-wall and particle-particle collisions, where the radii of the two colliding particles can be arbitrary.

Whenever a distinction between particle-wall and particle-particle has to be made, a reference to Appendix C.1 is given for brevity, providing all definitions and nomenclature needed to distinguish between the two different cases.

The torque $\mathbf{T}_{c,p}$ on a spherical particle p generated by the tangential contact forces is

$$\mathbf{T}_{c,p} = \sum_{q,\, q \neq p}^{N_p} R_{p,cp}\, \mathbf{n}_{p,q} \times \mathbf{F}_{t,q} + R_{p,cp}\, \mathbf{n}_{p,w} \times \mathbf{F}_{t,w} \tag{4.4}$$

where $\mathbf{n}_{p,q}$ and $\mathbf{n}_{p,w}$ are the unit vectors pointing to the collision partner q or the wall, respectively, and $R_{p,cp}$ is the particle radius at the contact point as defined per Appendix C.1 in (C.6), which accounts for surface overlap. In the next section, we will provide the mathematical description of the models used in PARTIES.

4.2 Collision modeling

4.2.1 Lubrication model

When the distance between the surfaces of two approaching particles becomes small, the fluid is squeezed out of the gap. The fluid grid cannot resolve this process as soon as $\zeta_n < 2h$, where h is the grid cell size. Hence, we employ a lubrication model, which also acts on particles rebounding after the collision, when fluid is drawn into the gap. The lubrication force is dissipative, since it is always directed opposite to the relative velocity. The model is based on the analytical derivation of Cox and Brenner [87], who solved for the force under Stokes flow conditions

$$\mathbf{F}_n = -\frac{6\pi\rho_f\nu_f R_{eff}^2}{\max\left(\zeta_n, \zeta_{n,min}\right)}\mathbf{g}_{n,cp}, \tag{4.5}$$

where R_{eff} is the effective radius accounting for polydisperse sediment and $\mathbf{g}_{n,cp}$ the normal component of the relative particle velocity as defined per Appendix C.1 in (C.1) and (C.9) respectively. The original model scales as $1/\zeta_n$ which introduces a singularity as $\zeta_n \to 0$. This has been addressed by Simeonov and Calantoni [78] and Kempe and Fröhlich [58], who set $\mathbf{F}_n = 0$ for $0 < \zeta_n < \zeta_{n,min}$, and Izard et al. [79], who have shifted the denominator of (4.5) to $\zeta_n + \zeta_{n,min}$. In the present approach, as in the approach of Costa et al. [80], lubrication forces are held constant as soon as the gap size becomes smaller than the critical value $\zeta_{n,min}$, which provides a continuous forcing on the particles when they are close to sustained contact. This parameter can be interpreted as the micro-texture of the particle surface, which acts as a surface roughness, as will be discussed further in Section 4.3.4 below.

4.2.2 Normal contact model

To account for normal contact forces, we implemented the Adaptive Collision Time Model (ACTM) proposed by Kempe and Fröhlich [58]. The main idea of the ACTM is to use an adaptive procedure to obtain the desired restitution coefficient e_{dry} and to resolve the collision on the timescale of the fluid solver. The ACTM is based on a nonlinear spring-dashpot system

$$\mathbf{F}_n = -k_n|\zeta_n|^{3/2}\mathbf{n} - d_n\mathbf{g}_{n,cp}, \tag{4.6}$$

which involves empirical parameters for the coefficients of stiffness k_n and damping d_n. Here, $\mathbf{n}$ is the normal vector pointing either towards the collision partner or towards the wall as defined per Appendix C.1 in (C.3). The nonlinear term $|\zeta_n|^{3/2}$ arises from Hertzian contact theory [88].

Since the timescale of a collision according to Hertzian contact theory is several orders of magnitude smaller than the typical temporal discretization of the fluid solver,

the collision event has to be stretched in time to maintain the efficiency of the numerical procedure. This measure is also needed for the fluid to adapt to the sudden change in the particle trajectory [58, 80]. However, the duration of contact T_c is mainly determined by the stiffness parameter k_n. This becomes of particular importance for the complex situation of bed-load transport, where a broad range of impact velocities is encountered, ranging from high-impact collisions at the top of the bed to enduring contact within the bed.

The ACTM fixes this problem by adaptively calibrating the parameters k_n and d_n depending on the impact velocity u_{in}, the desired restitution coefficient e_{dry}, and the desired collision time T_c. The latter is a parameter of the model and should be minimized to avoid excessive particle overlaps and temporal stretching. Kempe and Fröhlich [58] demonstrated that $T_c = 10\Delta t$ is a suitable choice for the collision time given that all timescales related to fluid and particle motion are significantly larger than the timescale of particle contact. For glass and hard metals, $e_{dry} = 0.97$ is a typical value [89, 77, 82]. For immersed collisions, the restitution coefficient e_{wet}, measured some small distance away from the wall, becomes a function of the Stokes number [77]. The ACTM, however, uses the IBM and lubrication model to account for e_{wet} through additional dissipative fluid effects.

In order to find values for k_n and d_n, we first neglect all non-contact forces acting on the particle so that (2.9) and (4.6) together give the following nonlinear ordinary differential equation:

$$m_{\mathit{eff}} \frac{\mathrm{d}^2 \zeta_n}{\mathrm{d}t^2} + d_n \frac{\mathrm{d}\zeta_n}{\mathrm{d}t} + k_n \zeta_n^{3/2} = 0, \tag{4.7}$$

where m_{eff} is the effective mass accounting for polydisperse sediment as defined per Appendix C.1 in (C.2). Note that $\mathrm{d}\zeta_n/\mathrm{d}t = -\mathbf{g}_{n,cp} \cdot \mathbf{n}$. Together with (4.7) and initial and final conditions, the constraints e_{dry} and T_c allow for determination of k_n and d_n

using either an iterative procedure, as was done by Kempe and Fröhlich [58], or an explicit formulation, as was proposed by Ray et al. [90]. In PARTIES, we implemented the explicit formulation, which is provided in Appendix C.2. According to Ray et al. [90], the error in u_{out} increases with decreasing e_{dry}, but does not exceed 1.3% for $e_{dry} > 0.7$ or 3% for $e_{dry} > 0.4$, making this method useful for most sediment materials such as silicate, glass, or even metal.

4.2.3 Tangential collision model

To account for frictional contact between the particles, we implemented a tangential contact model based on the linear spring-dashpot model described in the review paper of Thornton et al. [86]:

$$\mathbf{F}_{t,LS} = -k_t \boldsymbol{\zeta}_t - d_t \mathbf{g}_{t,cp}, \tag{4.8}$$

which has stiffness and damping coefficients k_t and d_t. This model uses $\mathbf{g}_{t,cp}$, the tangential component of the relative surface velocities as described in (C.10) of Appendix C.1, as well as $\boldsymbol{\zeta}_t$, the tangential spring displacement, which represents the accumulated relative tangential motion between the two surfaces:

$$\boldsymbol{\zeta}_t = \int_{t_i}^{t} \mathbf{g}_{t,cp}(t')dt', \tag{4.9}$$

where t_i is the time of impact. The discretized form of (4.9) is described in Appendix C.3.

This model limits the maximum force based on Coulomb's friction criterion:

$$\mathbf{F}_t = \min\left(||\mathbf{F}_{t,LS}||, ||\mu \mathbf{F}_n||\right)\mathbf{t}, \tag{4.10}$$

where μ represents the coefficient of friction between the two surfaces (described further in Section 4.4.3) and $\mathbf{t} = \mathbf{F}_{t,LS}/||\mathbf{F}_{t,LS}||$ points in the direction of the tangential force.

This model has two important features for simulating densely-packed beds. First, the spring allows many particles to interact in a smooth, stable manner, provided the stiffness is chosen properly. Second, the model has a memory of the friction force via the tangential displacement $\boldsymbol{\zeta}_t$, which permits a steady-state frictional bed configuration. In contrast, a model that only uses $\mathbf{g}_{t,cp}$, such as the one proposed by Kempe and Fröhlich [58], can only react to slip, not predict it.

Similarly to the ACTM, we can adaptively compute k_t and d_t for each collision. According to Thornton et al. [91], the stiffness can be set to

$$k_t = \frac{\kappa\, m_{\mathit{eff}}\, \pi^2}{T_c^2}. \tag{4.11}$$

Here, κ is based on Poisson's ratio ν:

$$\kappa = \frac{2(1-\nu)}{2-\nu}, \tag{4.12}$$

which is a well-studied material property typically ranging between $0.22 < \nu < 0.30$ [89, 82, 92]. Hence, a value of $\nu = 0.22$ was used in this chapter.

In addition, the damping is computed according to Thornton et al. [86] to account for the inelasticity of the collisions

$$d_t = 2\sqrt{m_{\mathit{eff}}\, k_t}\frac{-\ln e_{dry}}{\sqrt{\pi^2 + \ln^2 e_{dry}}}. \tag{4.13}$$

Having created a uniform collision time T_c with the normal contact model, we obtain the correct rebound characteristics for oblique impacts using these values for k_t and d_t, as shown in Section 4.4.3. Consistently, the model does not require any calibration but instead can be parameterized using material properties obtained from experiments.

4.3 Enhancements to the normal contact model

4.3.1 Motivation

In order to obtain a good agreement with immersed collision experiments, we had to implement a few enhancements to the normal contact model described in Section 4.2.2. Both changing the time integration to a scheme of higher accuracy and adding more timesteps to the integration of particle motion without changing the fluid timestep allowed us to reproduce the collision trajectories of Gondret et al. [82] in a robust manner.

4.3.2 Improved time integration

The ACTM normal contact force $\mathbf{F}_{c,p}$ is a function of the surface distance ζ_n and the relative velocity $\mathbf{g}_{n,cp}$, which in turn depend on the particle position $\mathbf{x}_p^{k-1}$ and velocity $\mathbf{u}_p^{k-1}$ at the previous substep $k-1$. We can write this functional dependence as $\mathbf{F}_{c,p}(\mathbf{x}_p^{k-1}, \mathbf{u}_p^{k-1})$. Integrating the particle equation of motion with a Forward Euler/Crank Nicholson scheme for the particle's velocity/position, we obtain:

$$\mathbf{u}_p^k = \mathbf{u}_p^{k-1} + \frac{2\Delta t \alpha_k}{m_p} \mathbf{F}_{c,p}\left(\mathbf{x}_p^{k-1},\, \mathbf{u}_p^{k-1}\right) \tag{4.14a}$$

$$\mathbf{x}_p^k = \mathbf{x}_p^{k-1} + \Delta t \alpha_k \left(\mathbf{u}_p^k + \mathbf{u}_p^{k-1}\right), \tag{4.14b}$$

where k is the number of the RK-substep and α_k is the RK-coefficient [53]. For now, we ignore the hydrodynamic, gravitational, and lubrication forces in order to focus on the contact forces alone. We conducted a simple test to analyze the accuracy of this scheme. A particle of density $\rho_p/\rho_f = 7.8$ and with radius $R_p = 10 u_\infty \Delta t$ was initialized with a velocity of $\mathbf{u}_p = (0, u_\infty, 0)^T$ at a position $y_p > R_p$ above a wall at $y = 0$. Subsequently, the particle was released and eventually collided with the wall. Neglecting hydrodynamic effects as well as gravity yields an impact velocity of $u_{in}/u_\infty = 1$. Choosing the collision

time to be $T_c = 10\Delta t$ as suggested by Kempe and Fröhlich [58], gave good results for the duration of the desired contact phase T_c, but rather large errors of the rebound velocity were observed compared to the prescribed $e_{dry} = 1$. The value of $u_{out} = -e_{dry}\, u_{in}$ was overestimated by more than 12%.

Turning our attention to Figure 4.3, we can see that the discretization of (4.14) leads to a poor estimation of the collision force $||\mathbf{F}_{c,p}||$ when compared to the simulation in which 10^4 timesteps were used to resolve the collision, which can be taken as the exact solution. This inaccuracy in the collision force was observed for a variety of simulations using different R_p, ρ_p, u_{in}, and e_{dry}. In order to reduce the error to 0.1%, a temporal discretization of $T_c = 1000\Delta t$ would be required, which is not feasible for simulations of sediment transport. Hence, we implemented a temporal discretization scheme with a higher order of accuracy. Utilizing the same three-step RK scheme that integrates the Navier-Stokes equations, we reformulated the collision integration with a predictor-corrector scheme:

$$\widetilde{\mathbf{u}}_p = \mathbf{u}_p^{k-1} + \frac{\Delta t}{m_p}\left[\gamma_k \mathbf{F}_{c,p}\left(\mathbf{x}_p^{k-1},\, \mathbf{u}_p^{k-1}\right) + \zeta_k \mathbf{F}_{c,p}\left(\mathbf{x}_p^{k-2},\, \mathbf{u}_p^{k-2}\right)\right] \tag{4.15a}$$

$$\widetilde{\mathbf{x}}_p = \mathbf{x}_p^{k-1} + \Delta t\, \alpha_k \left(\widetilde{\mathbf{u}}_p + \mathbf{u}_p^{k-1}\right) \tag{4.15b}$$

$$\mathbf{u}_p^{k} = \mathbf{u}_p^{k-1} + \frac{\Delta t\, \alpha_k}{m_p}\left[\mathbf{F}_{c,p}\left(\widetilde{\mathbf{x}}_p,\, \widetilde{\mathbf{u}}_p\right) + \mathbf{F}_{c,p}\left(\mathbf{x}_p^{k-1},\, \mathbf{u}_p^{k-1}\right)\right] \tag{4.15c}$$

$$\mathbf{x}_p^{k} = \mathbf{x}_p^{k-1} + \Delta t\, \alpha_k \left(\mathbf{u}_p^{k} + \mathbf{u}_p^{k-1}\right). \tag{4.15d}$$

Here, tilde indicates predicted values, and γ_k and ζ_k are the RK coefficients for the explicit third-order scheme according to Rai and Moin [53]. Hence, the velocity predictor step (4.15a) is third-order accurate while the other steps use second-order Crank-Nicholson schemes. A similar approach was taken by Costa et al. [80], but in this reference, the predicted value is determined by an iterative scheme, which is computationally more costly than the present scheme. In Figure 4.3 we can see that this predictor-corrector

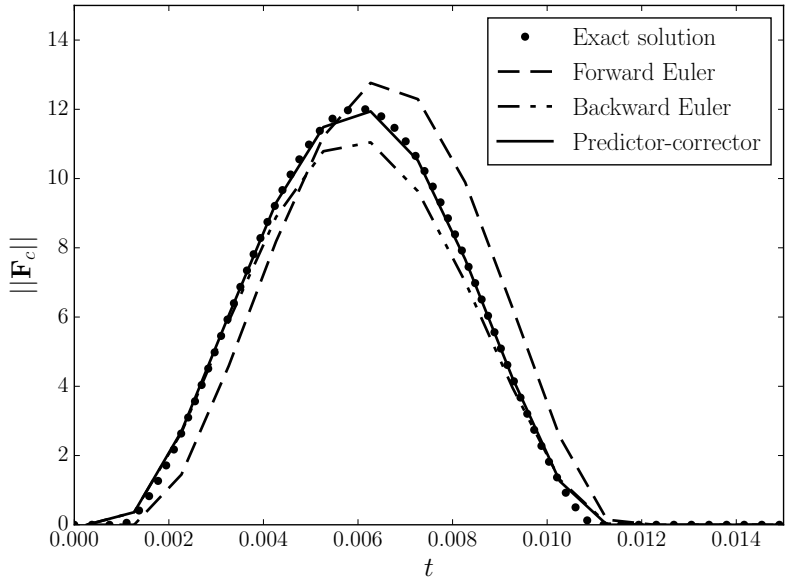

Figure 4.3: Collision forces vs. time for Forward Euler, Backward Euler, and predictor-corrector schemes.

scheme yields a much better approximation of $||\mathbf{F}_{c,p}||$ compared to the Forward Euler method, reducing the error of u_{out} by almost two orders of magnitude to 0.17% for $T_c/\Delta t = 10$. For completeness, we have also included a solution that uses the Backward Euler method, which underestimates the rebound velocity by 11%. This improvement has been achieved by a minimal increase of the computational costs, as the most expensive part of (2.9) is the computation of the hydrodynamic forces $\mathbf{F}_{h,p}$.

4.3.3 Temporal substepping

Having improved the accuracy of the contact model, we carried out simulations of particle-wall collisions in a fluid to compare to the experiments of Gondret et al. [82]. The details of the simulations, including the material properties as well as the physical and numerical parameters, are summarized in Table 4.1. Gondret et al. [82] released particles from heights large enough to accelerate to their terminal velocities before colliding with the wall. For these simulations, the horizontal wall and vertical particle trajectories

St	27	152
Re_p	30	164
R_p (m)	0.003	0.0015
u_{in} (m/s)	0.518	0.585
ρ_p/ρ_f	8.083	8.342
ν_f (m^2/s)	1.036×10^{-4}	1.070×10^{-5}
e_{dry}	0.97	0.97
g (m/s^2)	9.81	9.81
Domain size (m) ($L_x \times L_y \times L_z$)	$0.08 \times 0.16 \times 0.08$	$0.02 \times 0.2 \times 0.02$
Domain boundary conditions	p × ns × p	p × ns × p
Initial position of sphere center (m)	0.075	0.197
Grid cells in x-direction	256	128
Grid cells per diameter	19	19
Timestep	Δt = 2.5e-4	Δt = 8.9e-5

Table 4.1: Simulation parameters to match the experiments of Gondret et al. [82]. Boundary conditions can be periodic (p), slip (s), or no-slip (ns).

allow us to only consider normal collision forces. To control the impact velocity u_{in}, we accelerated the particle in the numerical simulations according to the relation

$$u(t) = u_{in}\left(e^{-40t} - 1\right), \quad \zeta_n > R_p. \tag{4.16}$$

In other words, we prescribed the falling velocity of the particle so that it accelerated in a smooth manner so that u_{in} matched the Stokes number reported in Gondret et al. [82] as shown in Table 4.1. Two scenarios were considered: one with a rather high Stokes number St = 152 and one with a lower Stokes number of St = 27, the latter of which is within the range of Stokes numbers that have been reported for the numerical simulations of Kempe et al. [71]. Once the particle reached a distance of $\zeta_n = R_p$, we turned off the prescribed velocity, allowing the particle to move on its own volition according to the hydrodynamic, buoyant, and collision forces acting on it.

While attempting to reproduce the experimental trajectories, the simulations produced large variations in the results from small changes to the initial conditions. To

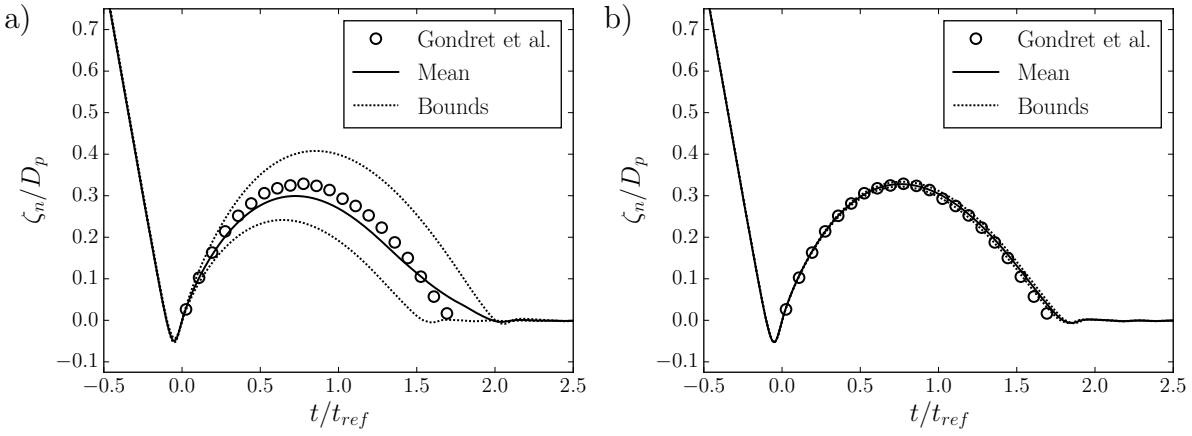

Figure 4.4: Sensitivity of rebound trajectories to initial position y_0 for St = 27. a) Trajectories computed without particle substeps and b) trajectories computed with particle substeps.

show this, we executed five simulations for St = 27, varying only the initial position of the particle y_0 from the value recorded in Table 4.1 within the interval of one grid cell h. Figure 4.4a shows the range of trajectories encountered. For St = 27, a substantial variation in the rebound height of up to 83% can be observed. We would thus expect the collision model to produce a variety of incorrect trajectories for the simulation of sediment transport in a horizontal channel flow. Even the mean of the variety of trajectories is not able to fully reproduce the experimental trajectory.

To better understand the observed variability, we plot the time evolution of the collision forces, i.e. lubrication and contact forces, for the low Stokes number case St = 27 in Figure 4.5. In this plot, we can see the particle approaching the wall with the lubrication force growing as $1/\zeta_n$ (phase I). Subsequently, the lubrication forces become zero during the contact phase starting at $t/t_{ref} = -0.1$. During this phase (phase II), the contact force grows and then decays with the particle-wall overlap as the particle changes direction to rebound. Finally, the particle experiences the lubrication force again during the rebound phase starting at $t/t_{ref} = 0$ (phase III). At this time, lubrication is acting in the opposite direction because lubrication is dissipative. The dotted line in Figure 4.5 shows

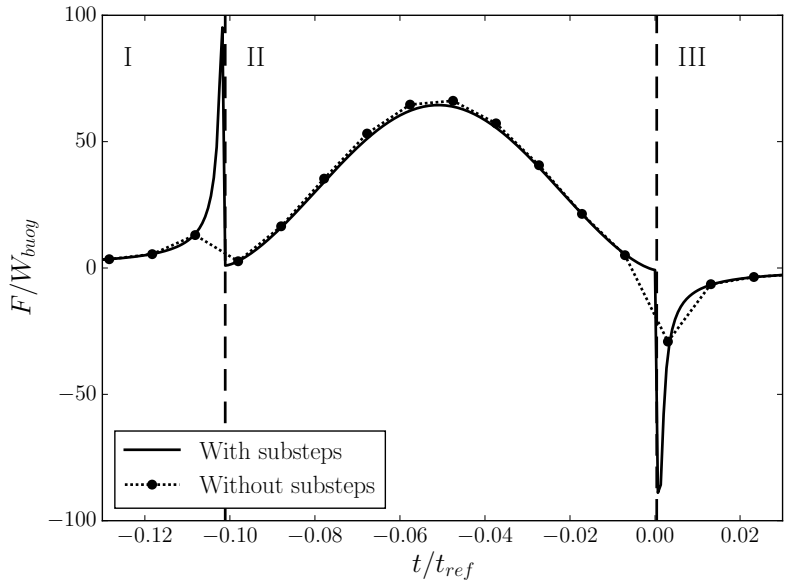

Figure 4.5: Collision forces acting on the particle at St = 27 including: the lubrication force during approach (phase I), the normal force during contact (phase II), and the lubrication force during rebound (phase III). Vertical dashed lines indicate a change in phase. $W_{buoy} = (1 - \rho_f/\rho_p)m_p\, g$ is the buoyant weight of the particle.

the forces acting on the particle for a time discretization based on CFL = 0.5 for the settling velocity. As expected, the normal contact model with the modifications described in Section 4.3.2 above is able to give a smooth evolution of contact forces with the time step size of the fluid solver. However, it turns out that the lubrication forces remain under-resolved during approach and rebound, especially as ζ_n approaches zero directly before and after the contact phase. This leads to either more or less total impulse acting on the particle, depending on where the timestep happens to land, which in turn results in variability between simulations. This effect strongly depends on the Stokes number, since the lubrication force decreases with increasing St. Hence, the ratio of the normal contact force to the lubrication force increases when approaching dry contact conditions.

Since the lubrication model used is an algebraic relation that does not depend on the surrounding hydrodynamics, we have implemented a substepping method that integrates the particle motion with smaller timesteps than the fluid motion. This method works as

follows:

1. We solve the fluid equations of motion, IBM, and hydrodynamic forces acting on the particle as normal.

2. We divide the fluid RK substep k into a number of substeps $N_{sub,k} = \{8, 2, 5\}$. This choice results in a total of 15 substeps of constant size per fluid timestep ($\Delta t_{sub} = \Delta t/15$), which is most efficient since $2\alpha_k = \{8/15, 2/15, 5/15\}$ as used in (4.15).

3. For each of the substeps, we solve the particle equations of motion with the three-step RK method. As we update the particle velocities and positions, we re-evaluate the collision (lubrication and contact) forces, but the hydrodynamic forces remain constant. This compromise makes the present approach very efficient.

4. At the end of the 8, 2, or 5 substeps, we use the final particle position and velocity for the next fluid RK substep.

This measure effectively increases the resolution of a collision to a timestep 15 times smaller than the fluid timestep to integrate particle motion, allowing us to compute the lubrication forces with higher accuracy. Since the contact duration of $T_c = 10\Delta t$ is maintained, the contact phase is now resolved with a total of 150 timesteps with only a marginal increase to the computational cost. Substepping has also been used by Kidanemariam and Uhlmann [29] and Costa et al. [80] but the authors did not illustrate the variability we have observed for the trajectories of particle-wall collisions. Meanwhile, Kidanemariam and Uhlmann [29] do not provide a comparison with the data of Gondret et al. [82] at all. The scheme presented by Costa et al. [80] still relies on an iterative procedure subdividing every fluid timestep into 50 substeps, which is less efficient than the scheme presented here. The results of our approach can be appreciated in Figure 4.5.

The solid line, which was resolved with fifteen times more timesteps, can be viewed as a better approximation of the exact solution to the model we have implemented. Figure 4.4b shows how this method almost eliminates the variability in the rebound trajectories of the particle-wall collisions discussed above.

4.3.4 Choice of particle surface roughness

As shown in Figure 4.4, the improved integration scheme described in Sections 4.3.2 and 4.3.3 yields excellent results in reproducing the rebound trajectory of the St = 27 experiment of Gondret et al. [82]. Having obtained consistent results that are insensitive to the initial condition, we can use the same setup of particle-wall collisions to select the most suitable surface roughness $\zeta_{n,min}$ for the lubrication model (4.5). This is the only parameter involved that requires calibration as an inverse problem. However, the range of values that can be assigned to $\zeta_{n,min}$ should neither fall below the surface roughness of the actual simulated particle nor exceed the length of a grid cell in order for the lubrication model to make physical sense.

The impact of $\zeta_{n,min}$ on particle rebound trajectories for St = 27 is illustrated in Figure 4.6. A clear trend can be identified: decreasing the value of $\zeta_{n,min}$ also decreases the rebound height due to more damping within the lubrication layer. However, the results are moderately sensitive to the roughness value. For instance, note that changing the roughness by an order of magnitude has a similar effect to excluding substeps (as shown in Figure 4.4). Based on the present results, we selected $\zeta_{n,min}$ = 3e-3R_p to optimize agreement with the experimental data. We have used this value for all simulations in this chapter. Note that a surface roughness of 1e-4R_p has been reported by Gondret et al. [82], and other authors have used the physical particle roughness length for this parameter [58, 80] to avoid the singularity in the lubrication force. Thus, we do not consider

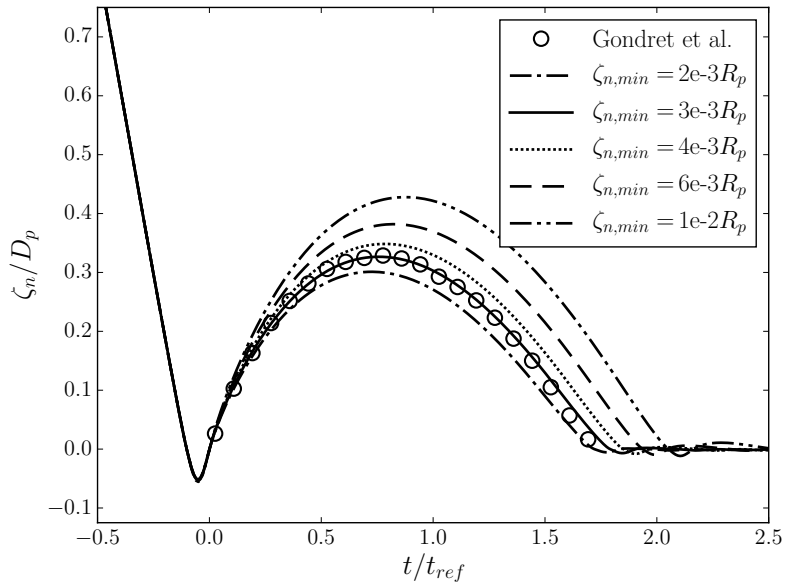

Figure 4.6: Effect of changing $\zeta_{n,min}$ on rebound trajectories for St = 27.

this parameter to be an exact physical representation of the actual surface roughness, but rather as a parameter to be calibrated within a reasonable range (small enough to be meaningful relative to the particle size and large enough to be resolved by the substeps).

4.3.5 Particle momentum balance for high Stokes number collisions

Finally, we present a clarification to the ACTM as written by Kempe and Fröhlich [58]. As already mentioned in Section 4.2.2, the ACTM assumes that (4.7) represents the equation of motion for the particle in determining the coefficients k_n and d_n. In other words, no fluid or gravitational forces act on the particle during the contact phase. Though not stated in their paper, Kempe and Fröhlich [58] excluded hydrodynamic and buoyant weight forces in order to reproduce the trajectories of Gondret et al. [82] (Kempe & Fröhlich, 2016, private communication). Thus, during contact the non-disabled Lagrangian markers still affect the fluid, but not the particle momentum. This procedure

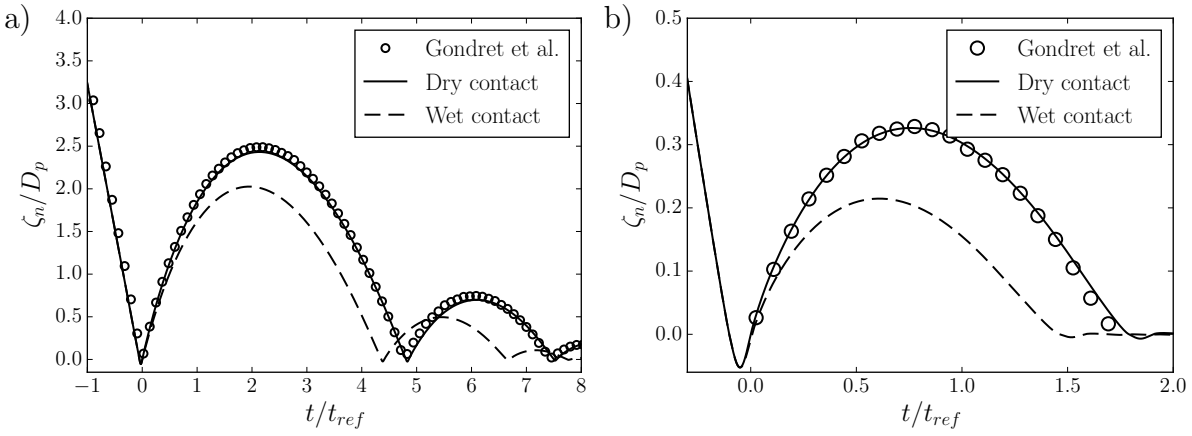

Figure 4.7: Effect of including ("wet") or excluding ("dry") fluid forces during contact on rebound trajectories. a) St = 152 and b) St = 27.

is somewhat delicate for the situation of sediment transport in a horizontal channel considering the fact that the governing nondimensional number is the ratio of the hydrodynamic stress to the buoyant weight of the particle. This characteristic number is classically known as the Shields parameter $\mathrm{Sh} = \tau_w/((\rho_p - \rho_f)gD_p)$, where τ_w is the wall shear stress [11]. It is, therefore, very desirable to include hydrodynamic and buoyant forces in (2.9) during the contact phase. In our experience, including the gravitational force during contact has a negligible effect in changing the desired T_c and e_{dry}. In fact, the results presented so far have all been generated by including buoyant weight during contact.

On the other hand, including the fluid forces during contact can lead to significant drag on the particle throughout the collision. Figure 4.7 shows how excluding fluid forces during contact gives us excellent agreement with the experimental results, while including fluid forces during contact leads to excessive damping because the fluid surrounding the particle has not been able to adapt to the change of the kinematics of the particle. Indeed, the simulations of Simeonov and Calantoni [78] show coefficients of restitution below experimental values for moderate Stokes numbers ($20 < \mathrm{St} < 100$). Hence, we

decided to follow Kempe and Fröhlich [58] and to exclude fluid forces during contact for collisions with St $\gg 1$, redefining (2.9) as follows:

$$m_p \frac{\mathrm{d}\mathbf{u}_p}{\mathrm{d}t} = \begin{cases} \mathbf{T}_{f,p} + \mathbf{F}_{g,p} + \mathbf{F}_{c,p} & \zeta_n > 0 \\ \mathbf{F}_{g,p} + \mathbf{F}_{c,p} & \zeta_n \leq 0. \end{cases} \tag{4.17}$$

Costa et al. [80] implemented a similar method for particle-wall collisions, but they turned off fluid forces when the collision overlap exceeded the expected overlap due to the particle's weight, i.e. $\zeta_n < -(1 - \rho_f/\rho_p) g m_p/k_n$. For the cases shown in Figure 4.7, the timescale of the contact phase is much smaller than the timescale of the general fluid flow, i.e. the timescale of the particle rebound. Thus, while neglecting fluid forces has an important effect on realizing the correct e_{wet}, it has a minimal effect on the general flow.

However, neglecting fluid forces can lead to unphysical situations for enduring contact, which we define to be when the timescale of contact matches or exceeds that of the general flow. Consider, for example, a single particle at rest and in contact with a wall. If we then impose a shear flow over the particle, it should be swept up into the flow, or at the very least be carried downstream. However, in a simulation using (4.17), because the particle is in contact with the wall, it does not experience the hydrodynamic forces. It will therefore continue to sit on the wall, oblivious to the flow around it, until another particle collides with it. This was addressed in Kempe et al. [71] by switching on the hydrodynamic forces for all collisions regardless of the Stokes number, even though it was not explicitly mentioned in this reference (Kempe & Fröhlich, 2016, private communication). We address this problem in detail in the subsequent Section 4.4 to introduce a suitable threshold for the inclusion of the hydrodynamic forces in (2.9) and (2.10).

4.4 Enduring contact model

4.4.1 Accounting for fluid forces

As shown in the results from Section 4.3, neglecting fluid forces acting on the particle during contact produces a good match with the experimental data of Gondret et al. [82], which involve collisions of finite duration. However, problems can arise in the limit of enduring contact. We therefore propose to include fluid forces during contact below some threshold Stokes number St_{crit}. For collisions above St_{crit}, the contact duration should be finite ($T_c = 10\Delta t$) so that no major loss of physicality is encountered. For collisions below St_{crit}, the particle is not going to experience an appreciable rebound so that the particle motion is not governed by collision forces during contact, but by hydrodynamic forces. Neglecting hydrodynamic forces in the low-Stokes number regime introduces artifacts in particle mobility. Indeed, this was observed in Vowinckel et al. [93] for the situation of a horizontal turbulent open-channel flow laden with particles heavier than their critical threshold of motion. Using the same method for collisions, these particles formed a closed bed of resting particles. In this reference, it was shown that a collision with a fast moving particle was necessary for almost all of the erosion events recorded to dislodge a particle out of the sediment packing. However, it has not been possible to clarify to what extent this triggering collision is merely a consequence of the collision procedure.

To investigate what the critical value for the Stokes number may be, we compared particle-wall collisions that include hydrodynamic forces during contact ("wet" contact) to those that exclude hydrodynamic forces during contact ("dry" contact), as illustrated in Figure 4.8. For this scenario, we used the same parameters as those summarized in Table 4.1 ($\mathrm{St} = 27$) and repeated the simulations for ever-decreasing St. The Stokes number was controlled by prescribing the particle's velocity until it made direct contact with the wall. Unlike the previous simulations, we did not allow the lubrication layer to

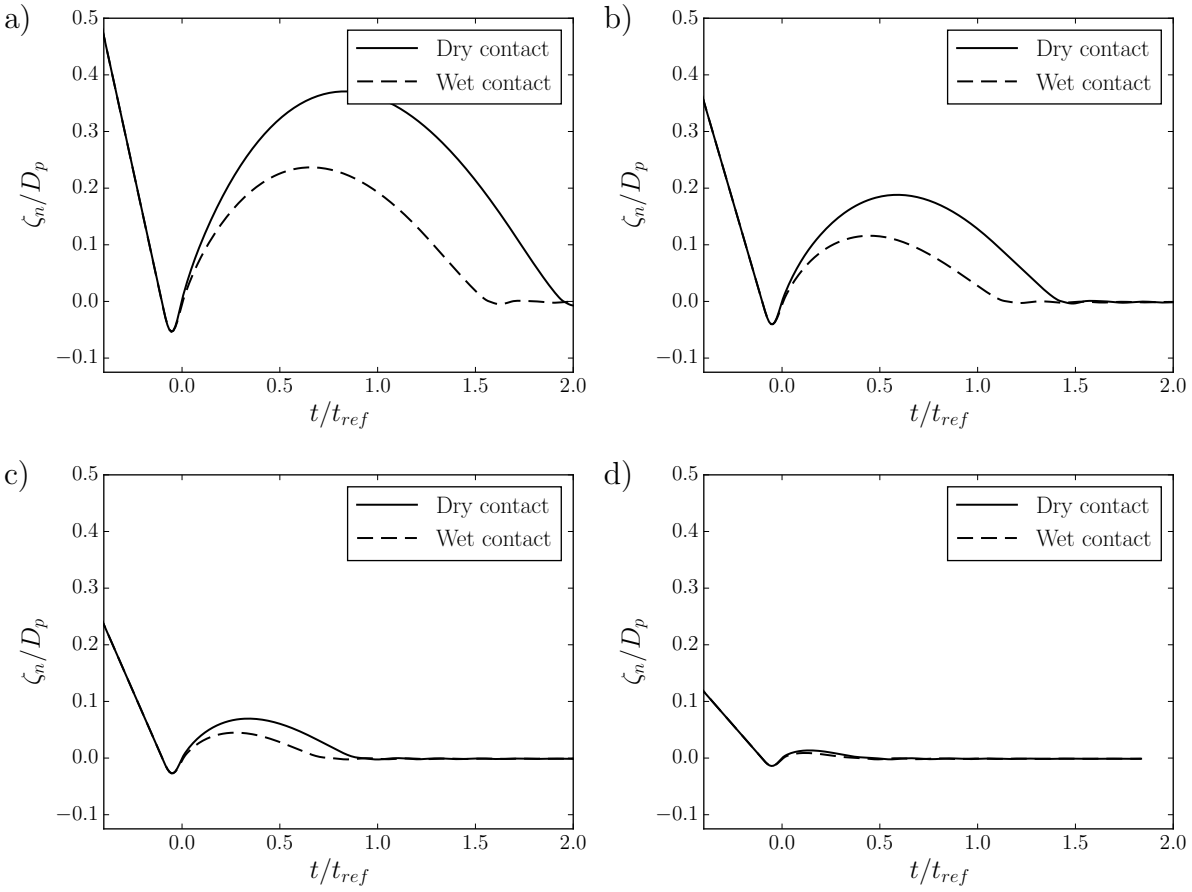

Figure 4.8: Comparison of trajectories of particle-wall collisions without ("dry") and with ("wet") hydrodynamic forces during contact for various Stokes numbers a) $St = 20$, b) $St = 15$, c) $St = 10$, d) $St = 5$, where u_{in} is measured at $\zeta_n = 0$.

slow the particle before contact.

For the cases with higher Stokes numbers, we can clearly see how including hydrodynamic forces during contact leads to significant undershooting of the rebound trajectory. As the Stokes number decreases, however, the significance of this undershooting also decreases. For St < 5 (Figure 4.8d), there is no appreciable rebound, and we consider the particle to be in enduring contact. Thus, based on these plots, we selected the critical Stokes number to be $\mathrm{St}_{crit} = 5$. This value is consistent with the work of other researchers [82, 77], who experimentally observed no rebounds for St < 10. Note that the Stokes

numbers reported in Figure 4.8 and our resulting St_{crit} are based on the particle velocity at contact, i.e. when $\zeta_n = 0$, whereas most other authors report Stokes numbers at some distance from the wall, before the lubrication layer has fully slowed the particle. With this enduring contact model, we can expand the particle equation of motion (4.17) to

$$m_p \frac{\mathrm{d}\mathbf{u}_p}{\mathrm{d}t} = \begin{cases} \mathbf{F}_{h,p} + \mathbf{F}_{g,p} + \mathbf{F}_{c,p}, & \zeta_n > 0 \\ \mathbf{F}_{g,p} + \mathbf{F}_{c,p}, & \zeta_n \leq 0 \wedge \max\{\mathrm{St}\} > \mathrm{St}_{crit} \\ \mathbf{F}_{h,p} + \mathbf{F}_{g,p} + \mathbf{F}_{c,p}, & \zeta_n \leq 0 \wedge \max\{\mathrm{St}\} \leq \mathrm{St}_{crit}, \end{cases} \tag{4.18}$$

where the $\max\{\mathrm{St}\}$ function represents the maximum Stokes number among all active collisions for particle p, and fluid forces acting on the particle are only included from non-disabled markers. The same consideration applies for the angular momentum (2.10). Using this scheme now allows us to include the full momentum balance for particles in enduring contact, i.e. the hydrodynamic stresses as well as the buoyant weight of the particle, so that the considerations of the Shields parameter become applicable.

4.4.2 Optimizing enduring particle overlap

In the case of $\mathrm{St} \ll 1$, the impact velocity u_{in} approaches zero. This means in turn that the computed stiffness in (C.11d) would approach infinity. This problem is addressed by Kempe and Fröhlich [58] who have introduced a critical Stokes number St_{crit}, which establishes a minimum impact velocity to limit k_n for enduring contact:

$$u_{in,crit} = \frac{9\mathrm{St}_{crit}\,\rho_f \nu_f}{\rho_p D_p}. \tag{4.19}$$

In the present study, this critical impact velocity was used in (C.11d) and (C.11c) to compute k_n and d_n, respectively, for such collisions. This implementation differs slightly

from that of Kempe and Fröhlich [58], who do not apply any damping for collisions with $\mathrm{St} < \mathrm{St}_{crit}$, i.e. they have set $d_n = 0$. We included this damping for enduring contact in order to help reach steady-state conditions. Our implementation also differs in that we use $\mathrm{St}_{crit} = 5$ whereas Kempe and Fröhlich [58] used $\mathrm{St}_{crit} = 1$.

Furthermore, we retain the buoyant weight forces in the equation of motion during contact as outlined in Section 4.3.5. This means that, for particle packings several diameters thick, the weight of a single sphere resting on another layer of particles is passed along to deeper layers. This effect enhances the physical realism because frictional contact forces increase with depth, but it also results in increasing particle surface overlap with depth and ultimately in a change of porosity of the sediment bed, which has been acknowledged as a crucial parameter to define the hydraulic resistance of a sediment to the flow [28]. However, a flow with a lower Reynolds number would result in collisions with lower Stokes numbers such that $u_{in,crit}$ could become large relative to the particle size and relevant time scales. A large $u_{in,crit}$ would result in a low k_n and hence a large overlap between particles, which is undesirable. To prevent this large overlap, we enforce a maximum overlap distance ϵR_p through the following procedure: for a collision with $\mathrm{St} < \mathrm{St}_{crit}$, the stiffness is given by

$$k_n = \begin{cases} \frac{m_{\mathit{eff}}}{\sqrt{u_{in} t_*^5}} & u_{in} > u_{in,crit} \\ \max\left(k_{n,crit},\, k_{n,grav}\right) & u_{in} < u_{in,crit} \end{cases} \tag{4.20}$$

where m_{eff} and t_* are defined in (C.2) and (C.11b), respectively,

$$k_{n,crit} = \frac{m_{\mathit{eff}}}{\sqrt{u_{in,crit} t_*^5}} \tag{4.21}$$

Case	Dry oblique collision	Rolling in shear flow
R_p	0.00159	0.0625
ρ_p/ρ_f	2500	2.5
e_{dry}	0.83	0.97
ν	0.22	0.3
μ_k	0.11	0.15
μ_s	0.8	0.8
g	0	9.81
ν_f	0	0.02
Timestep	$\Delta t = 2\text{e}{-5}$	CFL = 0.5

Table 4.2: Simulation setup for oblique and rolling sphere simulations.

is the stiffness limited by the critical impact velocity, and

$$k_{n,grav} = \max\left[m_p g(\epsilon R_p)^{-3/2},\, m_q g(\epsilon R_q)^{-3/2}\right] \tag{4.22}$$

is the stiffness required for particle p (or q) to have a steady-state overlap of ϵR_p (or ϵR_q) with a wall due to gravity. To have a minimal constant overlap we set $\epsilon = 10^{-3}$. Thus, we ensure that a bed of particles contains a uniform set of collision stiffnesses that minimize particle overlap.

4.4.3 Rolling and sliding motion

The coefficient of friction for a material can depend on whether the contact is rolling or sliding [94]. The rolling condition implies zero slip at the contact point, i.e. $\|\mathbf{g}_{t,cp}\| = 0$ (cf. C.1). As a consequence, particle surfaces are in sticking contact for rolling motion until a critical threshold of static friction $F_s = \mu_s\|\mathbf{F}_n\|$ is exceeded, where μ_s is the coefficient of static friction. As soon as this condition is met, significant slip occurs and the contact condition changes from sticking to sliding, so that the threshold for kinetic friction $F_k = \mu_k\|\mathbf{F}_n\|$ must be used, where μ_k is the coefficient of kinetic friction, with μ_s always greater than μ_k. Apart from the physical reasoning presented above, limiting the

frictional forces also becomes important from a numerical point of view whenever two or more collision partners are involved. Otherwise the multiple contact points competing for no-slip conditions can lead to instabilities in the calculation of the frictional forces.

In PARTIES, the distinction between rolling/sticking and sliding is made by the following scheme, which is comparable to that of Luding [95]:

- While the particle is sticking, i.e. $||\mathbf{F}_{t,LS}|| < ||\mu \mathbf{F}_n||$, we set $\mu = \mu_s$ to test for the onset of slipping.
- Once slipping occurs, i.e. $||\mathbf{F}_{t,LS}|| > ||\mu \mathbf{F}_n||$, we set $\mu = \mu_k$ until the friction force falls below the Coulomb friction force.

The aim of the present study is to simulate natural sediment. Hence we parametrized the coefficients of friction with typical values of silicate materials, yielding $\mu_k = 0.15$ based on the work of Joseph and Hunt [92], who worked with glass spheres, and $\mu_s = 0.8$ based on the work of Dieterich [96], who found values ranging from 0.75 to 0.85 for different rock materials like quartz, granite, and sandstone.

We have validated the tangential collision model using an oblique dry impact experiment, i.e. neglecting hydrodynamic forces, by Foerster et al. [89], whose parameters are summarized in Table 4.2. Figure 4.9 shows that our simulations compare well to the experiments in reproducing the rebound angle

$$\psi_{out} = \frac{u_{t,out}}{u_{n,in}}, \tag{4.23}$$

which depends on the impact angle

$$\psi_{in} = \frac{u_{t,in}}{u_{n,in}}. \tag{4.24}$$

Here, $u_{n,in}$ is the impact velocity normal to the wall, while $u_{t,in}$ and $u_{t,out}$ are the impact

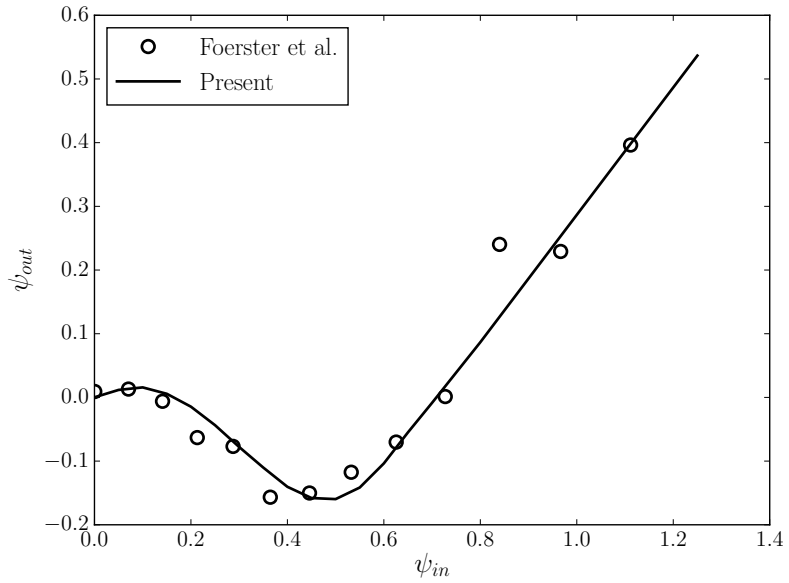

Figure 4.9: Rebound vs. impact angles for a particle-wall oblique collision.

and rebound velocities, respectively, of the particle's contact point tangential to the wall ($u_t = u_p + R_p\,\omega_{p,z}$ for a particle obliquely colliding in the x-direction). For a particle with no initial rotation, ψ_{in} is the tangent of the angle the particle makes with the wall from the normal ($\psi_{in} = 0$ means no relative tangent motion). The rebound angle is zero when the contact is sticking perfectly at the time of release. However, the rebound angle is negative when, at the point of release, $|u_p| < |\omega_{p,z}|$ (since $\omega_{p,z} < 0$ for our example). The linear-spring tangential collision model is able to perfectly capture these negative values for ψ_{out} at low impact angles.

To test both situations, rolling and sliding, we simulated a particle in a Couette flow. We placed a sphere of radius $R_p/H = 0.0625$ on the bottom wall of a channel of height H. We initialized the particle at rest at a distance $\zeta_n/R_p = 1.6 \times 10^{-5}$ above the bottom wall. We subsequently exposed the sphere to a linear shear flow, holding it fixed for a short time ($tU/H = 0.01$) to allow the flow to develop around it before releasing it. The numerical parameters are summarized in Table 4.2. We found that slipping motion

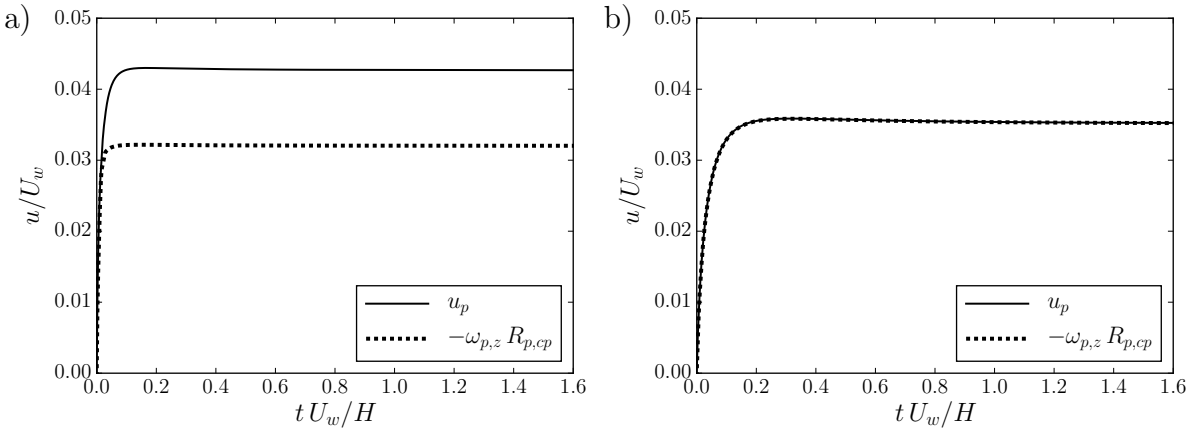

Figure 4.10: Translational and rotational velocities of a particle exposed to a linear shear flow. a) sliding motion for $Re_H = 10$ and b) rolling motion for $Re_H = 50$.

occurs for a lower Reynolds number of $\mathrm{Re}_H = UH/\nu_f = 10$, where U is the lid velocity. On the other hand, perfect rolling motion occurs at $\mathrm{Re}_H = UH/\nu_f = 50$.

Figure 4.10 shows how the particle accelerates until it reaches a steady-state translational velocity. As soon as the particle makes contact with the wall, gravity holds it there with a slight overlap according to the conditions defined in Section 4.4.2. Accounting for fluid forces during contact allows the particle to accelerate to a steady-state speed while in contact with the wall. As expected the particle achieves perfect rolling without slip (Figure 4.10b), marked by the match between the translational velocity u_p and the rotational velocity relative to the particle center $-\omega_{p,z}\,R_{p,cp}$. Accordingly, the particle shows significant slip for the lower Reynolds number (Figure 4.10a), where the increased viscosity leads to increased drag on the particle, which in turn overpowers the friction from the particle's weight.

4.5 Conclusions

In this chapter, we presented and validated a contact model for the purpose of phase-resolved Direct Numerical Simulations, in which the disperse phase is represented by the Immersed Boundary Method. The present modeling approach allows for actual particle contact and takes all relevant contact forces into account without introducing parameters that require arbitrary calibration. These forces include lubrication forces for small inter-particle gaps, normal repulsive forces to resolve inelastic collisions, and tangential forces to represent particle friction. We demonstrated that an improved integration scheme is necessary to obtain consistent results for particle-wall collisions. Subsequently, we presented enhancements that extend the model to deal with simulations of flows over dense granular sediments. It turns out that these enhancements are crucial in order to deal with thick sediment packings. The measures taken should allow us to generate sediment packings several diameters thick that are numerically stable as the packing reaches a steady-state condition. The simulations are performed by retaining the full momentum balance of a particle in enduring contact, which includes the hydrodynamic forces and the buoyant weight of a particle. Including these forces is crucial to represent phenomena like erosion and resuspension of particles. Moreover, the enhanced model allows for rolling and sliding contact, distinguishing between sticking and sliding conditions.

Altogether, the present approach yielded excellent agreement with the benchmark test cases for binary collisions. In the next chapter, we will evaluate our approach for situations involving many particles using benchmark cases for an erodible particle bed.

Chapter 5

Flow over a dense sediment bed

5.1 Introduction

In Chapter 3, we presented our implementation of the IBM, which couples the interactions between the fluid and particles, and then validated it against experiments of single sedimenting spheres. In Chapter 4, we developed a collision model for polydisperse spheres to account for close particle-particle and particle-wall interactions. We then validated our collision model against experiments involving single spheres. We are ultimately interested, however, in simulations of particle beds involving the interactions of many particle. This chapter will focus on the validation of the hydrodynamic and collisional interactions for thousands of particles in a sediment bed configuration, allowing us to later analyze the physics of such flows.

For our validation, we will focus on a laminar flow over a bed of particles. Several groups have conducted experiments for such flows. Lobkovsky et al. [17] and Aussillous et al. [19] carried out pressure-driven experiments in a linear flume where they controlled the fluid flow rate over a bed of particle that eroded over time. Houssais et al. [20] and Allen and Kudrolli [97] conducted experiments in a circular tank sheared by a rotating

lid, allowing them to study long-term steady-state bed behavior. The latter two studies, however, involve time scales that would be computationally expensive to simulate with our methods. For this reason and because they accounted for the effects of the side walls, which allow our simulations with periodic boundaries to more closely match their results, we have chosen to use the experiments of Aussillous et al. [19] as a benchmark study.

In this chapter, we will first carry out a convergence test for a laminar pressure-driven flow over a bed of particles, which will establish the consistency of our methods and provide information regarding appropriate grid resolutions for similar types of simulations. Then, we will present a detailed validation of our simulation results with wall-normal profiles of the fluid and particle velocities as well as bulk flow quantities using the experimental data of Aussillous et al. [19].

5.2 Convergence test

5.2.1 Simulation setup

The simulation we consider here involves a pressure-driven flow over a particle bed that can be mobilized. The domain has dimensions $L_x = 10D_p$ in the streamwise direction, $L_y = 20D_p$ in the vertical direction, and $L_z = 10D_p$ in the spanwise direction. We initialize the simulation by allowing $N_{p,m}$ mobile particles to settle under gravity and without fluid (i.e. a "dry" simulation) onto a bed of $N_{p,f}$ fixed particles, which are arranged in a hexagonal spacing pattern in the xz-plane and whose heights above the lower wall vary randomly by D_p. The number of particles was chosen such that initially the particle bed is about $h_p = 10D_p$ deep with a clear fluid height of $h_f = 10D_p$ above it. A parabolic velocity profile was initialized in the clear fluid layer above the particles with a bulk velocity of $u_{bulk} = \frac{1}{h_f}\int_{h_p}^{L_y} u \, \mathrm{d}y = 1$ and a constant pressure gradient $f_{b,x} = 1$

Ga	0.850
Re_{ref}	3.16
D_p	0.1
ρ_p/ρ_f	2.1
ν_f (m^2/s)	0.1
$\zeta_{n,min}/D_p$	1.5e-3
e_{dry}	0.97
μ_k	0.15
μ_s	0.8
g (m/s^2)	6.57
Domain size ($L_x/D_p \times L_y/D_p \times L_z/D_p$)	$10.0 \times 20.0 \times 10.0$
Domain boundary conditions	p × ns × p
$N_{p,m}$	1071
$N_{p,f}$	100
Initial h_f/D_p	10.0

Table 5.1: Simulation parameters for convergence test. Boundary conditions are periodic (p) or no-slip (ns).

$N = L_x/h$	96	128	192	256	384	512
D_p/h	9.6	12.8	19.2	25.6	38.4	51.2
Δt	5e-4	5e-4	5e-4	5e-4	5e-4	5e-4

Table 5.2: Grid resolutions for convergence test.

was applied to the flow. The particle bed, which was initially at rest, then began to erode at the bed/clear fluid interface. Other parameters associated with the simulation are provided in Table 5.1.

For the convergence test, the simulation was run at a variety of grid resolutions ranging from $D_p/h = 9.6$ to $D_p/h = 51.2$, where h is the grid spacing. A constant step size of $\Delta t =$ 5e-4 was used for all the simulations, which corresponds to a CFL value of 0.5 for the highest-resolution simulation.

5.2.2 Results

To analyze the convergence rate, we will first consider the volumetric particle flux, given by

$$q_p = \frac{1}{L_y L_z} \sum_{p=1}^{N_{p,m}} V_p u_{p,x}, \tag{5.1}$$

where V_p is the volume of particle p, and $u_{p,x}$ is the velocity in the x-direction of particle p. For nondimensionalization, we will use a reference length of D_p, a reference velocity,

$$u_{ref} = \sqrt{\frac{f_{b,x}\, D_p}{\rho_f}}, \tag{5.2}$$

which is based on the driving pressure gradient $f_{b,x}$, and a reference time,

$$t_{ref} = D_p / u_{ref}. \tag{5.3}$$

This reference velocity and time allow us to use concrete values based on the input simulation parameters, rather than values obtained *a posteriori* from the simulation, which may vary from one run to the next. We can then characterize the simulation using a Reynolds number based on the reference velocity

$$Re_{ref} = \frac{u_{ref} D_p}{\nu_f}, \tag{5.4}$$

and the Galileo number

$$\mathrm{Ga} = \frac{\sqrt{(\rho_p/\rho_f - 1) g D_p^3}}{\nu_f}, \tag{5.5}$$

which are both shown in Table 5.1.

Figure 5.1 shows the flow rate as a function of time for the different grid resolutions. There is an initial spike in the flow rate as the entire bed moves and reconfigures into a

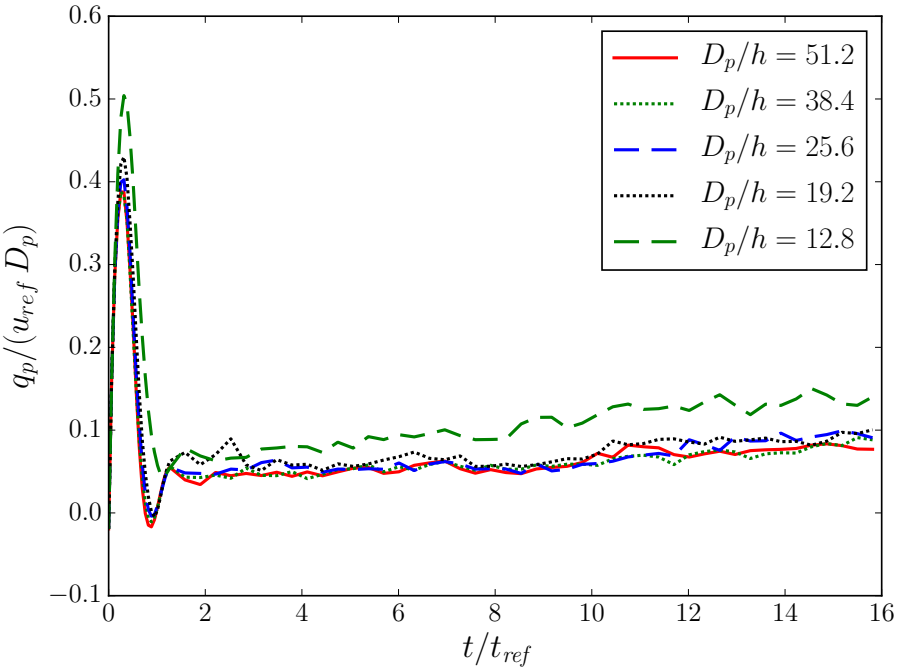

Figure 5.1: Particle flux, q_p, as a function of time.

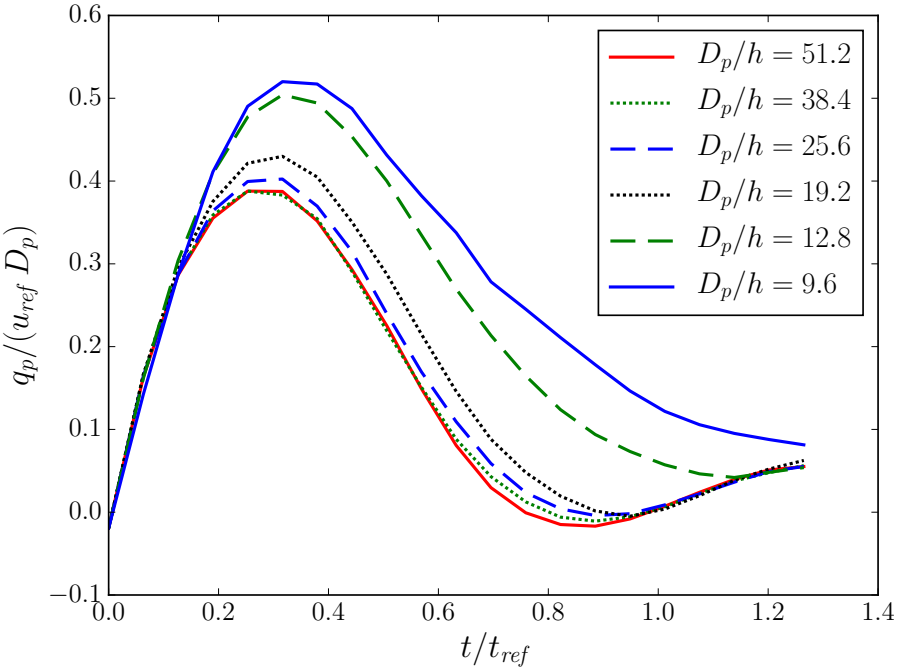

Figure 5.2: Particle flux, q_p, as a function of time during the initial bed movement.

locked state, after which the flow rate drops and then slowly increases in time as the flow pushes particles at the bed surface downstream. Aside from a marked difference in the flow rate at $D_p/h = 12.8$, we cannot draw any conclusions regarding convergence from this plot. The different trajectories arise from the system being chaotic; slight numerical differences and even machine precision can result in particle moving in a different direction after a collision. Thus, to show any reasonable convergence, we would have to run the simulation for a very long time to reach statistical convergence, which would be very costly.

If we look at the initial flow rate spike, however, we can see more of a pattern between the different flow rates. Figure 5.2 shows a zoom on this region. Here we can clearly see a convergence pattern when the flow is still deterministic. The simulation seems pretty well converged at a resolution of $D_p/h = 38.4$, though the resolutions $D_p/h = 25.6$ and $D_p/h = 19.2$ have reasonable errors, 7.5% and 19%, repectively (see Figure 5.3). In order to obtain a quantitative measure, we can compare the convergence to the highest resolution result ($N = 512$). We thus define the error in q_p as

$$e_{q_p} = \sqrt{\frac{\int_0^{T_f} \left(q_p - q_{p,N=512}\right)^2 \mathrm{d}t}{\int_0^{T_f} \left(q_{p,N=512}\right)^2 \mathrm{d}t}}, \tag{5.6}$$

where the final time $T_f/t_{ref} = 1.26$ for the particle fluxes in Figure 5.2. The resulting errors using this value for T_f are shown in Figure 5.3.

The error in the flow rate appears to follow a trend that is third-order accurate. This result is a bit unexpected, since the methods we employ are generally second-order in space. We could look at some other metrics for the error, such as the error in the average

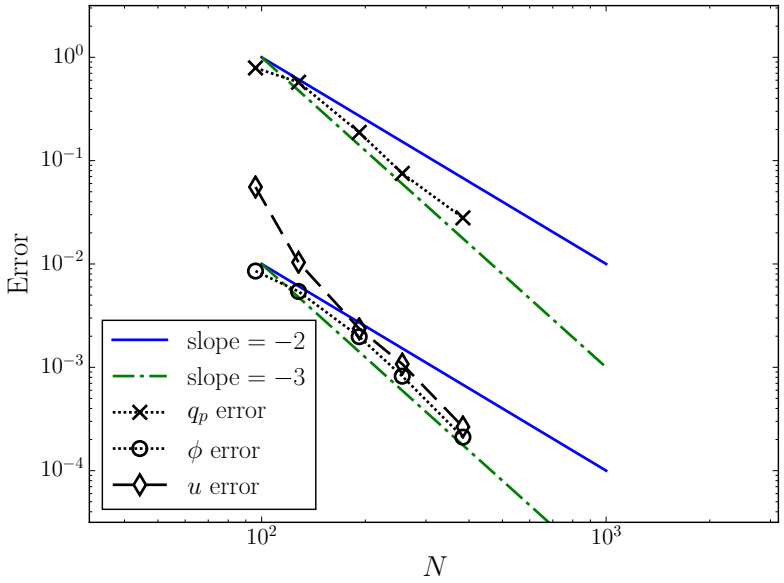

Figure 5.3: Convergence of errors in the particle flux, e_{q_p}, the volume fraction, e_ϕ, and the streamwise fluid velocity, e_u.

streamwise fluid velocity

$$e_u = \sqrt{\frac{\int_0^{L_y} \left(\overline{\langle u \rangle} - \overline{\langle u \rangle}_{N=512}\right)^2 \mathrm{d}y}{\int_0^{L_y} \left(\overline{\langle u \rangle}_{N=512}\right)^2 \mathrm{d}y}}, \tag{5.7}$$

where $\overline{\langle u \rangle}$ is the x-component of the fluid velocity outside the particles averaged in the streamwise and spanwise directions and time:

$$\overline{\langle u \rangle} = \frac{1}{T_f} \int_0^{T_f} \left(\frac{\int_0^{L_z} \int_0^{L_x} (1-\phi) u_x \, \mathrm{d}x \mathrm{d}z}{\int_0^{L_z} \int_0^{L_x} (1-\phi) \, \mathrm{d}x \mathrm{d}z} \right) \mathrm{d}t, \tag{5.8}$$

where $T_f/t_{ref} = 1.26$ is the same averaging time as the one used for calculating e_{q_p}. We can also look at the error in the volume fraction

$$e_\phi = \sqrt{\frac{\int_0^{L_y} \left(\overline{\langle \phi \rangle} - \overline{\langle \phi \rangle}_{N=512}\right)^2 \mathrm{d}y}{\int_0^{L_y} \left(\overline{\langle \phi \rangle}_{N=512}\right)^2 \mathrm{d}y}}, \tag{5.9}$$

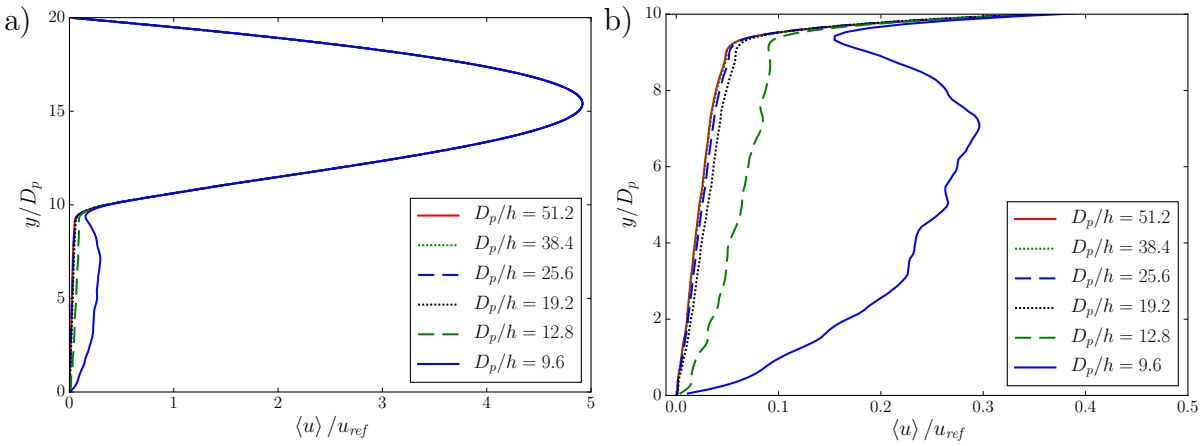

Figure 5.4: Fluid velocity profiles averaged in spanwise and streamwise directions and time for different grid resolutions. Shown are a) the full velocity profile and b) a zoom on the mobile bed layer. The reference velocity, u_{ref} is given by (5.2).

where $\overline{\langle\phi\rangle}$ is the solid volume fraction averaged in the streamwise and spanwise directions and time:

$$\overline{\langle\phi\rangle} = \frac{1}{T_f L_x L_z} \int_0^{T_f} \int_0^{L_z} \int_0^{L_x} \phi \, \mathrm{d}x \mathrm{d}z \mathrm{d}t. \tag{5.10}$$

Figure 5.3 likewise shows third-order convergence in the velocity and volume fraction errors.

One possible explanation for the higher-than-expected convergence is our use of disabling Lagrangian markers. Part of our collision strategy, as discussed in Section 4.1.1, is that we turn off Lagrangian markers for two particles when their interpolation/spreading stencils overlap. We implement this strategy in order to prevent markers from competing for enforcing their respecting boundary conditions, which seems to work well, especially when considering the situation of a single particle colliding with a wall. Problems arise, however, for situations involving many particles in close proximity to one another, such as in a sediment bed. In this case, many markers might be turned off. In fact, at low grid resolutions, most of the markers might be turned off. As the grid resolution increases, however, the percentage of turned-off markers decreases.

One effect of markers being turned off within the bed is that a flow is permitted to develop through the particles as if they were porous. This effect can be seen in Figure 5.4, which shows the streamwise fluid velocity at the different grid resolutions. At the lowest resolutions, $D_p/h = 9.6$ and $D_p/h = 12.8$, a significant porous flow exists within the sediment bed due to the fluid moving through the gaps opened up by the turned-off Lagrangian markers. This flow is significantly reduced for $D_p/h = 19.2$ and is almost negligible above resolutions of $D_p/h = 25.6$. Thus, having more markers acting along the particle surface can significantly increase the accuracy of the simulations, potentially resulting in an accuracy that is higher than second-order. For simulations involving a sediment bed, we will use grid resolutions of $D_p/h = 20$ to $D_p/h = 25$.

5.3 Validation with experiments

5.3.1 Physical setup

We presented a detailed validation of binary particle-wall collisions in Sections 4.3 and 4.4. To address the bulk behavior of a dense granular bed sheared by a laminar Poiseuille flow, we carried out numerical simulations to reproduce the experimental results of Aussillous et al. [19], who studied pressure-driven flows over glass spheres with a mean diameter $D_p = 1.1$mm and a standard deviation of $\sigma(D_p) = 0.1$mm as sediment material. This experimental work provides investigations over a range of submergences h_f/D_p and Reynolds numbers in the laminar regime, where h_f is the height of the clear-water layer above the sediment bed illustrated in Figure 5.5. We define h_f to be the height above which the average particle volume fraction $\phi < 0.05$, which is the threshold for negligible impact of particle-particle interaction on the flow [98]. We define the mobile bed height h_m to be the portion of the particle bed above which the mean particle velocity is higher

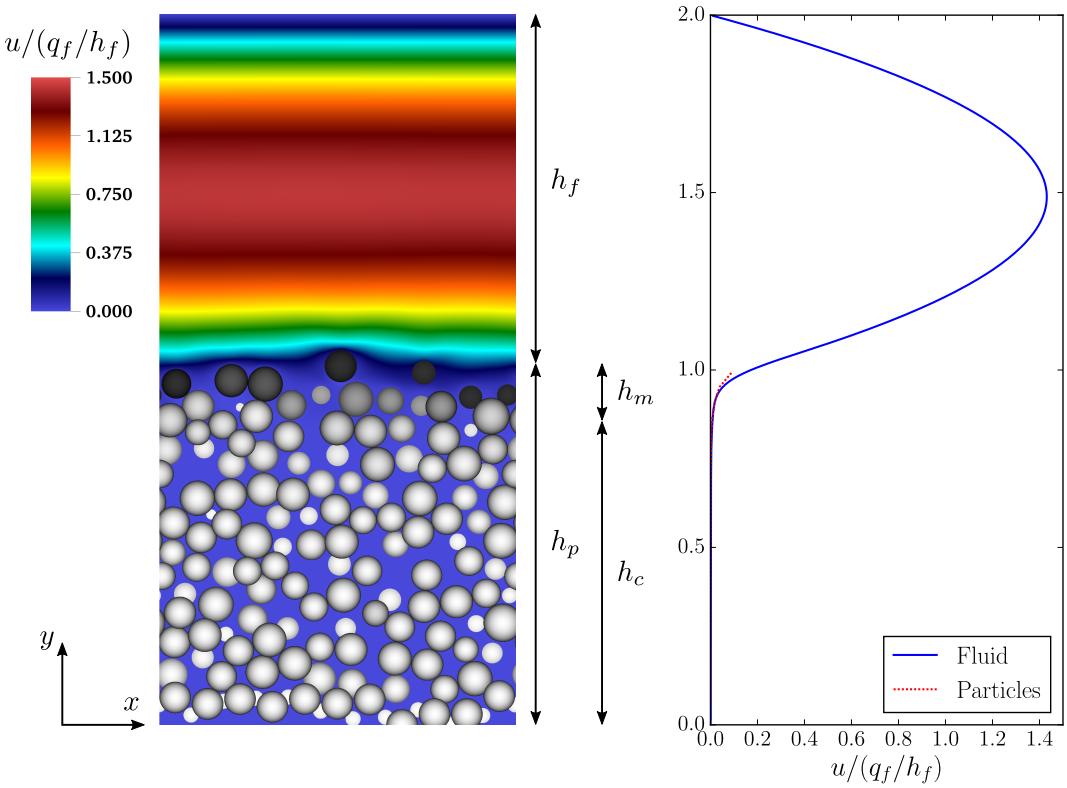

Figure 5.5: Left plot: Instantaneous snapshot of a slice through the xy-plane for case A10M. Contours show the streamwise component of the fluid velocity. Particles are colored grayscale according to their velocity: black fast, white slow. Right plot: Streamwise and spanwise averages of fluid and particle velocities. Arrows correspond to the length scales for the clear fluid, h_f, the particle bed, h_p, the mobile bed layer, h_m, and the motionless bed layer, h_c.

Ga	0.397
R_p (m)	0.0444
ρ_p/ρ_f	2.1
ν_f (m^2/s)	0.219
g (m/s^2)	9.81
e_{dry}	0.97
$\zeta_{n,min}/R_p$	3.0×10^{-3}
μ_k	0.15
μ_s	0.8
Domain size (m) ($L_x \times L_y \times L_z$)	$1.0 \times 2.0 \times 1.0$
Domain boundary conditions	p $\times$ ns $\times$ p
Grid cells in x-direction	256
D_p/h	22.7
Volume fraction in center of bed	0.609
Timestep	CFL = 0.1

Table 5.3: Simulation parameters to match the experiments of Aussillous et al. [19]. Boundary conditions are periodic (p) and no-slip (ns). The Galileo number Ga is defined in (5.5).

than 1% of the value at the fluid/particle interface.

In their experiments, Aussillous et al. [19] filled a long chamber with particles and then applied a constant pressure gradient, which eroded the particles from the chamber. Initially, the fluid height h_f was small and the pressure gradient drove a large number of particles so that the height of the mobile bed layer, h_m in Figure 5.5, was large. Since no new particles were added to the chamber, h_f increased as the particles eroded away until, at long periods of time, the experiment reached a steady-state configuration where the influx of particles into the observation window remained in equilibrium with the outflux. Due to our use of periodic boundary conditions, we will only try to replicate the long-term steady-state flow conditions, of which there are only a few data from Aussillous et al. [19]

We executed several simulations in an attempt to match four of the experiments of Aussillous et al. [19] at different flow rates and fluid heights. The physical and numerical

Case	A1	A2	A9	A10	A10M
Re_b	0.301	0.402	1.01	1.15	1.15
h_f/D_p (Exp.)	7.05 ± 0.5	8.15 ± 0.5	10.29 ± 0.5	11.27 ± 0.5	11.27 ± 0.5
h_f/D_p (Sim.)	7.15	8.31	10.33	11.29	11.05
Sh (Exp.)	0.24 ± 0.03	0.24 ± 0.03	0.37 ± 0.04	0.35 ± 0.03	0.35 ± 0.03
Sh (Sim.)	0.224	0.222	0.358	0.343	0.357
q_f (m^2/s)	0.0659	0.0880	0.220	0.251	0.251
$N_{p,m}$	2031	1870	1559	1419	1407*
$N_{p,f}$	132	132	132	132	132
T_{avg} (s)	139.5	137.9	126.2	127.3	111.0

Table 5.4: Parameters that vary between the different cases. The bulk Reynolds number Re_b is defined in (5.11) and the Shields number Sh is defined in (5.12). The fluid height h_f (and hence Shields number) do not exactly match between the experiments (Exp.) and simulations (Sim.). *Polydisperse particle diameters follow a Gaussian distribution with a standard deviation of $\sigma(D_p) = 0.1D_p$.

parameters associated with these simulations are listed in Table 5.3, and the differences between the four cases are listed in Table 5.4. These experiments can be characterized by the Galileo number (5.5) and the bulk Reynolds number

$$\mathrm{Re}_b = \frac{q_f}{\nu_f}, \tag{5.11}$$

where q_f is the fluid flow rate, and the Shields number

$$\mathrm{Sh} = \frac{6\mathrm{Re}_b}{\mathrm{Ga}^2}\left(\frac{D_p}{h_f}\right)^2, \tag{5.12}$$

which represents the ratio of the shear stress acting on the particle bed to the buoyant weight of a particle. Aussillous et al. [19] reported an uncertainty for the determination of the bed height as $h_f \pm R_p$, which we have included in Table 5.4 as the deviations in h_f and Sh, which depends on h_f.

We required a low CFL = 0.1 in order to maintain the stability of the fluid-particle coupling. This restricted CFL value was necessary to avoid numerical instabilities arising

from the simultaneous particle-particle interactions of a multitude of particles within the thick sediment bed. We also used a grid resolution of $D_p/h = 22.7$ to resolve the interstitial flow, though we did not see any appreciable difference in the bulk flow properties for a coarser discretization of $D_p/h = 17.0$.

We generated the initial sediment bed using a precursor simulation, in which we randomly distributed $N_{p,m}$ particles in a computational domain with periodic x- and z-boundaries above a layer of $N_{p,f}$ fixed particles, which we arranged in a hexagonal packing with random heights varying from $0 < y_0 < D_p$. These fixed particles were used to avoid over-idealized smooth conditions at the lower wall. We subsequently allowed the non-fixed particles to settle under "dry" conditions, i.e. without considering hydrodynamic forces. We then applied a large pressure gradient to produce a fluid flow rate 8 times that of the final desired flow rate, mobilizing the entire bed. This mobilization also caused the bed to dilate, or have the average local volume fraction decrease, which in turn decreased h_f. Once h_f dropped to about $0.15D_p$ below the desired value, we immediately decreased the flow rate to the final flow rate reported in Table 5.4, which is defined as

$$q_f = \frac{1}{L_x L_z} \int_0^{L_z} \int_0^{L_y} \int_0^{L_x} (1-\phi) u \, \mathrm{d}x \, \mathrm{d}y \, \mathrm{d}z, \tag{5.13}$$

where ϕ is the particle volume fraction. We adopted this procedure because we noticed a hysteresis in the particle flux between an increased flow rate and a decreased flow rate, which has also been observed by Clark et al. [99]. Note that this procedure more closely resembles the experiments, where the particle bed is largely mobilized and then settles into a lower particle flux.

However, one problem with this procedure is that we cannot determine the final bed height *a priori*. The dilation and contraction accompanying the two flow rates is difficult to predict without executing an iterative procedure of running simulations with varying

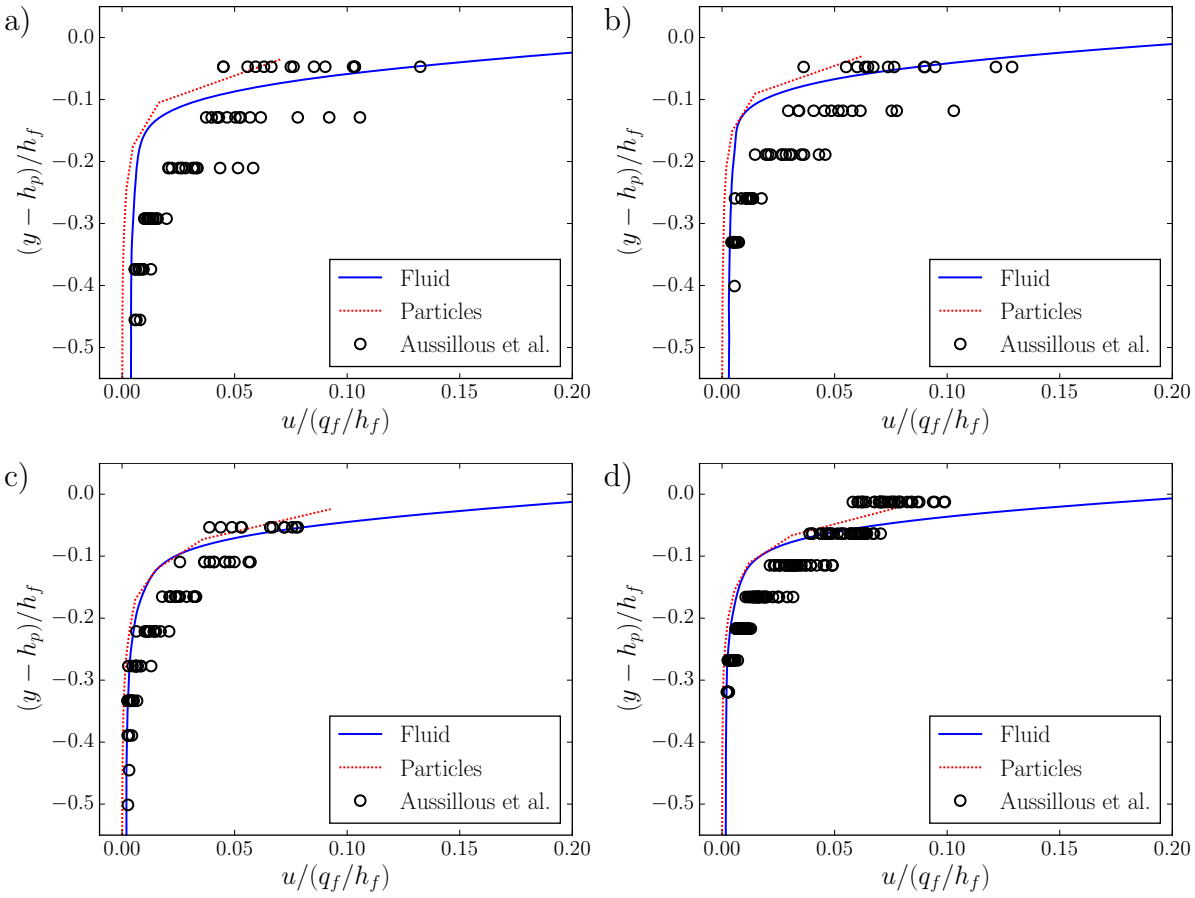

Figure 5.6: Wall-normal profiles of average fluid and particle velocities near the particle/fluid interface compared to the wall-normal particle velocity profile from Aussillous et al. [19]. a) Case A1, b) Case A2 c) Case A9 d) Case A10.

numbers of particles. Due to the computational costs of the simulations, we did not iterate on this method, but instead accepted the values we obtained for h_f, which, with the exception of case A10M, are larger than those in the experiments, as seen in Table 5.4.

5.3.2 Comparison of wall-normal profiles

In Figure 5.6 we compare the particle velocity profiles of the simulation to the experimental results of Aussillous et al. [19]. We calculated the particle velocity profile $\langle u_p \rangle$ from our simulations by averaging the velocities of all the particles in the streamwise and

spanwise directions whose center fell within a given range of heights. We used bins of width R_p arranged such that the topmost bin extended from $y = h_p - R_p$ to $y = h_p$. We evaluated the fluid velocity profile by averaging the u-velocity field in the streamwise and spanwise directions for each grid cell of the y-coordinate. For this calculation, we used the particle cell volume fractions ϕ to exclude fluid velocities existing within the particles:

$$\langle u \rangle = \frac{\int_0^{L_z} \int_0^{L_x} (1-\phi) u \, \mathrm{d}x \, \mathrm{d}z}{\int_0^{L_z} \int_0^{L_x} (1-\phi) \, \mathrm{d}x \, \mathrm{d}z} \tag{5.14}$$

The fluid velocity profiles exhibit a parabolic shape in the clear fluid above the bed, as shown in Figure 5.5. At the interface between the clear fluid and particle bed, we observe some slip between the fluid and the particles, but within the bed the two velocity profiles are very similar, with only a slight difference due to flow between the particles. The particle velocity profiles from the simulations compare very well with the experiments for cases A9 and A10, and reasonably well for cases A1 and A2.

Part of the discrepancy between our experiments and the simulations is due to the differences in bed heights and Shields numbers as seen in Table 5.4. In this table, we can see that cases A1 and A2 exhibit the largest differences in the fluid height between the simulations and experiments, which may have resulted in the larger deviations in the velocity profiles seen in Figure 5.6. Likewise, for these two cases we can also see larger differences in the Shields number, which can be sensitive to the fluid height h_f.

5.3.3 Comparison of bulk quantities

We ran the simulation until it reached a constant particle velocity flux q_v, defined as

$$q_v = \int_0^{L_y} \langle u_p \rangle \, \mathrm{d}y, \tag{5.15}$$

Case	Experimental value			Simulation value
	$\overline{q_v}^-/q_f$	$\overline{q_v}/q_f$	$\overline{q_v}^+/q_f$	$\overline{q_v}/q_f$
A1	5.e-3	1.2e-2	1.9e-2	6.71e-3
A2	5.e-3	1.1e-2	1.6e-2	5.17e-3
A9	4.87e-3	8.20e-3	1.15e-2	7.61e-3
A10	5.17e-3	7.04e-3	8.91e-3	5.84e-3
A10M	5.17e-3	7.04e-3	8.91e-3	7.56e-3

Table 5.5: Comparison of the velocity flux $\overline{q_v}$ between our simulations and the experiments of Aussillous et al. [19]. $\overline{q_v}^+/q_f$ and $\overline{q_v}^-/q_f$ represent the mean q_v/q_f plus and minus the standard deviation over the averaging time, respectively.

where $\langle u_p \rangle$ is the binned particle velocity profile as defined in the previous section. Unlike q_f, which had no variability in time, q_v did vary as particles occasionally locked in place or rolled over one another. We therefore evaluated a time-averaged value of the particle velocity flux

$$\overline{q_v} = \frac{1}{T_{avg}} \int_{t_s}^{t_f} q_v \, \mathrm{d}t, \tag{5.16}$$

where t_f is the time at the end of the simulation, t_s is the time at which the particle flux reached steady-state, and $T_{avg} = t_f - t_s$ is the time interval over which the data was averaged. The values of T_{avg} are given in Table 5.4.

In Table 5.5, we can see a good agreement between our numerical results and the experimental values of the velocity flux q_v. Because these quantities are derived from the particle velocity profiles, we expect to see the similar trends, namely that we underestimate the mean values from the experiments and obtain better matches for cases A9 and A10. However, our results still fall within the margin of error of the experiments.

5.3.4 Polydisperse flow

Furthermore, we conducted another simulation to show the effect of polydispersity. In experiments, it is impossible to have a perfectly monodisperse set of particles. In their article, Aussillous et al. [19] reported having a set of spheres with diameters following

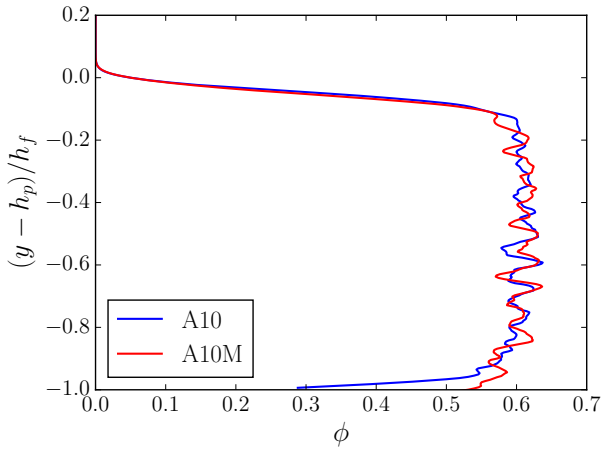

Figure 5.7: Wall-normal profiles of average particle volume fractions.

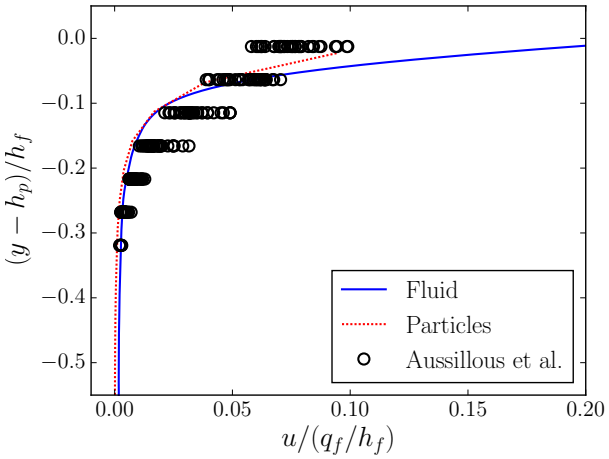

Figure 5.8: Wall-normal profiles of average fluid and particle velocities for the simulation with polydisperse particles (case A10M).

a Gaussian distribution of mean $D_p = 1.1$mm and standard deviation $\sigma(D_p) = 0.1$mm, which is almost 10% of the mean. We created a simulation containing this distribution of particle diameters and a similar submergence depth to that of case A10. The parameters used are listed under case A10M in Table 5.4.

In Figure 5.7, we do not see any appreciable changes in the particle bed volume fractions between cases A10 and A10M. The average volume fraction within the bed is $\phi = 0.609$, which is consistent with a random sphere packing fraction. On the other

hand, in Figure 5.8, we see a slightly increased velocity profile compared to that of case A10 (Figure 5.6d). This is likely due to the decreased value of h_f compared to that of A10, which results in a higher Shields number, as shown in Table 5.4. Therefore, we also obtain a velocity flux that overpredicts the mean experimental value, as shown in Table 5.5. However, the particle velocity profile and velocity flux still agree very well with the experimental results, and the results suggest that using monodisperse spheres is a valid approximation to polydisperse spheres for this experimental setup.

5.4 Conclusions

We performed a convergence study on the pressure-driven flow over an erodible sediment bed. We only analyzed the beginning of the flow because the system quickly turned chaotic and would require a large amount of computational resources to reach a statistically-converged state. In this startup region, the results converge at higher grid resolutions. Using the highest resolution as a reference solution, we found that the simulations exhibit third-order accuracy, which is not fully understood, but could result from our disabling Lagrangian markers for nearby particles. We also observed that strong unphysical porous flows can develop within the sediment bed at lower grid resolutions. In order to avoid these porous flows and have minimal errors in the sediment flux, a grid resolution of at least $D_p/h = 20$ is recommended, though $D_p/h = 25$ would be better.

We also validated the ability for PARTIES to accurately handle simulations involving many particles using the experiments of Aussillous et al. [19]. Indeed, as designed, the strategies taken with the collision modeling in the previous chapter resulted in a numerically-stable particle bed that could be eroded by a fluid flow while particles remained in sustained contact. Furthermore, we obtained good quantitative agreement with Aussillous et al. for the particle bed velocities under different flow conditions. In

addition, we presented a first test case involving polydisperse sediment. The high degree of accuracy achieved will now enable us to analyze phase-resolved numerical simulation data in great detail.

Chapter 6

Coarse-graining

6.1 Introduction

In order to develop or use a continuum model for a fluid/particle mixture, such as that of Ouriemi et al.[16], we need to be able to describe the particle phase in a continuum sense. One method is binning, or averaging these values within control volumes based on the location of the particle center, which we used in Section 5.3. While simple to implement, it requires a large sample size of particles, either using large bins, which reduces the spatial resolution, or large time averages, which only works well for steady-state configurations and can be computationally-expensive to obtain. It can also be especially sensitive when particles are sparse, such as near the top of a particle bed.

Zhu and Yu [100] developed an alternative coarse-graining method for granular flows, which transforms a discrete microscopic field (a set of particles) into a macroscopic continuum field (a particle continuum). This transformation is carried out in such a way as to satisfy a set of equations of motion (mass and momentum) for the continuum field. While Zhu and Yu envisioned coarse-graining over a large number of particles, Goldhirsch [101] developed a similar methodology to represent the particles in a continuum sense that

could even be on the scale of the particle size. Weinhart et al. [102] implemented Goldhirsch's approach and extended it to include the effects of walls. They demonstrated how the particle continuum field can be represented by a numerical mesh with a resolution finer than the particle size (10 grid cells per particle diameter or more) to show the spatially-smooth variations in e.g. linear momentum. Weinhart et al. [103] later showed how, for 3-D granular flows, this coarse-graining method can produce a complete stress tensor for the particle phase. They also investigated the effect of different averaging volumes, ranging from several particle diameters to a fraction of a particle diameter. Nott et al. [104] developed a continuum framework for the particle phase that could incorporate a coarse-graining function, but they did not implement it for any particular systems.

In this chapter, we discuss our implementation of the coarse-graining method, which is based largely on the work of Weinhart et al. [102]. The novelty in our work is the application of the method to particle-laden flows, whereas previous applications have been for granular flows in which no fluid is present [102, 103, 105]. We also use a different coarse-graining function, which will be described below, but this fact does not change the underlying mechanics of the method. After describing our implementation of the coarse-graining method, we will briefly show some results from an erodible bed simulation to illustrate its capability. This method will then provide a useful tool for our analysis in subsequent chapters.

6.2 Coarse-graining method

Goldhirsch [101] and Weinhart et al. [102] developed their coarse-graining methods to exactly satisfy the equations of motion for the particle phase, including continuity and momentum. However, it is not straightforward to extend these continuum equations of motion to include the effects of hydrodynamic forces acting on the particle centers, which

is information we would ideally like to use due to its low storage cost in simulations. Instead, we use their ideas to obtain continuum fields for particular quantities. For instance, we can obtain the particle volume fraction by

$$\phi^{cg}(\mathbf{x}, t) = \sum_{p=1}^{N_p} V_p \mathcal{W}(\mathbf{x} - \mathbf{x}_p(t)), \tag{6.1}$$

where N_p is the number of particles, V_p and $\mathbf{x}_p(t)$ are the volume and position of the center of particle p, and $\mathcal{W}$ is the conservative coarse-graining function, described further in Section 6.2.1. We can similarly obtain a coarse-grained particle velocity field,

$$\mathbf{u}^{cg}(\mathbf{x}, t) = \frac{1}{\phi^{cg}(\mathbf{x}, t)} \sum_{p=1}^{N_p} V_p \mathbf{u}_p(t) \mathcal{W}(\mathbf{x} - \mathbf{x}_p(t)), \tag{6.2}$$

where $\mathbf{u}_p(t)$ is the velocity of particle p.

For other quantities acting at the particle center, such as forces, we define the coarse-grained quantity to be

$$\mathbf{F}^{cg}(\mathbf{x}, t) = \sum_{p=1}^{N_p} \mathbf{F}_p(t) \mathcal{W}(\mathbf{x} - \mathbf{x}_p(t)). \tag{6.3}$$

For our analysis in later chapters, we will coarse-grain the forces acting on the particle centers. We could alternatively coarse-grain the collision forces in a manner similar to that of Weinhart et al. [102], which would give us the collision stress tensor

$$\sigma_{ij}^{cg}(\mathbf{x}, t) = \sum_{p=1}^{N_p} \sum_{q=p+1}^{N_p} F_{c,pq,i}(t)\, r_{pq,j}(t) \int_0^1 \mathcal{W}(\mathbf{x} - \mathbf{x}_p(t) + s\mathbf{r}_{pq}(t))\, \mathrm{d}s, \tag{6.4}$$

where $\mathbf{F}_{c,pq}$ is the collision force acting on particle p from particle q, and $\mathbf{r}_{pq} = \mathbf{x}_p - \mathbf{x}_q$ points from the center of particle q to the center of particle p. The integral effectively

spreads the contact force along the line connecting $\mathbf{x}_p$ to $\mathbf{x}_q$. However, we can only use hydrodynamic forces acting at the particle center of mass because, for computational efficiency, PARTIES does not store information across the particle surface. Hence, for consistency we will later limit our analysis to all quantities acting at the particle centers.

6.2.1 Coarse-graining function

The coarse graining function $\mathcal{W}$ plays a very similar role to that of the delta functions used in the IBM: smoothly spreading a quantity from one mesh to another. The main properties identified by Weinhart et al. [103] are that $\int_{\mathbb{R}^3} \mathcal{W}(\mathbf{r})\,\mathrm{d}\mathbf{r} = 1$, which conserves the spread quantity, and that $\mathcal{W}(\mathbf{r})$ has two continuous derivatives, which allows one to evaluate gradients of the resulting coarse-grained fields analytically. While Weinhart et al. [102] used a Gaussian coarse-graining function and Weinhart et al. [103] used a polynomial coarse-graining function, we instead implement one based on the delta function of Roma et al. [57]:

$$\mathcal{W}(\mathbf{r}) = \frac{1}{w^3}\delta(r_x/w)\,\delta(r_y/w)\,\delta(r_z/w), \tag{6.5}$$

where w sets the coarse-graining width and

$$\delta(r) = \begin{cases} \frac{1}{3}\left(1 + \sqrt{-3r^2+1}\right) & |r| \leq 0.5 \\ \frac{1}{6}\left[5 - 3|r| - \sqrt{-3(1-|r|)^2+1}\right] & 0.5 < |r| \leq 1.5 \\ 0 & |r| > 1.5. \end{cases} \tag{6.6}$$

Thus, $\mathcal{W}(\mathbf{r})$ has a radius of influence of $1.5w$ and one continuous derivative. We chose this function because it exhibits good conservation properties and because we do not evaluate the coarse-graining expressions analytically and hence do not need multiple

continuous derivatives. In order to implement the coarse-graining method, we must create an Eulerian mesh on which to spread the Lagrangian (particle-centered) quantities. We could set the coarse-grained mesh width, h^{cg}, to match that of the fluid grid, i.e. $h^{cg} = h$, or we could set it to a coarser value, i.e. $h^{cg} > h$, to reduce the computational cost of the coarse-graining evaluation. The function we selected allows us to perfectly conserve quantities when using coarser values of h^{cg}. More precisely, this coarse-graining function conserves quantities as long as w is an integer multiple of the coarse-graining mesh size, h^{cg}, i.e. $w = nh^{cg}$ for $n \in \mathbb{Z}$. We have used $w = h^{cg}$ to $w = 3h^{cg}$ in our analysis, whereas the Gaussian or polynomial functions, on the other hand, would require smaller values for h^{cg}, such as $w = 10h^{cg}$, in order to get closer to conserving the spread quantities.

The coarse-graining width, w, determines the distance over which the particle-centered quantities are spread. Weinhart et al. [103] studied the sensitivity of results to w, finding that they did not change appreciably under two regimes: the sub-particle scale $w \approx 0.05D_p$ and the particle scale $w \approx D_p$. We will discuss our own findings regarding the width further below.

6.2.2 Handling boundaries

When particles approach boundaries, some of their coarse-grained data can be lost due to the coarse graining function (6.5) spreading information beyond the wall. For example, consider the coarse-grained representation of the volume fraction for particle p, which is sitting on the wall and has a coarse-grained width $1.5w > R_p$, as shown in Figure 6.1. The red dashed line shows the area over which the mass, and hence volume fraction, will be spread. Because a portion of the mass is spread below the wall, it will not be accounted for when taking spatial averages within the domain, and the overall volume fraction will be underrepresented near the wall. We can account for this lost mass using

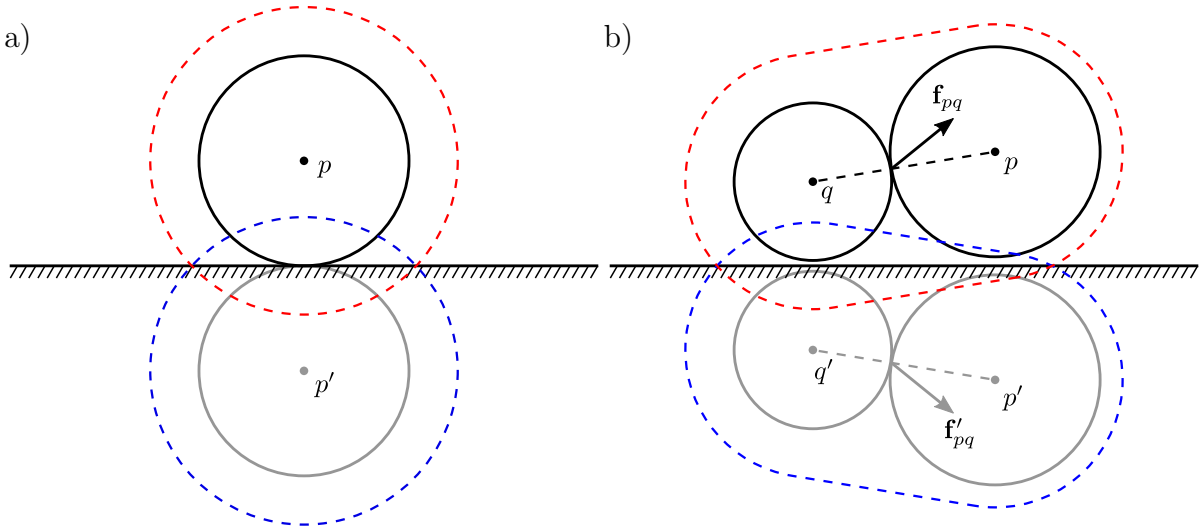

Figure 6.1: Reflection of coarse-grained quantities near a wall, whose radii of influence are represented by dashed lines. Shown are (a) particle-based quantities, such as volume fraction and velocity, and (b) collision-based quantities, which are spread along lines of contact between particle centers.

the method of Zhu and Yu [100] and Sun and Xiao [106], who extended it to consider corners of boundaries, by reflecting this particle across the wall (represented by the gray particle) and including the coarse-grained values from this reflected particle (represented by the blue dashed circle). We employ this method at the particle/fluid interface as well, creating an artificial wall at $y = y_p$, where y_p is the height of the particle bed, only when calculating the coarse-grained particle velocity field $\mathbf{u}^{cg}$.

6.3 Coarse-grained particle bed

6.3.1 Simulation setup

We will now explore how to choose a suitable coarse-graining width, w. Consider a pressure-driven flow over an erodible particle bed similar to the one in Section 5.3. The exact simulation setup is described by run Re8 in Section 7.2.2, but we briefly describe

Ga	0.850
Re_{ref}	8.33
ρ_p/ρ_f	2.1
Timestep	CFL = 0.5
Domain size ($L_x/D_p \times L_y/D_p \times L_z/D_p$)	$20 \times 30 \times 10$
Domain grid size ($L_x/h \times L_y/h \times L_z/h$)	$512 \times 768 \times 256$
Domain boundary conditions	p × ns × p
Initial h_f/D_p	10.0
Particle resolution, D_p/h	25.6

Table 6.1: Simulation parameters for the pressure-driven flow over a bed of particles.

Resolution	w/D_p	w/h	h^{cg}/h
Coarse	0.94	24	8
Medium	0.31	8	4
Fine	0.04	1	1

Table 6.2: Values of the coarse-graining width, w and the coarse-graining grid size, h^{cg}, used to generate a coarse resolution, in which the width is similar to the particle diameter, a medium resolution, in which the width is similar to the particle radius, and a fine resolution, in which the width is much smaller than the particles.

it here. The simulation domain has dimensions $L_x = 20D_p \times L_y = 30D_p \times L_z = 10D_p$ discretized with $D_p/h = 25.6$. The bed was generated similar to before by allowing 4339 particles to settle under gravity, without the influence of the fluid, onto a bed of 200 fixed particles. The resulting bed fills the domain to a height of $h_p \approx 20D_p$ so that a reference length $y_{ref} = 10D_p$ approximates h_f, the clear fluid height above the particle bed. Other parameters are given in Table 6.1.

To obtain a steady-state flow, we mobilized the bed with a large pressure gradient and then decreased the pressure gradient. To nondimensionalize the simulation, we use a reference Poiseuille flow based on the height y_{ref}, which would approximate the flow if the initial bed were to remain motionless. The reference velocity is based on the average fluid velocity of the reference flow, $u_{ref} = -y_{ref}^2 f_{b,x}/(12\mu_f)$, where $f_{b,x}$ is the pressure gradient of the final flow. From this reference velocity, we define the Reynolds number

to be $Re_{ref} = \rho_f u_{ref} y_{ref}/\mu_f$. We also define a reference stress, $\sigma_{ref} = -y_{ref} f_{b,x}/2$, to be the wall stress from the reference case.

We will apply the coarse-graining method at an instantaneous point in time for the simulation, demonstrating its ability to smooth data without averaging in time. We will also study the effect of the coarse-graining width, w, using three different resolutions, which vary from $w = 0.94D_p$ to $w = 0.04D_p$ and are given in Table 6.2.

6.3.2 Particle volume fraction

For this instantaneous flow field, Figure 6.2 shows the coarse-grained particle volume fraction

$$\langle \phi^{cg} \rangle = \int_0^{L_z} \int_0^{L_x} \phi^{cg} \, \mathrm{d}x \mathrm{d}z, \tag{6.7}$$

which is averaged in the streamwise and spanwise directions, for different coarse-graining widths w. Figure 6.2a shows a coarse-graining width that is close to the particle diameter, which means that the radius of influence of the coarse-graining function is actually $1.5D_p$. In this case, the coarse-grained volume fraction is much smoother than the grid-resolved volume fraction, which was obtained by directly calculating the particle volume fraction on the fluid mesh. Oscillations in the grid-resolved volume fraction arise from the particles forming an ordered layering. With perfectly-random packing and a large enough averaging volume, the grid-resolved volume fraction should become smooth. However, this coarse-graining width can provide us with a smooth volume fraction field when the grid-resolved volume fraction cannot. One downside, though, is that this width smears the volume fraction at the interface between the particle bed and the clear fluid above.

Figure 6.2b shows a coarse-graining width similar to that of the particle radius. In this case, the coarse-grained volume fraction is very similar to the grid-resolved volume fraction. This width therefore does an excellent job capturing the fluid/bed interface,

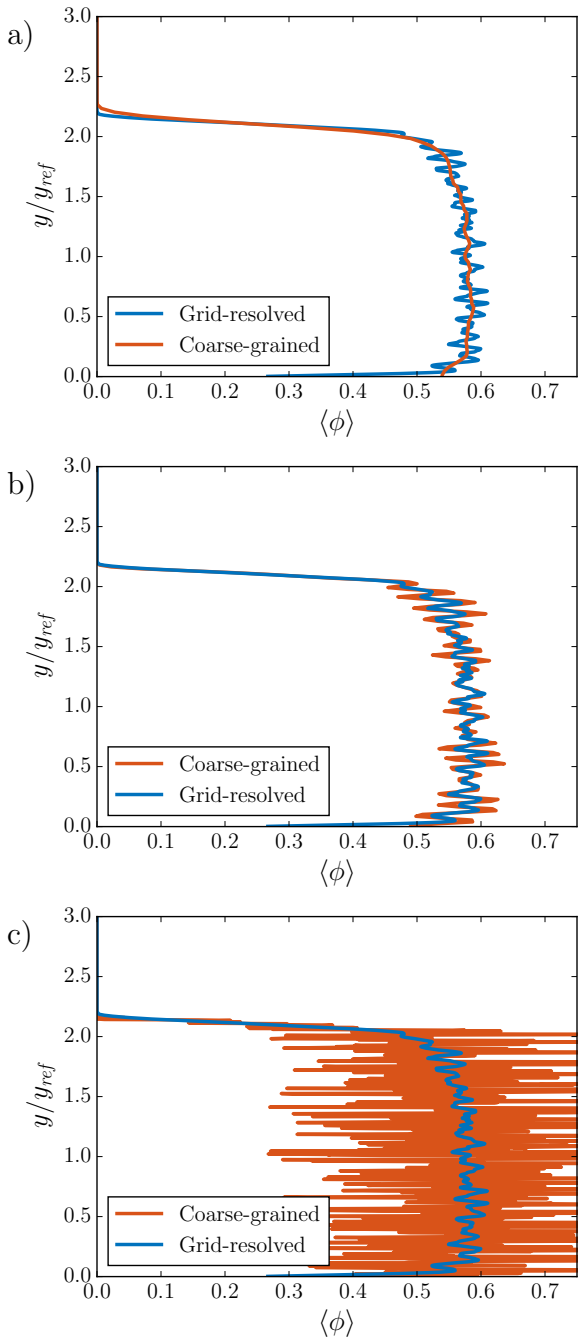

Figure 6.2: Coarse-grained particle volume fraction for (a) $w = 0.94D_p$, (b) $w = 0.31D_p$, and (c) $w = 0.04D_p$ compared with the volume fraction resolved using the fluid grid $D_p/h = 25.6$.

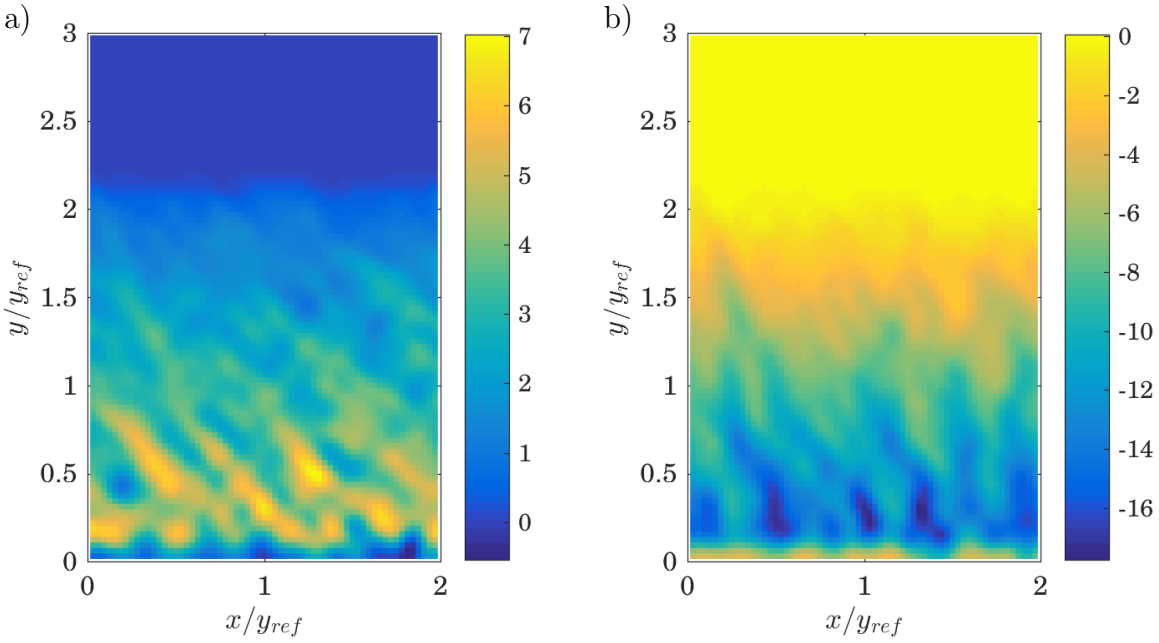

Figure 6.3: Coarse-grained particle collision stresses according to (6.4) for $w = 0.94D_p$. (a) shows the shear stress $\sigma_{12}^{cg}/\sigma_{ref}$ while (b) shows the wall-normal stress $\sigma_{22}^{cg}/\sigma_{ref}$.

but it is less useful if we desire a smooth coarse-grained field.

Figure 6.2c shows the results using a coarse-graining width much smaller than the particle diameter. This coarse-grained volume fraction exhibits enormous oscillations, rendering it useless for most applications. Although this width, in addition to the coarsest width, was recommended by Weinhart et al. [103], it does not appear to be very useful for this situation without significant time-averaging.

6.3.3 Collision stress

An important feature of the coarse-graining method, especially compared to binning, is its 3-D spatial resolution. The coarse-grained volume fraction, for instance, does not need to be averaged in the streamwise and spanwise directions, but could be averaged in just the spanwise direction, or taken as a 3-D field. In Figures 6.3–6.5, we present 2-D coarse-grained stress fields, obtained by averaging (6.4) in the spanwise direction alone.

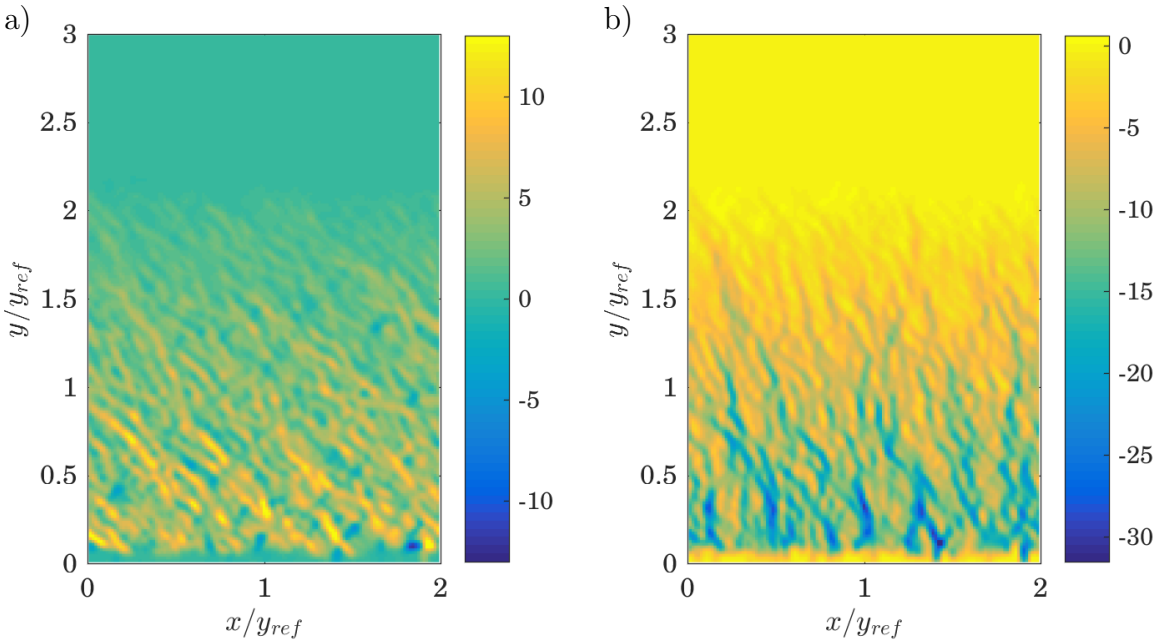

Figure 6.4: Coarse-grained particle collision stresses according to (6.4) for $w = 0.31D_p$. (a) shows the shear stress $\sigma_{12}^{cg}/\sigma_{ref}$ while (b) shows the wall-normal stress $\sigma_{22}^{cg}/\sigma_{ref}$.

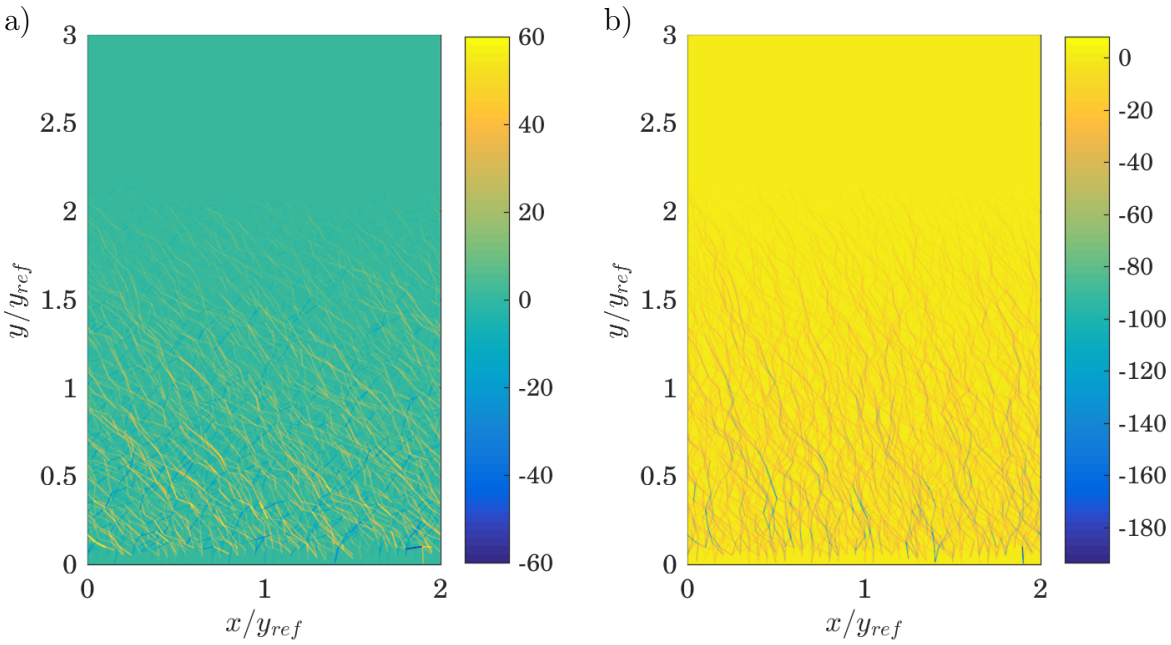

Figure 6.5: Coarse-grained particle collision stresses according to (6.4) for $w = 0.04D_p$. (a) shows the shear stress $\sigma_{12}^{cg}/\sigma_{ref}$ while (b) shows the wall-normal stress $\sigma_{22}^{cg}/\sigma_{ref}$.

Figure 6.3a shows the shear stresses at the coarse resolution. The stresses appear to form diagonal lines, which is consistent with expectations for a sheared particle bed [107]. In contrast, the stress chains for the vertical stress, shown in Figure 6.3b, form more vertical patterns. These stress chains become more apparent in Figure 6.4, which uses a coarse-graining width close to the particle radius. There are also negative shear stresses in this figure, resulting from tensional lubrication forces. These tensional stresses are not apparent at the coarsest resolution due to the smoothing. Finally, at the finest resolution, the force chains are even more resolved. Thus, very small coarse-graining widths can still be useful when considering collisional stresses.

However, notice that the magnitude of the stresses depends strongly on the coarse-graining width. The finer-resolution widths result in much larger stresses because they concentrate the stress into smaller volumes; averaging the stresses over large volumes at different resolutions will result in the same stresses. As an illustration, compare the coarse volume fractions in Figure 6.2a to the fine volume fraction in Figure 6.2c. While the fine resolution exhibits much larger and smaller volume fractions at a given height compared to the coarse resolution, both resolutions would average out to similar values over larger volumes.

6.4 Representing the volume fraction

There are two ways that we can obtain volume fraction data: resolve it directly, such as on the fluid grid, or use the coarse-graining method, i.e. (6.1). Resolving the volume fraction directly captures the sharp interface between the particle bed and clear fluid layer above, but it can also contain oscillations within the particle bed due to organization of the particle layers, as shown in Figure 6.6a. The coarse-graining method, on the other hand, perfectly smooths out the volume fraction within the particle bed, but smears out

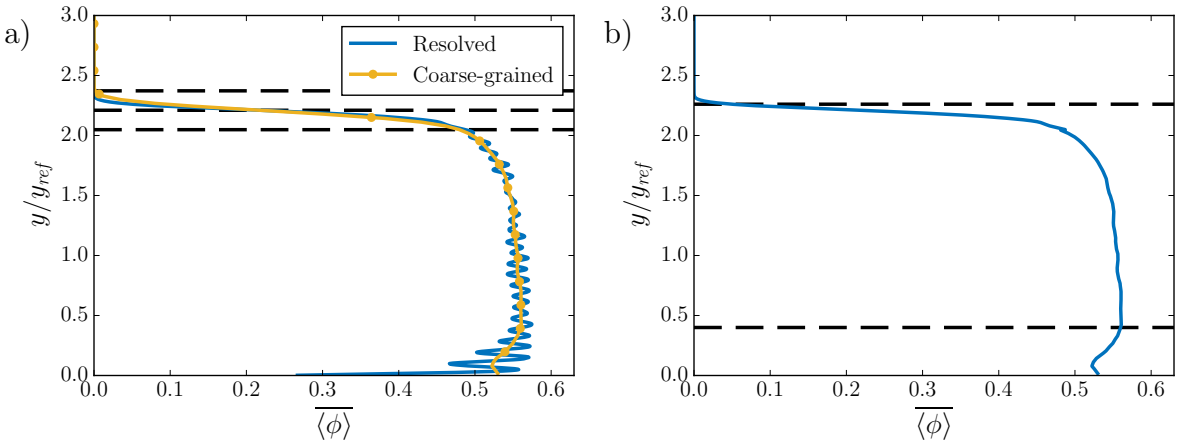

Figure 6.6: Volume fraction from case Re17 (a) measured directly using the fluid grid and the coarse-graining method and (b) measured using the hybrid resolved/coarse-grained method. Dashed lines indicate the y-coordinates used to (a) create the hybrid volume fraction and (b) filter data for the rheology plots.

the volume fraction data at the bed/fluid interface, as shown in the same figure. We could, however, use a hybrid technique that uses the resolved volume fraction at the interface and the coarse-grained data within the bed.

To find the location at which we separate the two methods, notice that the coarse-grained volume fraction crosses over the resolved volume fraction about halfway through the bed/fluid interface. We therefore determine the point at which the coarse-grained volume fraction goes to zero, indicated by the top dashed line in Figure 6.6a, and the point at which the two volume fractions cross at the interface, indicated by the middle dashed line in the same figure. The bottom dashed line, indicating the separation between the two methods, is then placed such that the middle dashed line is exactly halfway between the top and bottom lines. For our simulation results, this method produces pretty reasonable, smooth curves, as shown by the resulting hybrid line in Figure 6.6b. A blending algorithm could be used to smooth the transition from one method to the other, but without blending this method produces smooth enough results for visualizing the dependence of the rheological measurements on the volume fraction in Section 8.3.

Finally, for the purposes of analyzing the bed rheology in Chapter 8, we apply filtering to exclude data from the extremes of the domain. At the bed/fluid interface, we exclude data for volume fractions $\overline{\langle\phi\rangle} < 0.05$ to avoid division by small numbers in evaluating some of the rheological quantities. At the lower wall, we exclude data for $y < 4D_p$, which we selected by visual inspection of the volume fraction data to avoid the effects of the lower wall. Notice in Figure 6.6a how volume fraction decreases and the oscillations grow near the lower wall. The two criteria used to filter the rheological data are illustrated by the dashed lines in Figure 6.6b.

6.5 Conclusions

We presented our implementation of the coarse-graining method, which allows us to represent particle quantities in an instantaneous 3-D continuum field. We found that using a coarse-graining width, w, comparable to the particle diameter results in a smoothed continuum field that also conserves quantities of interest. Thus, while the binning method might be sensitive to particles jumping from one bin to the next, there is no such sensitivity in the coarse-graining framework. In fact, this method can represent smooth fields even for instantaneous data. The coarse-graining method can also provide a stress tensor for collision stresses capable of visualizing force chains. However, other methods may be more computationally efficient and quantitatively informative for analyzing force chains. We have also decided to avoid the tensorial description of collision stresses for later analysis, using instead forces acting at particle centers. While the coarse-graining method may smear information at the fluid/particle interface, it will be useful for measuring forces, velocities, and volume fractions of the particle phase.

Chapter 7

Momentum balance

7.1 Introduction

To test, validate, and enhance constitutive models for sediment transport, highly resolved data is needed with a degree of detail that can hardly be achieved by experiments. A starting point of a rigorous analysis should be the full description of the momentum balance and the resulting stress budget of the fluid-particle mixture. This, however, has proved to be challenging task due to the nontrivial coupling of the continuous fluid phase, on the one hand, and the disperse particle-phase on the other [16]. Nevertheless, this analysis will be crucial to measure the effective granular stress to characterize the rheology of the sediment bed. Recently, various numerical studies of particle-resolving Direct Numerical Simulations using the Immersed Boundary Method to couple the two phases have been carried out to measure stresses within particle-laden flows in various ways. Unfortunately, these studies were not specifically designed to decompose the stress budget into its different components, nor have they been used to form or compare against constitutive models. For example, Kidanemariam et al. [76] included a stress balance for turbulent particle-resolved flows to justify a statistical steady-state by evaluating

the average velocity profiles. Picano et al. [69] included a momentum balance for the shear stress for a turbulent flow laden with neutrally-buoyant particles. They used the stress balance developed by Zhang and Prosperetti [108], which is based on averaging volumes containing many particles. Due to the neutrally-buoyant particles, however, a sediment layer did not form. Vowinckel et al. [109, 110] developed momentum balances for double-averaged turbulent flows over granular beds, which also require averaging volumes containing many particles. Unfortunately, these latter two studies did not analyze the interfacial stresses coupling the fluid stress to the granular stress.

This chapter addresses this issue in detail. We develop a momentum balance for laminar flows, whose terms can be computed in a straightforward manner. This should be true for the most simple scenario, which is a single particle in a shear flow, and the much more complex situation of a thick sediment bed constituted of thousands of particles that is fully or partially in motion. The newly-developed framework will allow us to look carefully at the components that contribute to the stress balance of the fluid and the particle. We apply our analysis to the data generated by grain-resolving DNS using the IBM. After validating the concept for the simple single-grain case, we compute the stress budget for a computational scenario that is very similar to the experimental setup of Aussillous et al. [19] and the simulations performed in Chapter 5.

The chapter is structured as follows. First, we describe the computational setups in Section 7.2. Subsequently, we present the derivation of the stress budgets for the fluid and the particle phase in Section 7.3. Finally, results are presented for the single-particle case as well as for the sediment bed with complex rheology in Section 7.4.

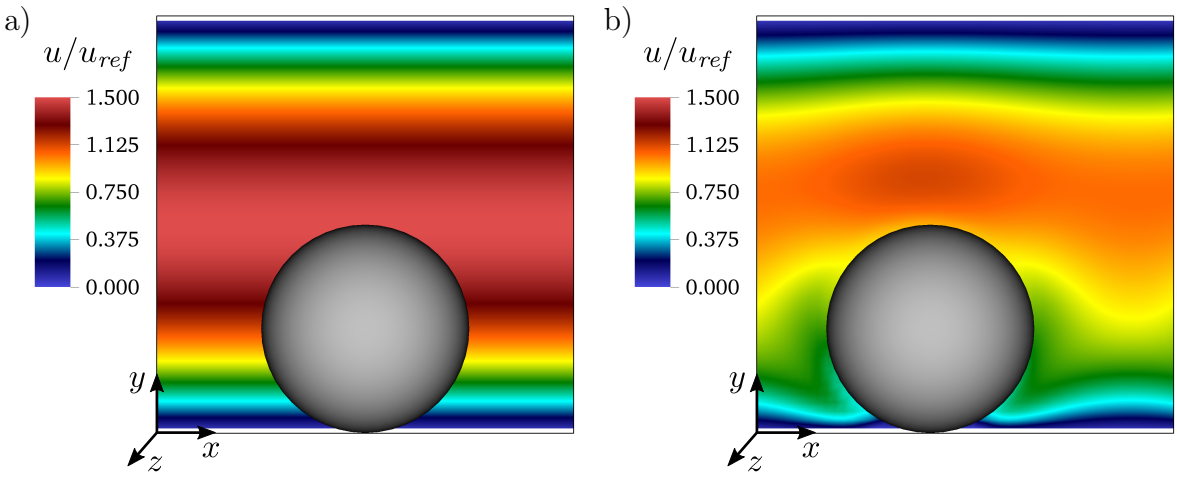

Figure 7.1: Fluid flow field along the particle center line ($z/L_z = 0.5$) at (a) $t/t_{ref} = 0$ and (b) $t/t_{ref} = 4$ for the simulation of a single rolling particle. Pseudocolor indicates fluid velocity in the x-direction.

7.2 Simulation setup

We will apply our stress balance framework to two different configurations. The first will involve the flow around a single sphere, where we can obtain a true steady-state flow. This simple case will thus test the framework under ideal conditions and illustrate its ability to resolve stresses on the particle scale. The second will be a more realistic case involving a flow over a bed of thousands of particles. This complex case will illustrate the type of information this framework can provide for general particle-laden flows and how it can be useful for future studies.

7.2.1 Single rolling particle

One key feature of our analysis technique is that it should work just as well for a single particle as for a large number of particles. As a simple case, we consider a single sphere rolling along the bottom of a channel with a pressure-driven flow. In the absence of the particle, there would be a laminar flow with a bulk (average) velocity of

Ga	8.29
Re_{ref}	10
ρ_p/ρ_f	2.1
Timestep	CFL = 0.5
Domain size ($L_x/D_p \times L_y/D_p \times L_z/D_p$)	$2.0 \times 2.0 \times 2.0$
Domain grid size ($L_x/h \times L_y/h \times L_z/h$)	$48 \times 48 \times 48$
Domain boundary conditions	p × ns × p
Particle resolution, D_p/h	24.0
Coarse-graining grid size, h^{cg}/h	1
Coarse-graining width, w/h	16

Table 7.1: Simulation parameters for a single rolling particle. Boundary conditions are periodic (p) and no-slip (ns). Coarse-graining parameters are defined in Section 6.2.

$u_{ref} = -L_y^2/(12\mu_f)f_{b,x}$ and a Reynolds number of $Re_{ref} = \rho_f u_{ref} L_y/\mu_f = 10$, where L_y is the channel height. The presence of the particle, however, changes the bulk velocity and Reynolds number. The domain size is two particle diameters in each of the x-, y-, and z-directions, discretized with 24 grid cells per particle diameter, so that the particle has a significant influence on the flow field. We provide the other parameters associated with this simulation in Table 7.1, where we define the Galileo number to be $Ga = \rho_f\sqrt{(\rho_p/\rho_f - 1)gD_p^3}/\mu_f$. Parameters not listed in Table 7.1 are the same as those in Chapter 4.

We initialized the flow velocity with the reference Poiseuille parabolic profile, shown in Figure 7.1a. The particle started with a translational and rotational velocity obtained from averaging the initial flow field within its volume. At this low Reynolds number, the flow remains laminar, but takes time to develop because the presence of the particle constricts and slows the flow. We ran the simulation until time $t = 4t_{ref}$, where $t_{ref} = L_y/u_{ref}$, at which point the particle, rolling along the lower wall, had slowed to a constant velocity in the streamwise direction, shown in Figure 7.1b. We therefore consider the flow to be in a steady state from the reference frame of the particle.

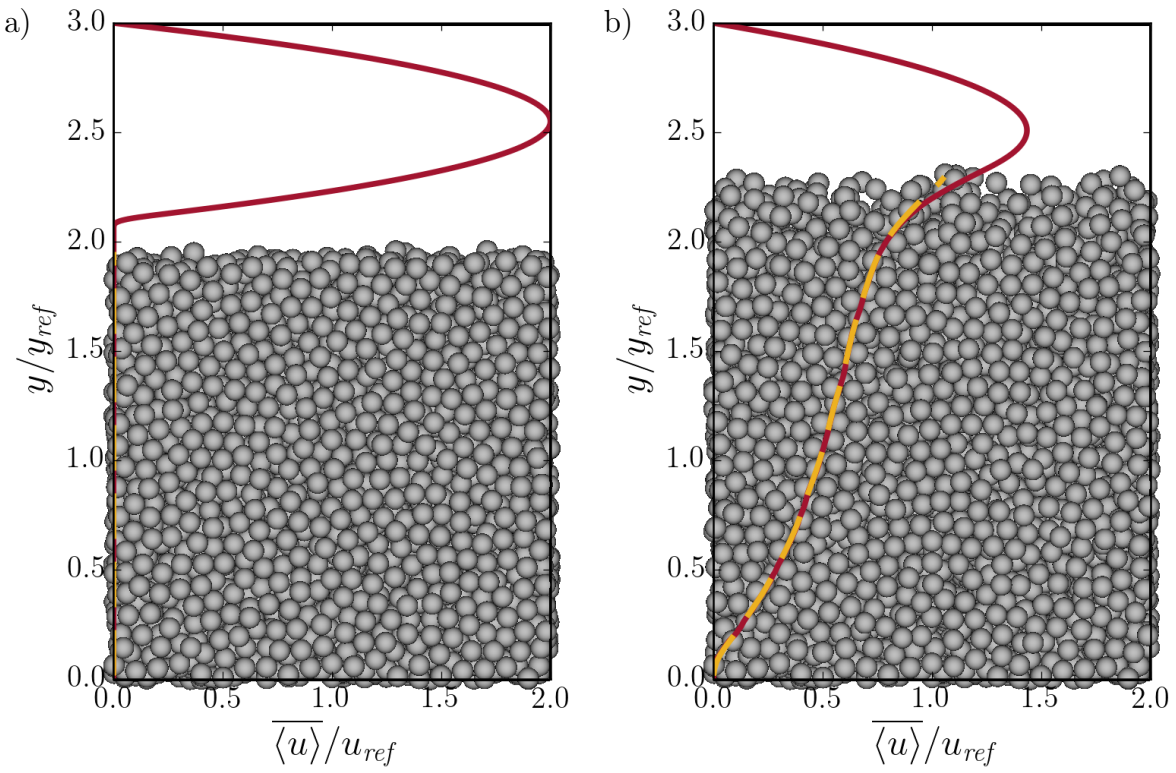

Figure 7.2: Bed configuration at (a) $t/t_{base} = 0$ and (b) $t/t_{base} = 10$ for simulation Re67 listed in Table 7.3. Lines indicate the average streamwise (x-direction) fluid velocity (red) and particle velocity (yellow).

7.2.2 Sheared bed of particles

We are ultimately interested in understanding flows involving many (thousands or more) particles. We therefore consider a setup very similar to the one in Section 5.3, which involves a pressure-driven flow over a bed of particles. The domain has dimensions $20D_p \times 30D_p \times 10D_p$ and is discretized with 25.6 grid cells per particle diameter. We formed the bed by allowing 4339 particles to settle under gravity, without the influence of the surrounding fluid, onto a layer of 200 fixed particles whose centers randomly vary in height above the bottom wall by D_p, providing an irregular roughness [27]. The resulting bed fills the domain to about a height of $h_p \approx 20D_p$ from the bottom wall, where h_p is the particle bed height, leaving a gap of about $10D_p$ between the top wall and the top

Ga	0.850
ρ_p/ρ_f	2.1
Timestep	CFL = 0.5
Domain size ($L_x/D_p \times L_y/D_p \times L_z/D_p$)	$20 \times 30 \times 10$
Domain grid size ($L_x/h \times L_y/h \times L_z/h$)	$512 \times 768 \times 256$
Domain boundary conditions	p × ns × p
Initial h_f/D_p	10.0
Particle resolution, D_p/h	25.6
Coarse-graining grid size, h^{cg}/h	8
Coarse-graining width, w/h	24

Table 7.2: Simulation parameters for the pressure-driven flow over a bed of particles.

Simulation run	Re_{ref}	t_{sim}/t_{base}	t_{avg}/t_{base}
Re67	66.7	$[0, 10.0]$	–
Re17	16.7	$[10.0, 47.2]$	$[16.0, 47.2]$
Re33	33.3	$[10.0, 58.8]$	$[44.0, 52.15]$
Re8	8.33	$[47.2, 92.05]$	$[77.0, 92.05]$

Table 7.3: Simulation parameters for different runs of the pressure-driven flow over a bed of particles. The Reynolds number is based on the reference case, $Re_{ref} = \rho_f u_{ref} y_{ref}/\mu_f$. The simulation was run for the duration t_{sim}. The momentum balance was conducted using time-averaged data over the range t_{avg}.

of the particle bed, as shown in Figure 7.2a.

We will again use a predefined Poiseuille flow as a reference case for the simulation. We define the reference length, $y_{ref} = 10D_p = L_y/3$, to be one-third of the domain height, or the intended clear-fluid height above the particle bed. That is, if the particle bed were to remain motionless, the reference case would represent the fluid flow fairly accurately. The reference velocity, $u_{ref} = -y_{ref}^2 f_{b,x}/(12\mu_f)$, represents the average fluid velocity of the reference case. Finally, we define the reference stress, $\sigma_{ref} = -y_{ref} f_{b,x}/2$, to be the wall stress for the reference case.

We are interested in studying the bed at different states, from those in which only a few particle layers are moving to those where the entire bed is mobilized. We therefore ran this simulation using different flow rates controlled by the volume force $\mathbf{f}_b$. However, it can take a long time for these flows to reach steady-state when initialized from a stationary bed. Therefore, we implemented the following procedure, which is similar to the one used in Section 5.3. To initialize the flow, we applied a large pressure gradient that mobilized the entire bed, as described by run Re67 in Table 7.3. By the end of this simulation run, the bed dilated to a height of $h_p/y_{ref} \approx 2.3$, and the particles just above the fixed layer at the bottom of the domain were moving, as shown in Figure 7.2b. After this initialization phase, the pressure gradient was reduced to produce the simulation runs Re17 and Re33. We carried out run Re8 by continuing Re17 with a lower pressure gradient. As described in more detail in Section 7.4.2, this procedure allowed us to quickly reach steady-state for runs Re8 and Re17, but not for run Re33.

In contrast to the single rolling sphere case, the steady-state configuration for the moving bed is steady only in a time-averaged sense because particle collisions and positions continuously fluctuate. We therefore define the time average of a quantity θ to be

$$\overline{\theta} = \frac{1}{t_{avg,2} - t_{avg,1}} \int_{t_{avg,1}}^{t_{avg,2}} \theta \, \mathrm{d}t, \tag{7.1}$$

where we present the values for $t_{avg,1}$ and $t_{avg,2}$ in Table 7.3. These time-averaging windows were chosen to capture the steady-state results when possible. For the unsteady simulations, the windows were chosen to capture as large a time span as possible for as similar a particle flux as possible. In order to compare the temporal evolution of the simulations directly to each other in Section 7.4.2, we use a set of variables to nondimensionalize the velocity, $u_{base} = u_{ref}(\mathrm{Re67})$, and stress, $\sigma_{base} = \sigma_{ref}(\mathrm{Re67})$, which are based on the reference variables corresponding to run Re67. From these variables, we also define a base time, $t_{base} = y_{ref}/(1.5u_{base})$, which does not vary between the simulations.

7.3 Theoretical stress balance

7.3.1 Fluid phase balance

In conducting a momentum balance of the fluid/particle system, we will look separately at the fluid and particle phases. Later, we will try to combine these two methods to obtain a momentum balance for the fluid/particle mixture, which implicitly accounts for the interactions of the particles on the fluid and the fluid on the particles. We first investigate the fluid phase alone, excluding the volume occupied by the particles and the inter-particle forces. We do account for the effect of the particles, however, through the stress the particles impart on the fluid at their boundaries. We conduct our stress analysis in an integral sense using a control volume Ω_{CV}^{+} that extends from the top wall to an arbitrary height y in the vertical dimension, encompasses the entire domain in the streamwise (x) and spanwise (z) directions, and excludes the volume within particles. Figure 7.3a illustrates the control volume for the case of a single particle, whereas Fig-

ure 7.4 illustrates the control volume for the general case involving many particles. We can write the integral form of (2.1) over this control volume as

$$\int\limits_{\Omega_{CV}^+} \rho_f \frac{\partial \mathbf{u}}{\partial t}\,\mathrm{d}V + \int\limits_{\Omega_{CV}^+} \rho_f \nabla\cdot(\mathbf{uu})\,\mathrm{d}V = \int\limits_{\Omega_{CV}^+} \nabla\cdot\boldsymbol{\tau}\,\mathrm{d}V + \int\limits_{\Omega_{CV}^+} \mathbf{f}_b\,\mathrm{d}V. \tag{7.2}$$

We did not include the IBM force term from (2.1) because the fluid stress at the fluid/particle interface accounts for the effects of the particles. We do, however, include the forcing term $\mathbf{f}_b$, which represents the background pressure gradient used to drive the flow. Application of the divergence theorem then gives us

$$\int\limits_{\Omega_{CV}^+} \rho_f \frac{\partial \mathbf{u}}{\partial t}\,\mathrm{d}V + \int\limits_{\Gamma_{CV}^+} \rho_f (\mathbf{uu})\cdot\mathbf{n}^+\,\mathrm{d}A = \int\limits_{\Gamma_{CV}^+} \boldsymbol{\tau}^+\cdot\mathbf{n}^+\,\mathrm{d}A + \int\limits_{\Omega_{CV}^+} \mathbf{f}_b\,\mathrm{d}V, \tag{7.3}$$

where $\mathbf{n}^+$ is the normal vector pointing outwards from Ω_{CV}^+, and $\boldsymbol{\tau}^+$ is the stress tensor of the fluid outside the particle. These volumes should be thought of as time-dependent ones, i.e. $\Omega_{CV}^+ = \Omega_{CV}^+(t)$ and $\Gamma_{CV}^+ = \Gamma_{CV}^+(t)$. We are thus observing the fluid volume in a Lagrangian sense as it moves around the particle volumes. We can consider a steady-state to be one in which the fluid does not accelerate relative to the particle surface and in which the fluid stresses at the particle surface are constant. In such a case, the time-dependent term evaluates to zero, allowing us to balance the stresses by looking at the advective terms and stresses at the boundaries, which are composed of the surfaces $\Gamma_{CV}^+ = \Gamma_w \cup \Gamma_s \cup \Gamma_y^+ \cup \Gamma_{CV}^p$, as shown in Figure 7.3a. Note that surface Γ_s encompasses the periodic boundaries in both the x- and z-directions For the situation involving many particles in motion, the fluid volume will continue to evolve, never reaching a true instantaneous steady-state. In this case, we apply double-averaging (in time and space; [111]) to eliminate the time-dependent term. In either case, due to the periodic boundary

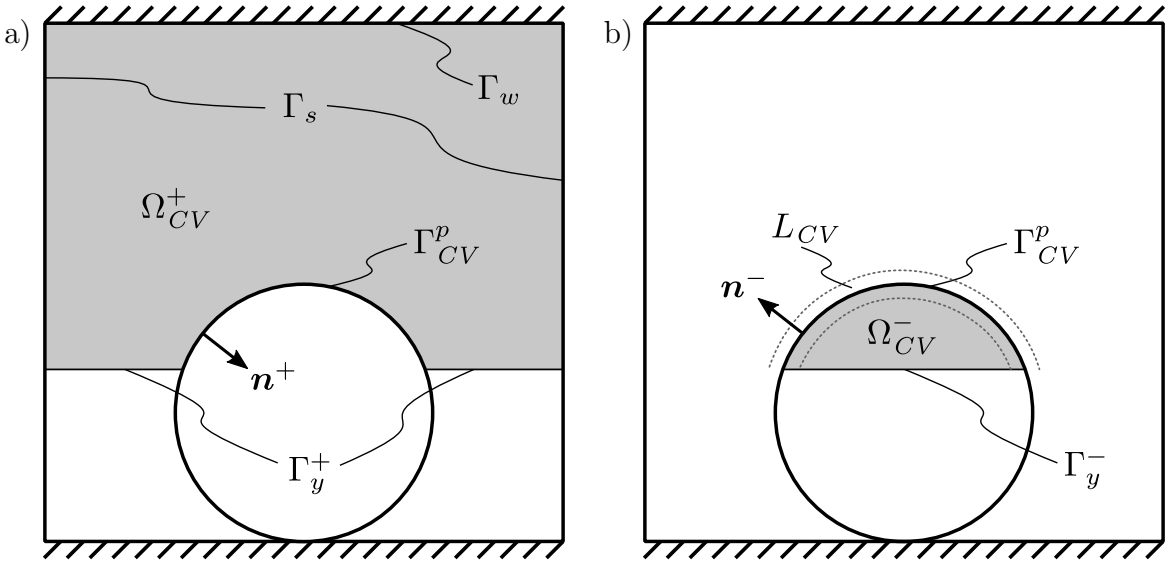

Figure 7.3: Shaded control volumes for fluid (a) surrounding the particle and (b) within the particle.

conditions on the x- and z-boundaries, all the terms along Γ_s cancel out. Furthermore, the upper wall and particle surface impose a no-flux condition, i.e. $(\mathbf{uu}) \cdot \mathbf{n}^+ = 0$ at Γ_w and Γ^p_{CV}. Thus, we can simplify (7.3) to

$$\int_{\Gamma^+_y} \rho_f (\mathbf{uu}) \cdot \mathbf{n}^+ \, \mathrm{d}A = \int_{\Gamma_w \cup \Gamma^+_y \cup \Gamma^p_{CV}} \boldsymbol{\tau}^+ \cdot \mathbf{n}^+ \, \mathrm{d}A + \int_{\Omega^+_{CV}} \mathbf{f}_b \, \mathrm{d}V. \tag{7.4}$$

All of these terms are straightforward to calculate, except for the fluid stress at the particle surface. However, we can evaluate this term indirectly using the IBM force, as was done to obtain the particle equations of motion (2.9) and (2.10). That is, the IBM force acts as a jump in stress between the fluid outside and the fluid inside the particle:

$$\int_{L_{CV}} \mathbf{f}_{IBM} \, \mathrm{d}V = \int_{\Gamma^p_{CV}} \boldsymbol{\tau}^+ \cdot \mathbf{n}^+ \, \mathrm{d}A + \int_{\Gamma^p_{CV}} \boldsymbol{\tau}^- \cdot \mathbf{n}^- \, \mathrm{d}A, \tag{7.5}$$

where we are careful to distinguish between $\mathbf{n}^+$, the outward surface normal for the

volume Ω^+_{CV}, and $\mathbf{n}^-$, the outward surface normal for the volume Ω^-_{CV}, which point in opposite directions. In reality, the particles are rigid objects, but in our simulations, the particles have fluid inside them as a by-product of the IBM. Initially, we only considered the fluid outside the particles, but, in order to determine the forces the particle imparts on the fluid, our analysis now requires us to account for the fluid inside the particles due to the mechanics of the IBM. To evaluate $\boldsymbol{\tau}^- \cdot \mathbf{n}^-$, we can perform a stress balance on the fluid inside the particle, shown in Figure 7.3b. The integral form of the Navier-Stokes equations together with the divergence theorem give us

$$\int_{\Omega^-_{CV}} \rho_f \frac{\partial \mathbf{u}}{\partial t} \, \mathrm{d}V + \int_{\Gamma^-_{CV}} \rho_f (\mathbf{u}\mathbf{u}) \cdot \mathbf{n}^- \, \mathrm{d}A = \int_{\Gamma^-_{CV}} \boldsymbol{\tau}^- \cdot \mathbf{n}^- \, \mathrm{d}A + \int_{\Omega^-_{CV}} \mathbf{f}_b \, \mathrm{d}V, \tag{7.6}$$

where $\Gamma^-_{CV} = \Gamma^p_{CV} \cup \Gamma^-_y$. We set the first term to zero because, at steady-state, the fluid velocity within the particle does not change in time. The convective terms are zero at the particle interface Γ^p_{CV} due to the no-slip condition. Then, (7.6) reduces to

$$\int_{\Gamma^-_y} \rho_f (\mathbf{u}\mathbf{u}) \cdot \mathbf{n}^- \, \mathrm{d}A = \int_{\Gamma^p_{CV}} \boldsymbol{\tau}^- \cdot \mathbf{n}^- \, \mathrm{d}A + \int_{\Gamma^-_y} \boldsymbol{\tau}^- \cdot \mathbf{n}^- \, \mathrm{d}A + \int_{\Omega^-_{CV}} \mathbf{f}_b \, \mathrm{d}V. \tag{7.7}$$

Using (7.7) together with (7.5), we obtain

$$\int_{\Gamma^p_{CV}} \boldsymbol{\tau}^+ \cdot \mathbf{n}^+ \, \mathrm{d}A = \int_{L_{CV}} \mathbf{f}_{IBM} \, \mathrm{d}V - \int_{\Gamma^-_y} \rho_f (\mathbf{u}\mathbf{u}) \cdot \mathbf{n}^- \, \mathrm{d}A + \int_{\Gamma^-_y} \boldsymbol{\tau}^- \cdot \mathbf{n}^- \, \mathrm{d}A + \int_{\Omega^-_{CV}} \mathbf{f}_b \, \mathrm{d}V. \tag{7.8}$$

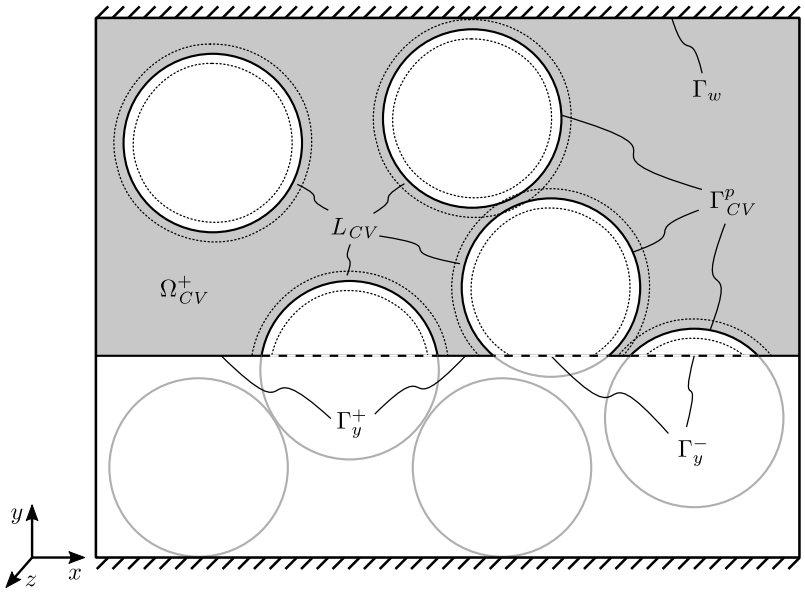

Figure 7.4: Shaded control volume for the general case involving multiple particles. The indicated volumes and surfaces are all those required for (7.9)

Finally, combining (7.8) and (7.4) gives us

$$\underbrace{\int_{\Gamma_w} \boldsymbol{\tau}^+ \cdot \mathbf{n}^+ \,\mathrm{d}A + \int_{\Omega_{CV}} \mathbf{f}_b \,\mathrm{d}V}_{\text{External force}} = \underbrace{-\int_{\Gamma_y^+} \boldsymbol{\tau}^+ \cdot \mathbf{n}^+ \,\mathrm{d}A + \int_{\Gamma_y^+} \rho_f(\mathbf{uu}) \cdot \mathbf{n}^+ \,\mathrm{d}A}_{\text{Fluid force}}$$
$$\underbrace{-\int_{L_{CV}} \mathbf{f}_{IBM} \,\mathrm{d}V - \int_{\Gamma_y^-} \boldsymbol{\tau}^- \cdot \mathbf{n}^- \,\mathrm{d}A + \int_{\Gamma_y^-} \rho_f(\mathbf{uu}) \cdot \mathbf{n}^- \,\mathrm{d}A}_{\text{Particle force}}, \tag{7.9}$$

where $\Omega_{CV} = \Omega^+_{CV} \cup \Omega^-_{CV}$. The left-hand side of (7.9) contains the external forces acting on the control volume from the top wall, Γ_w, and the body force applied to the whole volume, Ω_{CV}. These external forces are balanced by fluid and particle forces within and at the lower boundary of the control volume. Figure 7.4 presents an illustration of the control volume for the general case involving multiple particles. The fluid force consists of pressure and viscous stresses as well as convective flow, all of which act at the lower boundary outside the particles, Γ^+_y. The particle force consists of the IBM force, which

acts throughout the control volume over L_{CV}, and convective and fluid stresses, which act at the lower boundary inside the particles, Γ_y^-. Note that the fluid inside the particles is only considered for those particles cut by the control volume; for particles wholly inside the control volume, the IBM force alone accounts for the effect of the particles acting on the fluid.

Fluid phase momentum in the x-direction

We now consider the momentum balance over the control volume in the x-direction. At the top wall, Γ_w, the pressure does not contribute to the x-momentum, and the vertical velocity, v, is zero, so that only $\mu_f \partial u/\partial y$ contributes to the fluid stress. At the lower boundary, Γ_y, the pressure again does not play a role, but we keep the complete viscous terms and convective terms for generality. Due to the periodic boundaries, $\int_{\Gamma_y} \partial v/\partial x \, \mathrm{d}A = 0$, but the integrals of this quantity in the separate domains Γ_y^+ and Γ_y^- can be nonzero, so we leave the expression in the more general form:

$$\underbrace{\int_{\Gamma_w} \mu_f \frac{\partial u}{\partial y} \, \mathrm{d}A + \int_{\Omega_{CV}} f_{b,x} \, \mathrm{d}V}_{\text{External force}} = \underbrace{\int_{\Gamma_y^+} \mu_f \left(\frac{\partial u}{\partial y} + \frac{\partial v}{\partial x} \right) \mathrm{d}A - \int_{\Gamma_y^+} \rho_f uv \, \mathrm{d}A}_{\text{Fluid force}}$$
$$\underbrace{- \int_{L_{CV}} f_{IBM,x} \, \mathrm{d}V + \int_{\Gamma_y^-} \mu_f \left(\frac{\partial u}{\partial y} + \frac{\partial v}{\partial x} \right) \mathrm{d}A - \int_{\Gamma_y^-} \rho_f uv \, \mathrm{d}A}_{\text{Particle force}} . \tag{7.10}$$

It is important to note that here we are explicitly separating the stresses arising from the fluid and particle phases. We could consider all the viscous and convective terms acting along both Γ_y^+ and Γ_y^- to be the fluid stress terms and likewise consider only the f_{IBM} term to be the particle stress, as was done in Kidanemariam and Uhlmann [112]. However, while this method may be accurate in recovering the overall stress, it may not

be accurate in apportioning the stress between the fluid and particle phases (unless the viscous and convective stresses within the particles are negligible).

Dividing by the area of the domain and using the definition of the horizontal average,

$$\langle \theta \rangle = \frac{1}{L_x L_z} \int_0^{L_z} \int_0^{L_x} \theta \, \mathrm{d}x \, \mathrm{d}z, \tag{7.11}$$

we can rewrite (7.10) as

$$\underbrace{\mu_f \left\langle \left. \frac{\partial u}{\partial y} \right|_{L_y} \right\rangle + f_{b,x}(L_y - y)}_{\text{External stress}} = \underbrace{\mu_f \left\langle \gamma \left(\frac{\partial u}{\partial y} + \frac{\partial v}{\partial x} \right)_y \right\rangle - \rho_f \left\langle \gamma uv|_y \right\rangle}_{\text{Fluid stress}}$$
$$\underbrace{- \int_y^{L_y} \langle f_{IBM,x} \rangle \, \mathrm{d}y + \mu_f \left\langle \phi \left(\frac{\partial u}{\partial y} + \frac{\partial v}{\partial x} \right)_y \right\rangle - \rho_f \left\langle \phi uv|_y \right\rangle}_{\text{Particle stress}}, \tag{7.12}$$

where γ is an indicator function for the fluid volume fraction ($\gamma = 1$ outside the particle and $\gamma = 0$ inside the particle) and ϕ is an indicator function for the particle volume fraction ($\phi = 1 - \gamma$), as was done in the volume-averaging of Nikora et al. [111]. We have also used the fact that μ_f, ρ_f, and $f_{b,x}$ are constant throughout the domain.

Fluid phase momentum in the y-direction

For the y-velocity component, the pressure, in addition to the viscous stress, contributes to the fluid stress tensor at the boundaries Γ_w and Γ_y^+, but only the vv component

contributes to the convective term, reducing (7.9) to the following:

$$\underbrace{-\int_{\Gamma_w} p\,\mathrm{d}A + \int_{\Gamma_w} 2\mu_f \frac{\partial v}{\partial y}\,\mathrm{d}A}_{\text{External force}} = \underbrace{-\int_{\Gamma_y^+} p\,\mathrm{d}A + \int_{\Gamma_y^+} 2\mu_f \frac{\partial v}{\partial y}\,\mathrm{d}A - \int_{\Gamma_y^+} \rho_f vv\,\mathrm{d}A}_{\text{Fluid force}}$$
$$\underbrace{-\int_{L_{CV}} f_{IBM,y}\,\mathrm{d}V - \int_{\Gamma_y^-} p\,\mathrm{d}A + \int_{\Gamma_y^-} 2\mu_f \frac{\partial v}{\partial y}\,\mathrm{d}A - \int_{\Gamma_y^-} \rho_f vv\,\mathrm{d}A}_{\text{Particle force}}. \tag{7.13}$$

We have also set $f_{b,y} = 0$. On the left-hand side, the external force consists of the pressure and viscous stress acting at the top wall. This force is balanced on the right-hand side by the fluid force, consisting of the fluid pressure, viscous stress, and convection outside the particles at the lower boundary of the control volume, and the particle force, consisting of the IBM force throughout the control volume as well as the pressure, viscous stress, and convection of the fluid within the particles but by the lower wall of the control volume. Again, dividing by the domain area and applying the averaging operator, we can reduce (7.13) to

$$\underbrace{-\left\langle p|_{L_y}\right\rangle + 2\mu_f \left\langle \left.\frac{\partial v}{\partial y}\right|_{L_y}\right\rangle}_{\text{External stress}} = \underbrace{-\left\langle \gamma p|_y\right\rangle + 2\mu_f \left\langle \left.\gamma\frac{\partial v}{\partial y}\right|_y\right\rangle - \rho_f \left\langle \gamma vv|_y\right\rangle}_{\text{Fluid stress}}$$
$$\underbrace{-\int_y^{L_y} \langle f_{IBM,y}\rangle\,\mathrm{d}y - \left\langle \phi p|_y\right\rangle + 2\mu_f \left\langle \left.\phi\frac{\partial v}{\partial y}\right|_y\right\rangle - \rho_f \left\langle \phi vv|_y\right\rangle}_{\text{Particle stress}}. \tag{7.14}$$

7.3.2 Particle phase balance

Although the fluid stress analysis accounts for the effects of the particles through the IBM force, we can also perform an analysis on the particle phase by itself in order to ensure that the particle momentum also closes and to try to bridge the two balances into

a single one for the mixture as a whole. Additionally, rheological descriptions require information about the particle pressure, which we can only obtain by analyzing the particle phase. We can apply the coarse-graining method to (2.9) to obtain

$$\mathbf{a}^{cg} = \mathbf{F}_r^{cg} + \mathbf{F}_{IBM}^{cg} + \mathbf{F}_g^{cg} + \mathbf{F}_c^{cg}, \tag{7.15}$$

where

$$\mathbf{a}^{cg}(\mathbf{x}, t) = \sum_{p=1}^{N_p} m_p \frac{\mathrm{d}\mathbf{u}_p}{\mathrm{d}t} \mathcal{W}(\mathbf{x} - \mathbf{x}_p) \tag{7.16}$$

is the coarse-grained local particle acceleration, and

$$\mathbf{F}_{IBM}^{cg} = \sum_{p=1}^{N_p} \mathbf{F}_{IBM,p} \mathcal{W}(\mathbf{x} - \mathbf{x}_p) \tag{7.17}$$

is the coarse-grained IBM force (likewise for the other forces acting on the particle center of mass). The coarse-graining function, $\mathcal{W}(\mathbf{r})$, spreads the particle-centered quantities onto an Eulerian mesh, allowing us to treat them as a continuum field.

We also write the collision force $\mathbf{F}_{c,p}$ slightly differently from the previous expression (4.3) in order to more clearly refer to its different components. Instead, we write

$$\mathbf{F}_{c,p} = \mathbf{F}_{n,p} + \mathbf{F}_{t,p} + \mathbf{F}_{l,p} + \mathbf{F}_{w,p}, \tag{7.18}$$

where $\mathbf{F}_{n,p}$ accounts for all normal contacts with the walls and other particles, $\mathbf{F}_{t,p}$ accounts for all frictional contacts, and $\mathbf{F}_{l,p}$ account for all lubrication interactions. In this chapter, we additionally consider $\mathbf{F}_{w,p}$, which is the "wall force" required to hold a fixed particle p in place, and is equal and opposite to the hydrodynamic and other collision forces acting on the fixed particle. We include this force in order to close the momentum balance for the flow over a particle bed, which uses fixed particles acting as a rough lower

wall, in Section 7.4.2.

Similar to the fluid stresses, we can analyze the coarse-grained particle forces within a control volume spanning the entire domain in the streamwise and spanwise directions and extending from the top wall to an arbitrary height y. Integrating (7.15) over this volume, we obtain

$$\int\limits_{\Omega_{CV}} \mathbf{a}^{cg}\,\mathrm{d}V = \int\limits_{\Omega_{CV}} \left(\mathbf{F}_r^{cg} + \mathbf{F}_{IBM}^{cg} + \mathbf{F}_g^{cg} + \mathbf{F}_c^{cg}\right)\,\mathrm{d}V. \tag{7.19}$$

We can again apply the averaging operator to recast (7.19) as a line integral in the wall-normal direction:

$$\int_y^{L_y} \langle \mathbf{a}^{cg} \rangle\,\mathrm{d}y = \int_y^{L_y} \left(\langle \mathbf{F}_r^{cg} \rangle + \langle \mathbf{F}_{IBM}^{cg} \rangle + \left\langle \mathbf{F}_g^{cg} \right\rangle + \langle \mathbf{F}_c^{cg} \rangle\right)\,\mathrm{d}y. \tag{7.20}$$

If the particles are in a steady state, either naturally or through double-averaging, then the acceleration term would be zero. We can also decompose the equation into components in the x-direction,

$$\underbrace{\int_y^{L_y} \left\langle F_{r,x}^{cg} \right\rangle\,\mathrm{d}y + \int_y^{L_y} \left\langle F_{IBM,x}^{cg} \right\rangle\,\mathrm{d}y}_{\text{Hydrodynamic stress}} + \underbrace{\int_y^{L_y} \left\langle F_{c,x}^{cg} \right\rangle\,\mathrm{d}y}_{\text{Collision stress}} = 0, \tag{7.21}$$

where the gravitational force is zero, and the y-direction,

$$\underbrace{-\int_y^{L_y} \left\langle F_g^{cg} \right\rangle\,\mathrm{d}y}_{\text{Bed weight}} = \underbrace{\int_y^{L_y} \left\langle F_{r,y}^{cg} \right\rangle\,\mathrm{d}y + \int_y^{L_y} \left\langle F_{IBM,y}^{cg} \right\rangle\,\mathrm{d}y}_{\text{Hydrodynamic stress}} + \underbrace{\int_y^{L_y} \left\langle F_{c,y}^{cg} \right\rangle\,\mathrm{d}y}_{\text{Collision stress}}. \tag{7.22}$$

7.3.3 Mixture balance

Instead of considering the fluid and particle phases separately, we could combine them into a single mixture. For example, in the x-direction, equating the particle stress on the fluid in (7.12) to the hydrodynamic stress on the particles in (7.21), we obtain

$$\underbrace{\mu_f \left\langle \left.\frac{\partial u}{\partial y}\right|_{L_y} \right\rangle + f_{b,x}(L_y - y)}_{\text{External stress}} = \underbrace{\mu_f \left\langle \gamma \left(\frac{\partial u}{\partial y} + \frac{\partial v}{\partial x} \right)_y \right\rangle - \rho_f \left\langle \gamma u v|_y \right\rangle}_{\text{Fluid stress}} \underbrace{- \int_y^{L_y} \left\langle F_{c,x}^{cg} \right\rangle \, \mathrm{d}y}_{\text{Collision stress}} . \tag{7.23}$$

This formulation has several advantages over the separate phase balances. First, the collision information for the particles is generally more readily available from simulation results than the Eulerian IBM data is. Second, we can reformulate the coarse-grained collision stress as a stress acting over the lower surface of the control volume instead of a force integrated over the volume:

$$\int_y^{L_y} \left\langle F_{c,x}^{cg} \right\rangle \, \mathrm{d}y = \left\langle \sigma_{xy}^{cg} \right\rangle , \tag{7.24}$$

where σ_{xy}^{cg} is the xy-component of a coarse-grained particle collision stress, such as that given by (6.4). While the collision force in (7.23) can only provide information in the x-, y-, and z-directions and must be integrated over a volume, the stress tensor $\boldsymbol{\sigma}^{cg}$ can provide more information about shear and normal stresses in the particle phase without averaging over volumes, as shown in Section 6.3. However, for the momentum balance in this chapter, we found (7.24) to be valid, allowing us to use the coarse-grained collision force instead of the collision stress.

7.4 Results

7.4.1 Stress balance of a single rolling particle

Stress balance of the fluid phase in the x-direction

Having established momentum balance relationships (7.12) (7.21), we will now apply them to the single rolling sphere case described in Section 7.2.1. Figure 7.5 shows the x-momentum balance of the fluid phase, given by (7.12). The stresses are a function of the y-coordinate, where each value of σ_x corresponds to the control volume extending from the top wall to the y-coordinate. The reference stress for these plots is the wall shear stress for the reference case, $\sigma_{ref} = \mu_f \mathrm{d}u/\mathrm{d}y|_{y=0}$.

Figure 7.5a shows the instantaneous particle, fluid, and external stresses at $t = 2.5t_{ref}$. As expected, the external stress is in equilibrium with the total stress, which is the sum of the fluid and particle stresses. Thus, the steady state of the simulation is valid for this analysis, in which we neglected the time-dependent terms to obtain (7.12). For control volumes above the particle ($y/L_y > 0.5$), the particle stress is zero, and the external stress is balanced entirely by the fluid stress. However, in the lower half of the domain, where the particle is located, the particle stress accounts for most of the stress in the associated control volumes. Note that, in this simulation, the particle diameter fills half the domain in the streamwise and spanwise directions ($L_x = 2D_p$, $L_z = 2D_p$). Thus, the particle has a significant effect on the horizontally-averaged stresses. In contrast, we would expect a single particle in a much larger domain to have a much smaller effect on the flow and likewise to have a much smaller particle stress relative to the fluid stress. Near the lower wall ($y/L_y < 0.1$), a decrease in particle stress and increase in fluid stress indicates a transfer of x-momentum back to the fluid. The total drag on the particle, given by the particle stress at the lower wall, is thus only a small fraction of the drag

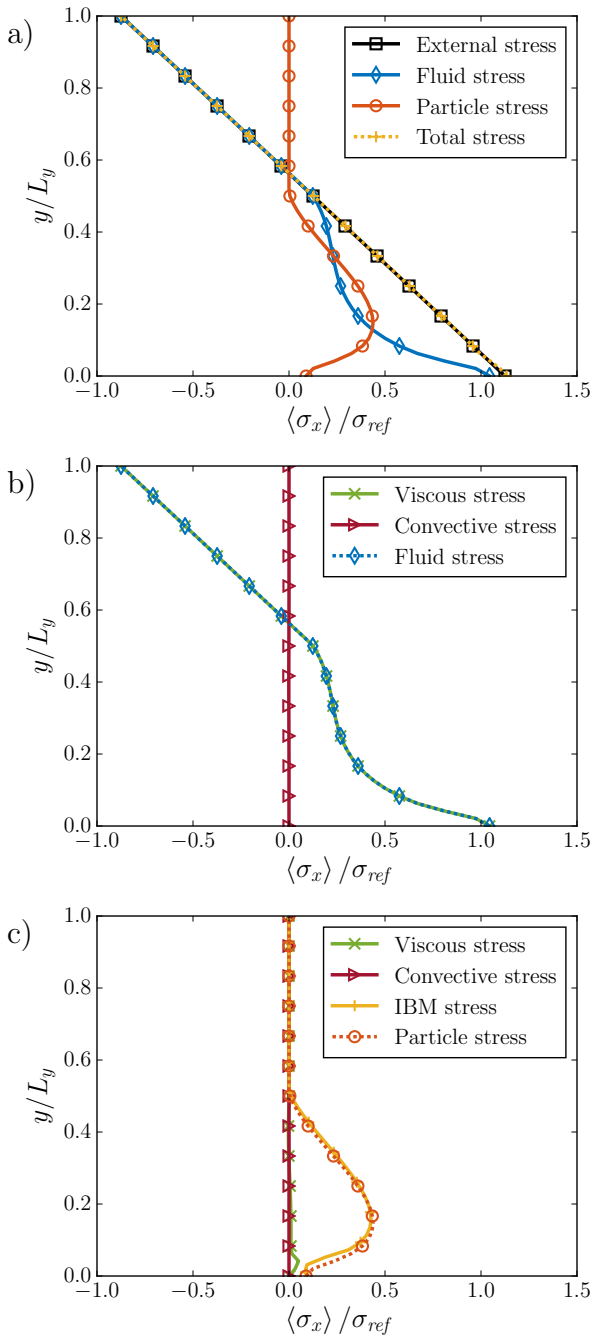

Figure 7.5: Single particle stress balance of the fluid phase in the x-direction according to (7.12). The total stress is the sum of the fluid and particle stresses. The components of (a) are further broken down for the (b) fluid stress and (c) particle stress.

experienced by the upper half of the particle.

Based on our definition of σ_{ref}, in the absence of the particle, the external stress in Figure 7.5a would extend from $\sigma_x/\sigma_{ref} = -1$ at $y/L_y = 1$ to $\sigma_x/\sigma_{ref} = 1$ at $y/L_y = 0$. The presence of the particle causes this curve to shift to the right, decreasing the magnitude of the stress at the top wall and increasing the stress at the bottom wall. This rightward shift results in a decrease in the fluid velocity in the upper half of the domain. At the lower wall, the fluid stress is close to $\sigma_x/\sigma_{ref} = 1$, while the rightward shift in the external stress results from the particle stress at the lower wall. The collisional friction with the lower wall, therefore, accounts for a large portion of the decrease in the flow rate relative to the reference case.

The fluid stress in Figure 7.5a is further decomposed into its components in Figure 7.5b, which shows the relative contributions from the convective stress, $-\rho_f \langle \gamma uv|_y \rangle$, and the viscous stress, $\mu_f \langle \gamma(\partial u/\partial y + \partial v/\partial x)_y \rangle$, given in (7.12). The convective term is negligible, so that the viscous term alone accounts for the fluid stress. Though we do not show it here, we also found the $\partial v/\partial x$ term to be negligible.

Likewise, the particle stress in Figure 7.5a is further decomposed into its components in Figure 7.5c, which include the IBM, viscous, and convective stresses comprising the particle stress in (7.12). The IBM term is dominant, the convective term is negligible, and the viscous term is detectable near the lower wall. In summary, we could remove the negligible terms from (7.12) to obtain

$$\underbrace{\mu_f \left\langle \left.\frac{\partial u}{\partial y}\right|_{L_y} \right\rangle + f_{b,x}(L_y - y)}_{\text{External stress}} = \underbrace{\mu_f \left\langle \gamma \left.\frac{\partial u}{\partial y}\right|_{y} \right\rangle}_{\text{Fluid stress}} \underbrace{- \int_y^{L_y} \langle f_{IBM,x} \rangle \, \mathrm{d}y + \mu_f \left\langle \phi \left.\frac{\partial u}{\partial y}\right|_{y} \right\rangle}_{\text{Particle stress}}. \tag{7.25}$$

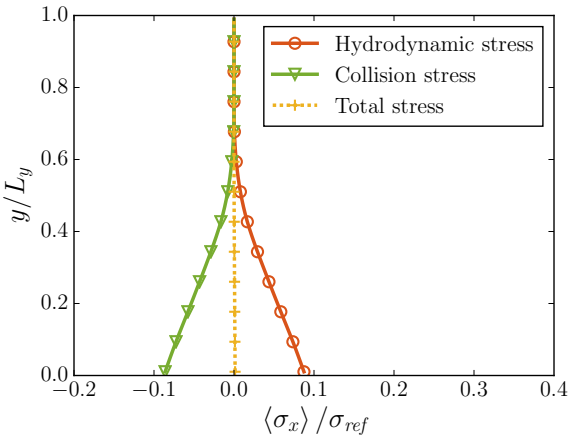

Figure 7.6: Single particle stress balance of the particle phase in the x-direction according to (7.21). The total stress is the sum of the hydrodynamic and collision stresses.

Stress balance of the particle phase in the x-direction

Figure 7.6 shows the momentum balance for (7.21), in which the total stress, the sum of the hydrodynamic and collision stresses, is zero. Thus, the hydrodynamic force driving the particle in the positive x-direction is balanced by the collision forces acting in the negative x-direction, indicating that the particle is not accelerating. For a single particle, this figure shows only the net hydrodynamic force, $\mathbf{F}_{r,p}+\mathbf{F}_{IBM,p}$, and net collision force, $\mathbf{F}_{c,p}$, smeared by the coarse-graining method. Thus, there exist stresses above the particle diameter ($y/L_y > 0.5$) because the coarse-graining width we chose spreads values beyond the particle radius. Furthermore, the stress at the lower wall represents the total stress (e.g. $\mathbf{F}_{c,p}/(L_x\,L_z)$) acting on the particle. At the lower wall, the particle stress in Figure 7.5a matches the hydrodynamic stress in Figure 7.6, which is balanced by the collision stress. Therefore, the particle stress at the lower wall in Figure 7.5a represents the stress between the particle and wall due to collision forces.

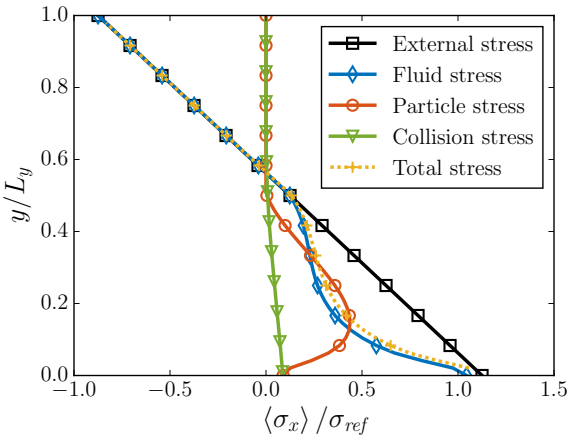

Figure 7.7: Stress balance in the x-direction for the fluid/particle mixture, given by (7.23). The total stress is the sum of the fluid and collision stresses.

Stress balance of the fluid/particle mixture in the x-direction

We can also consider the momentum balance for the mixture, given by (7.23) and shown in Figure 7.7. While the total stress, which is the sum of the fluid and collision stresses, does match the external stress in the clear fluid layer above the particle and at the lower wall, it does not match the external stress within the particle region. To understand this imbalance, we have included in this plot the particle stress, which represents the local hydrodynamic interactions that occur along the particle surface. The particle stress and collision stress should be equivalent because the entire system is in equilibrium. However, they match only at the lower wall because the coarse-graining method simply smears the collision stress over the volume, and the collision stress matches the net hydrodynamic stress acting on the particle center of mass, which does not account for local variations along its surface. Thus, using hybrid fluid/coarse-grained quantities does not close the momentum budget unless the entire particle is considered.

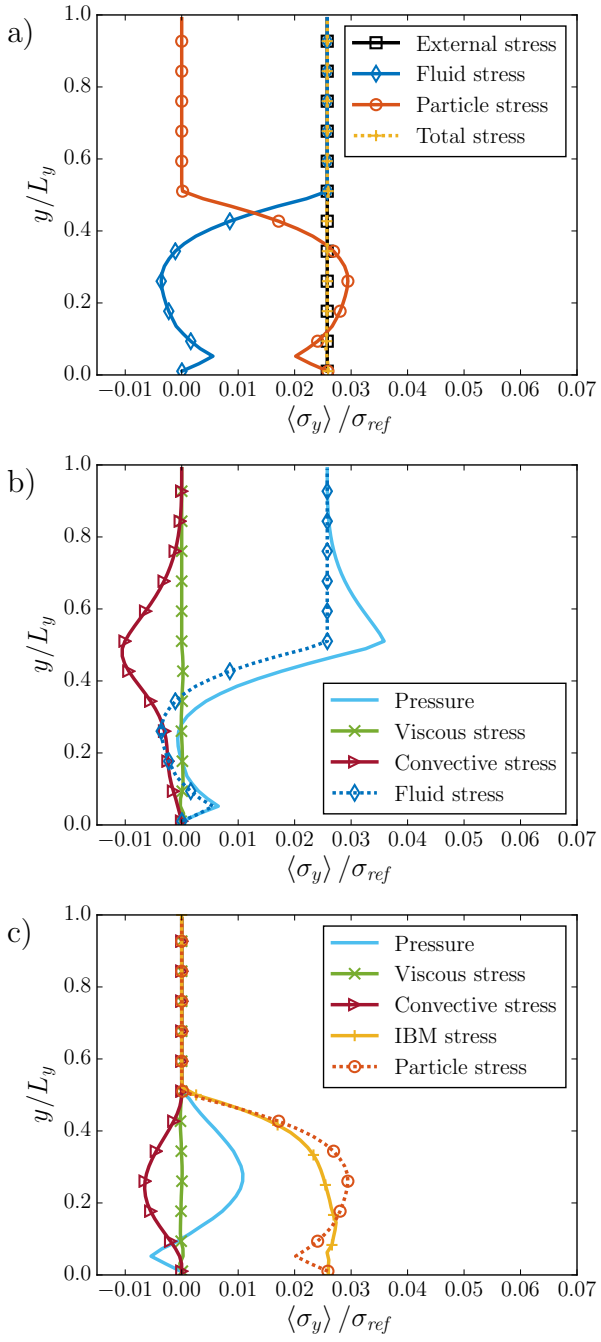

Figure 7.8: Single particle stress balance of the fluid phase in the y-direction according to (7.14). The total stress is the sum of the fluid and particle stresses. The components of (a) are further broken down for the (b) fluid stress and (c) particle stress. Note that "pressure" refers to the pressure term in (7.14), which is the negative pressure.

Stress balance of the fluid phase in the y-direction

We present the results for the momentum balance of the fluid phase in the y-direction, given by (7.14), in Figure 7.8. Figure 7.8a shows the balance between the external stress, comprised of the pressure and viscous terms at the top wall, and the total stress, which is the sum of fluid and particle stresses. Different from the x-momentum balance, the external stress for the y-momentum fluid phase does not depend on the y-coordinate, instead maintaining a constant value. All pressures evaluated here are relative to the pressure at the lower wall. In (7.14) the stresses scale with the negative pressure, so the positive external stress in Figure 7.8a thus indicates a lower, or negative, pressure in the fluid at the top wall relative to the bottom wall. This stress is carried exclusively by the fluid in the upper half of the domain and is then almost completely transferred to the particle in the lower half of the domain. The particle stress represents the lift force acting on the particle phase, and its value at the lower wall represents the total lift acting on the particle. The majority of the lift stress occurs along the top of the particle ($0.4 < y/L_y < 0.5$). The particle stress at the lower wall is equivalent to the external stress or the fluid stress at the upper wall. Thus, the lift force on the particle is supported by a negative pressure in the fluid at the upper wall. However, the maximum fluid stresses for the y-momentum balance in Figure 7.8a are up to two orders of magnitude smaller than those for the x-momentum balance in Figure 7.5a.

Figure 7.8b decomposes the fluid stress in Figure 7.8a into the pressure, viscous, and convective terms, given by $-\langle \gamma p|_y \rangle$, $2\mu_f \langle \gamma \partial v/\partial y|_y \rangle$, and $-\rho_f \langle \gamma v v|_y \rangle$ in (7.14), respectively. Similarly, Figure 7.8c decomposes the particle stress in Figure 7.8a into the IBM, pressure, viscous, and convective terms comprising the particle stress in (7.14). Contrary to the x-momentum balance, we find the pressure and convective stress to be significant

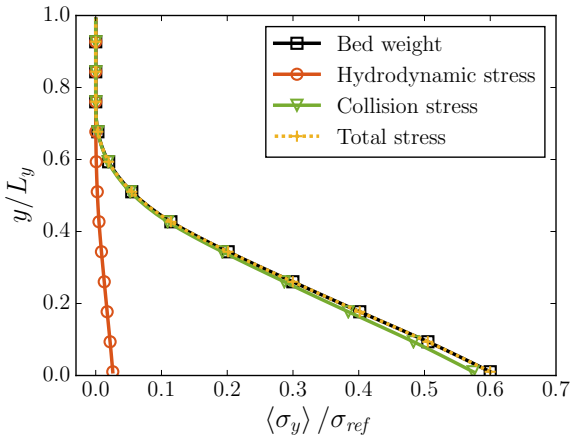

Figure 7.9: Single particle stress balance of the particle phase in the y-direction according to (7.22). The total stress is the sum of the hydrodynamic and collision stresses.

and the viscous stress to be negligible. We can thus simplify (7.14) to obtain

$$\underbrace{-\left\langle p|_{L_y}\right\rangle}_{\text{External stress}} = \underbrace{-\left\langle \gamma p|_y\right\rangle - \rho_f\left\langle \gamma vv|_y\right\rangle}_{\text{Fluid stress}} \underbrace{-\int_y^{L_y}\langle f_{IBM,y}\rangle\,\mathrm{d}y - \left\langle \phi p|_y\right\rangle - \rho_f\left\langle \phi vv|_y\right\rangle}_{\text{Particle stress}}. \tag{7.26}$$

Note that the IBM stress matches the particle stress only at the lower wall; accounting for the pressure and convective terms inside the particle is important for resolving the particle stress throughout the domain.

Stress balance of the particle phase in the y-direction

Figure 7.9 shows the stress balance for the particle phase given by (7.22), in which the bed weight is in equilibrium with the total stress, which is the sum of the hydrodynamic stress and the collision stress. In this case, the bed weight represents the gravitational force, $\mathbf{F}_{g,p}$, smeared by the coarse-graining method. The fluid exerts a positive lift force on the particle, but the vast majority of the particle's weight is supported by the collision

force with the lower wall. Comparing Figure 7.6 to Figure 7.9, we can see that the hydrodynamic lift stress is a fraction of the drag stress, but the y-momentum collision stress is six times larger than the drag stress. In fact, the bed weight and collision stress are the only terms in the y-momentum balance that are comparable in magnitude to the stresses in the x-momentum balance. Having validated these methods for a simple test case, we will now apply them to simulations involving many particles.

7.4.2 Stress balance of a sheared particle bed

Time evolution of the particle bed

We conducted simulations of a Poiseuille flow over a particle bed at four different flow rates: one to initialize the bed and three to study the bed under different flow conditions. The time evolution of these simulations is shown in Figure 7.10. Figure 7.10a shows the particle flux, q_p, over time for the different simulation runs, where we use the volumetric particle flux per unit width

$$q_p = \frac{1}{L_x L_z} \sum_{p=1}^{N_p} V_p u_{p,x}. \tag{7.27}$$

The particle flux rapidly increases during run Re67, and is accompanied by an increase in the bed height, h_p, or dilation of the particle bed, as shown in Figure 7.10b. We define the bed height to be the location at which $\langle \phi \rangle = 0.05$ to be consistent with our definition in Section 5.3. Upon resuming run Re67 at a lower pressure gradient, we can see that run Re17 quickly reaches a steady-state configuration, characterized by a constant particle flux and bed height, while run Re33 does not reach a steady-state since the particle flux and bed height continue to increase in time. Run Re8, which was resumed from run Re17, experiences a further decrease in the particle flux and bed height, reaching a somewhat steady particle flux but a still slightly-decreasing bed height. Figure 7.11

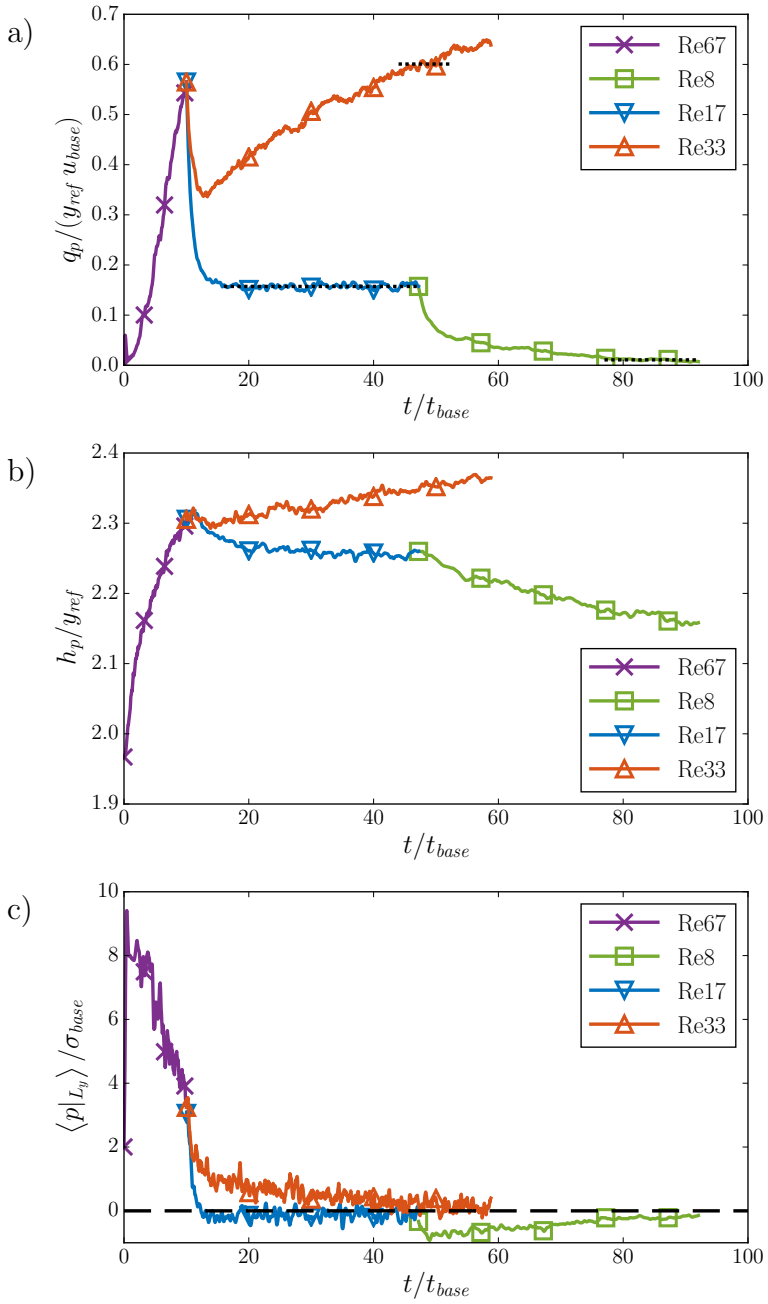

Figure 7.10: (a) Particle volumetric flux, given by (7.27), for the different simulation runs. Dotted lines indicate the average particle flux over the averaging time for each simulation. (b) Bed height, defined at $\langle\phi\rangle = 0.05$. (c) Spatially-averaged fluid pressure at the top wall, relative to the lower wall and neglecting hydrostatics.

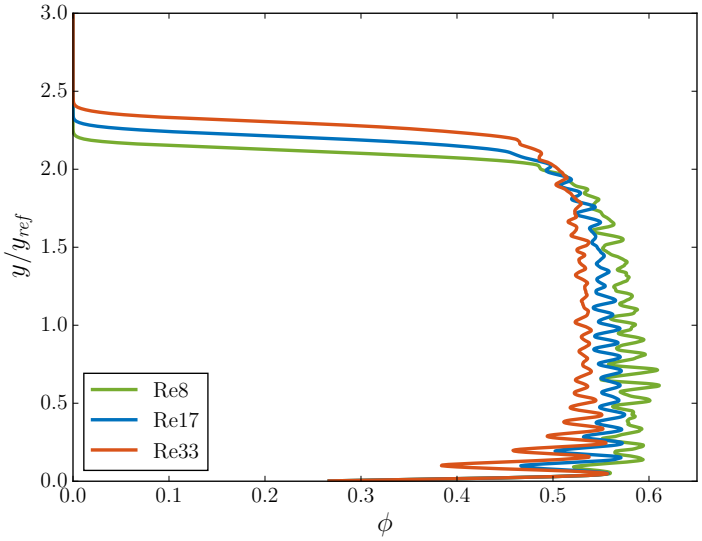

Figure 7.11: Average particle volume fraction profiles for the different simulation runs.

shows the volume fractions of the beds for the three simulations, where the bed height clearly increases for the higher flow rates. Accompanying this dilation is a decrease in the volume fraction of particles within the bed. These three simulations provide an opportunity to study the forces behind particle bed evolution. Clearly, the unsteady flows experience some type of force imbalance that causes the bed to dilate or contract in order to reach a steady state.

We will investigate the momentum balances of these simulations in part to understand these bed transitions. We will primarily focus on runs Re8, which is at steady-state, and Re33, which is not at a steady-state, due to their different flow conditions. Figure 7.12 shows the fluid and particle velocity profiles from the simulations together with the velocity profile for the reference Poiseuille case. We can see that there is no slip between the fluid and particle phases and that the reference velocity, u_{ref}, provides a reasonable estimate for the fluid velocity in the clear fluid layer above the particles ($y/y_{ref} > 2.3$), even when the entire particle bed is in motion. However, increasing the flow rate does

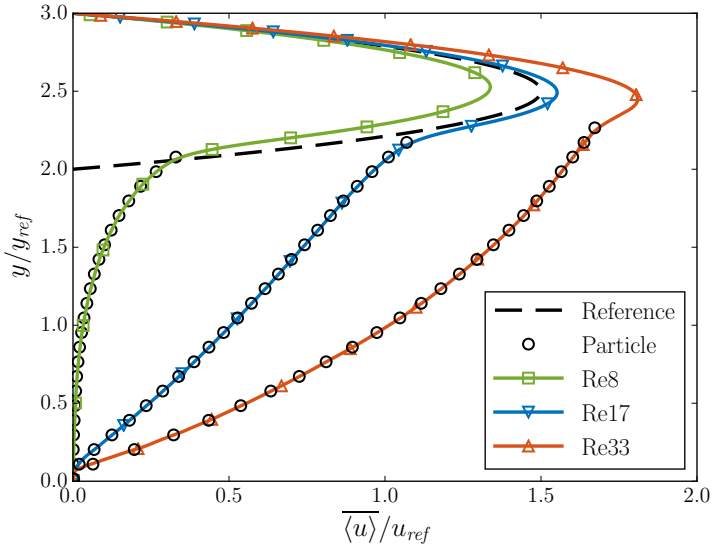

Figure 7.12: Average fluid velocity profiles for the different simulation runs, along with the average coarse-grained particle velocity profiles, given by (6.2), and the velocity profile for the reference case.

increase the velocity profile relative to the reference case. There is a clear qualitative difference between run Re8, whose velocity profile is concave and goes to zero within the bed at $y/y_{ref} \approx 0.5$, and run Re33, whose velocity profile is convex and goes to zero only at the fixed particles at the lower wall. For brevity, we will neglect the momentum balance for Re17, which is similar in bed morphology to Re33 and in steady-state characteristics to Re8.

As described in Section 7.2.2, we use time averages to smooth out the fluctuations due to particle-particle interactions. These time averages, which were used to generate Figures 7.12 and 7.11 as well as the stress balance results, are given in Table 7.3 and shown graphically by the dotted lines in Figure 7.10a. While this figure does not suggest it, we will actually find the stress balance for run Re33 to be in equilibrium for this time-averaging window. Considering that the particle flux and bed height change slowly relative to the flow timescale, it makes sense that the "accelerations" responsible for the change in particle flux and bed height are undetectable in the stress balance. However,

we can observe the unsteady nature of the flows through the y-stress balance. Consider the pressure at the top wall as a function of time, shown in Figure 7.10c. Recall from Section 7.4.1 that a negative pressure at the top wall corresponds to a lift force acting on the particle phase. Comparing Figures 7.10b and 7.10c, we can see a clear correlation between a positive pressure during bed dilation (increasing h_p), a negative pressure during bed contraction (decreasing h_p), and a slightly-negative pressure during steady-state. Thus, when the particle bed tries to dilate, the fluid immediately responds with a negative lift force, and in turn responds to bed contraction with a positive lift force. Alternatively, we can imagine that, when the bed dilates, a positive pressure forms above the bed as fluid flows into the bed to fill the void space, while, when the bed contracts, a negative pressure forms above the bed as the particles squeeze fluid out of the bed.

Stress balance of the fluid phase in the x-direction

We now investigate the momentum balance for the simulations involving a bed of mobile particles, focussing on runs Re8 and Re33 to get a sense of the results for different flow conditions. In order to obtain steady-state results, we apply the time-averaging operator, (7.1), to the x-momentum balances (7.12) and (7.21), resulting in double-averaged equations akin to Nikora et al. [111] and Vowinckel et al. [110].

Figure 7.13 shows the momentum balance of the fluid phase, given by (7.12), for runs Re8 (left side) and Re33 (right side), in which we expect the external stress to match the total stress, which is the sum of the fluid and particle stresses. In Figures 7.13a and 7.13b, the external stress at the top wall is close to $\overline{\langle\sigma_x\rangle}/\sigma_{ref} = -1$, which is the stress at the top wall we would expect from the reference case. This result is consistent with the observation that the velocity profiles in Figure 7.12 are similar to that of the reference case, so that the chosen scaling seems appropriate. In the upper part of the flow ($y/y_{ref} > 2.3$), there are no particles, and the fluid stress matches all of the external

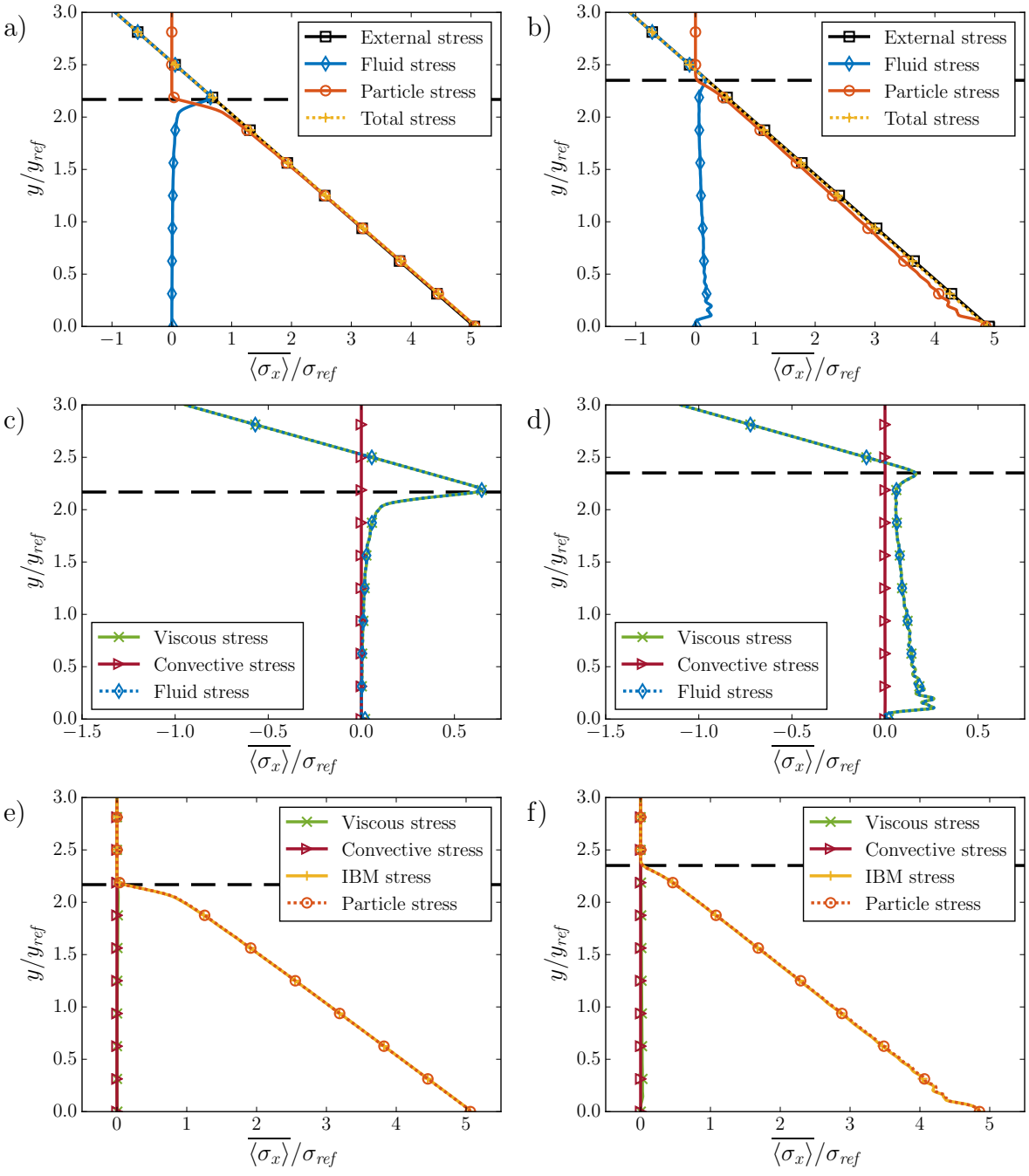

Figure 7.13: Particle bed stress balance of the fluid phase in the x-direction according to (7.12). Subfigures (a), (c), and (e) correspond to run Re8 while (b), (d), and (f) correspond to run Re33. The total stress is the sum of the fluid and particle stresses. The components of (a) and (b) are further broken down in (c) and (d) for the fluid stress and in (e) and (f) for the particle stress. The horizontal dashed line marks the height of the particle bed, h_p.

stress. Within the particle bed ($y/y_{ref} < 2.3$), however, the majority of the external stress is taken up by the particles.

Figures 7.13c and 7.13d show the terms in (7.12) that contribute to the fluid stress. The viscous term alone contributes to the fluid stress, which is consistent with the observations for the single rolling sphere. Run Re8 differs from Re33 in that the fluid stress reaches a higher positive value above the particle bed and quickly drops to zero within the particle bed. The fluid stress for Re33, on the other hand, reaches a somewhat constant value within the particle bed, increasing towards the lower wall. These results are consistent with the velocity profiles in Figure 7.12, where the concavity of the profile for Re8 results in a high shear stress at the fluid/particle bed interface and low stresses within the bed, and the convexity of the profile for Re33 results in a large shear stress at the lower wall.

Figures 7.13e and 7.13f, on the other hand, show the terms in (7.12) that contribute to the particle stress. Again, similar to the single sphere simulation, the IBM term alone contributes to the particle stress. The major differences in these curves between the two simulations is that the stress for Re8 increases rapidly at the fluid/particle bed interface, then gradually within the bed, whereas the stress for Re33 increases gradually at the fluid/particle interface and within the bed, and rapidly at the lower wall. This result is consistent with the locations of the sharp gradients in the fluid stress balance, so that the fluid and particle stresses together close the x-momentum balance.

Stress balance of the particle phase in the x-direction

Figure 7.14 shows the coarse-grained particle phase stresses, given by the time average of (7.21) for runs Re8 (left side) and Re33 (right side). In Figures 7.14a and 7.14b, the hydrodynamic stress propelling the particles in the positive x-direction and the collision stress slowing the particles in the negative x-direction are both zero above the particle

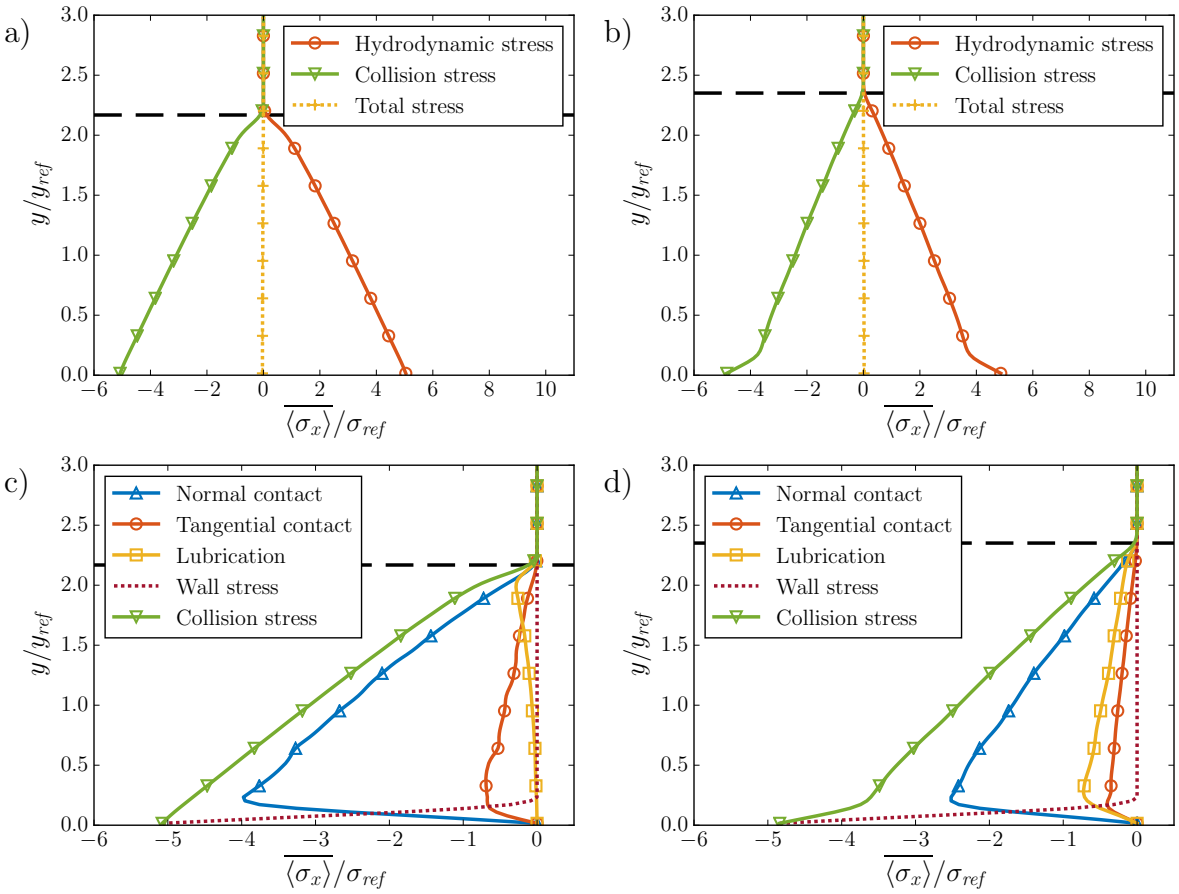

Figure 7.14: Particle bed stress balance of the particle phase in the x-direction according to (7.21). Subfigures (a) and (c) correspond to run Re8 while (b) and (d) correspond to run Re33. The total stress is the sum of the hydrodynamic and collision stresses. The components of the collision stresses in (a) and (b) are further broken down in (c) and (d) according to (7.18). The horizontal dashed line marks the height of the particle bed, h_p.

bed ($y/y_{ref} > 2.3$) and increase in magnitude deeper within the particle bed. The total stress, which is the sum of the hydrodynamic and collision stresses, is zero, indicating that the particle phase stress balance is also in equilibrium, even for the "unsteady" case, Re33. The hydrodynamic stress, and, due to equilibrium, the collision stress, has larger gradients at the fluid/particle bed interface for Re8 and at the lower wall for Re33, which is consistent with the locations of the larger particle stress gradients in Figures 7.13e and 7.13f.

Figures 7.14c and 7.14d show the terms in (7.18) that contribute to the collision stresses for runs Re8 and Re33, respectively. In both simulations, the normal contact forces dominate the collision stress, but the tangential contact (friction) and lubrication stresses do play important roles as well. Comparing these figures to the velocity profiles in Figure 7.12, we can see that the lubrication stress correlates with the shear rate, which is largest at the fluid/bed interface for Re8 and at the lower wall for Re33. This result is consistent with the fact that the lubrication force is dissipative and scales with the relative velocity between particles, similar to a viscous stress. In fact, for this reason, the fluid stresses within the particle beds in Figures 7.13c and 7.13d compare remarkably well qualitatively to the lubrication stresses. The tangential contact stress plays a larger role in the more static bed of run Re8, where the lubrication stress goes to zero, than it does in run Re33, where the lubrication stress exists throughout the bed. Finally, the wall stress, representing the force required to hold the fixed particles in place, is similar for both simulations, but there is a larger discontinuity with the other collision stresses for run Re33. As shown through the fluid phase balance, this result is due to the large fluid stress acting at the lower wall.

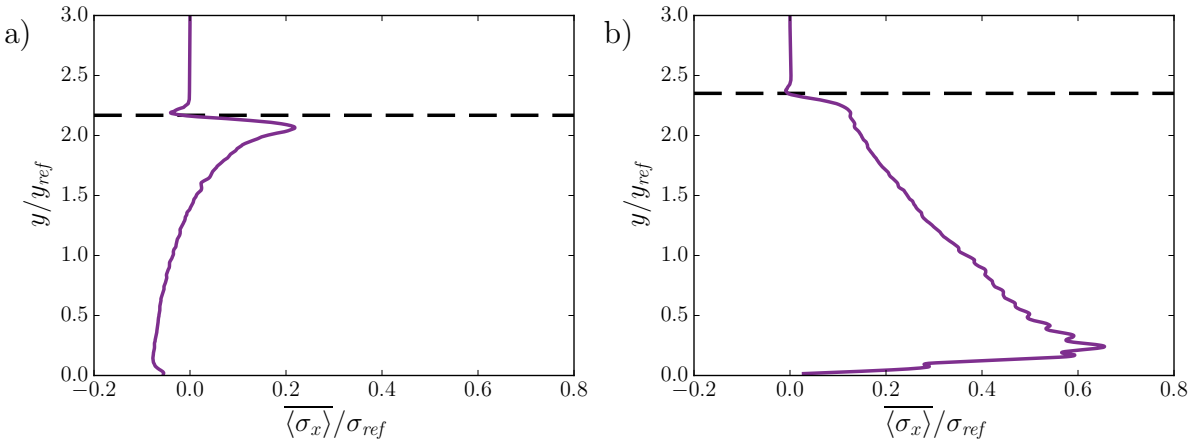

Figure 7.15: Particle bed stress balance in the x-direction for the fluid/particle mixture, given by (7.23), for (a) Run Re8 and (b) Run Re33. Shown is the difference between the external stress and the sum of the fluid and collision stresses. The horizontal dashed line marks the height of the particle bed, h_p.

Stress balance of the fluid/particle mixture in the x-direction

As we did in the case for the single rolling sphere, we can also look at the stress balance for the fluid/particle mixture, given by (7.23). As with the single rolling sphere case, the mixture balance does not close, so we present the imbalances (external minus fluid and collision stresses) for runs Re8 and Re33 in Figure 7.15. Considering the magnitude of stresses in the x-direction (Figure 7.13), these imbalances result in errors on the order of 10%. Figure 7.15a shows that the imbalance for Re8 is greatest in the upper portion of the particle bed. Figure 7.15b, on the other hand, shows a significant imbalance between the total stress and the external stress throughout the particle bed for Re33. Larger imbalances appear to correlate with larger shear rates in the fluid/particle velocity profiles (Figure 7.12). Therefore, one possible explanation for the imbalance is the same one we found for the single rolling sphere: the collision stress resolves the net fluid stress acting on the center of mass of the particles, not the stress differences that act along the upper and lower portions of the particles. This effect would be more pronounced in regions with higher shear rates, where the upper and lower portions of the particles can

experience stronger stress differences, which is what we observe. Finally, just as in the case of the single rolling sphere, the stress balance does close for both simulations when the entire domain is included within the control volume.

The x-momentum balance results for run Re17 (not presented for brevity) are both qualitatively and quantitatively very similar to those for run Re33, given our scaling. We might expect this result, given the similarities in their velocity profiles (Figure 7.12), but it is also a little surprising because Re33 is not in a steady-state configuration. The major differences between steady and unsteady beds, however, lie in the y-momentum balance.

Stress balance of the fluid phase in the y-direction

We similarly apply the time-averaging operator, (7.1), to the y-momentum balances of the fluid phase, (7.14), and the particle phase, (7.22). Figure 7.16 shows the stress balance of the fluid phase for runs Re8 (left side) and Re33 (right side). Figures 7.16a and 7.16b show the balance between the total stress, composed of the fluid and particle stresses, and the external stress, which represents the stress at the upper wall since we do not impose a body force on the fluid in the y-direction. Once again, the total stress is in balance with the external stress, even for the unsteady simulation, Re33. Similar to the results for the single sphere, the particle stress quickly takes up the stress from the fluid within the particle bed ($y/y_{ref} < 2.3$). However, the stresses for run Re8 (Figure 7.16a) are positive while those for run Re33 (Figure 7.16b) are negative, which stem from the transient dilation and contraction of the respective beds, as explained with the next subfigures.

Figures 7.16c and 7.16d show the terms in (7.14) that contribute to the fluid stress. Different from the simulation from the single sphere, the convective term is negligible for these simulations, so that only the pressure term plays a role. Recall that the stresses and

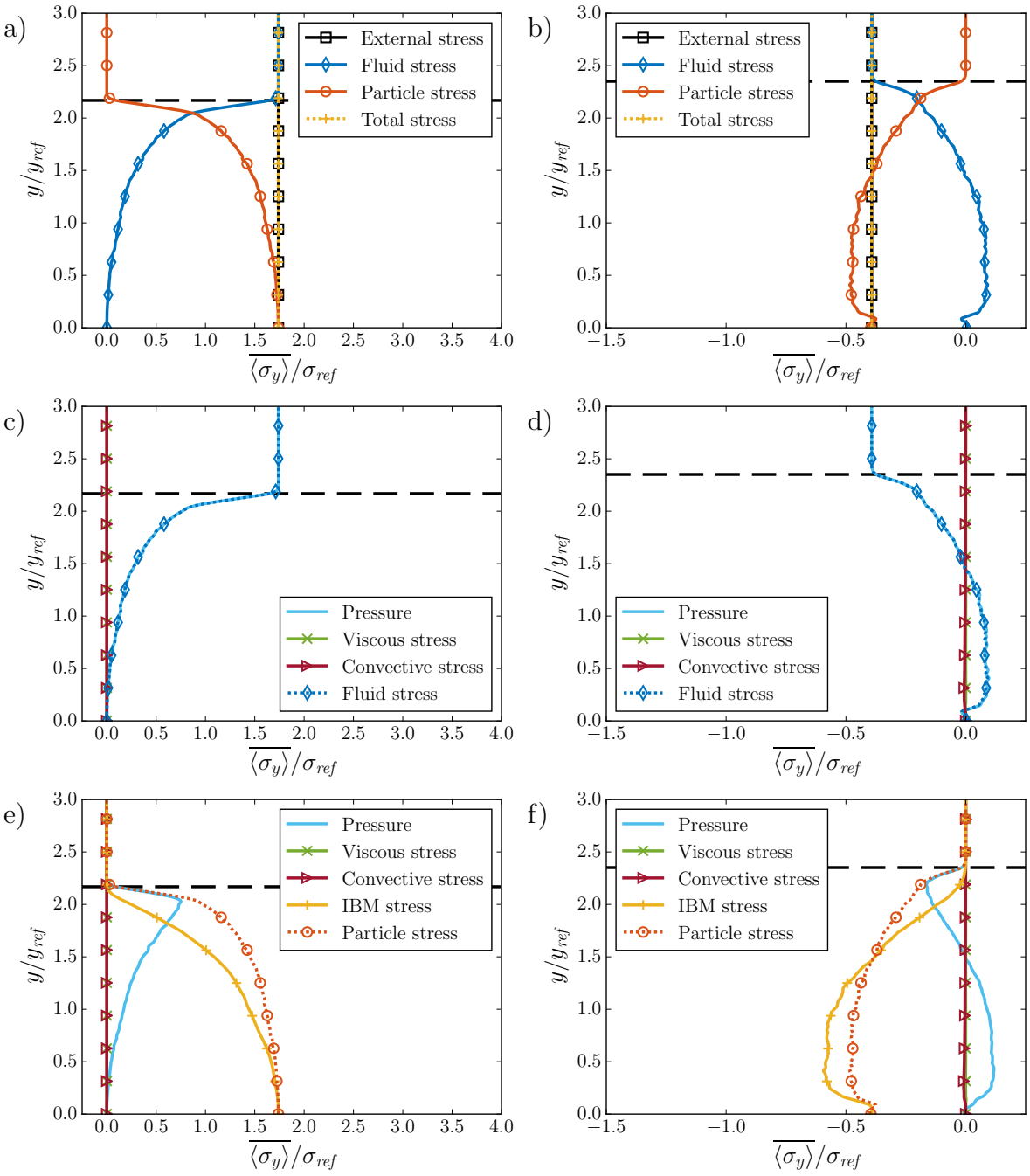

Figure 7.16: Particle bed stress balance of the fluid phase in the y-direction according to (7.14). Subfigures (a), (c), and (e) correspond to run Re8 while (b), (d), and (f) correspond to run Re33. The total stress is the sum of the fluid and particle stresses. The components of (a) and (b) are further broken down in (c) and (d) for the fluid stress and in (e) and (f) for the particle stress. Note that "pressure" refers to the pressure term in (7.14), which is the negative pressure. The horizontal dashed line marks the height of the particle bed, h_p.

pressures in these figures correspond to the negative value of the pressure, according to (7.14). Thus, simulation Re8 has a negative fluid pressure above the particle bed, while run Re33 has a positive fluid pressure above the bed. This observation is consistent with Figure 7.10, which revealed that the fluid pressure (relative to the lower wall) is positive above dilating beds (e.g. Re33) and negative above contracting beds (e.g. Re8). However, another interesting feature in Figure 7.16d is that, while the fluid pressure is positive above the bed, it is negative within the lower portion of the bed ($y/y_{ref} < 1.5$). This may be due to the unsteady nature of the flow.

Figures 7.16e and 7.16f show the terms in (7.14) that contribute to the particle stress. Again, the convective terms do not contribute to the particle stress like they did for the single rolling sphere, meaning only the pressure and IBM terms play a significant role. The pressure terms for the particle and fluid stresses behave similarly, and are important at the fluid/bed interface. Thus, only accounting for the IBM term can lead to an incorrect evaluation of the particle stress.

Stress balance of the particle phase in the y-direction

Figure 7.17 shows the coarse-grained particle phase stresses, given by the time average of (7.22) for runs Re8 (left side) and Re33 (right side). In Figures 7.17a and 7.17b, the bed weight increases almost linearly from the top of the particle bed down to the lower wall, balanced by the total stress, which is the sum of the hydrodynamic and collision stresses. In contrast to the x-momentum particle phase results, the y-momentum results show clear differences between runs Re8 and Re33. First, the hydrodynamic stress is positive for Re8 and negative for Re33, so that the collision stresses are less than and greater than the bed weight, respectively, for the stress balance to be in equilibrium. This difference is directly related to the pressure and steady-state differences discussed previously. Second, σ_{ref} does not collapse the stresses for Re8 and Re33 into similar

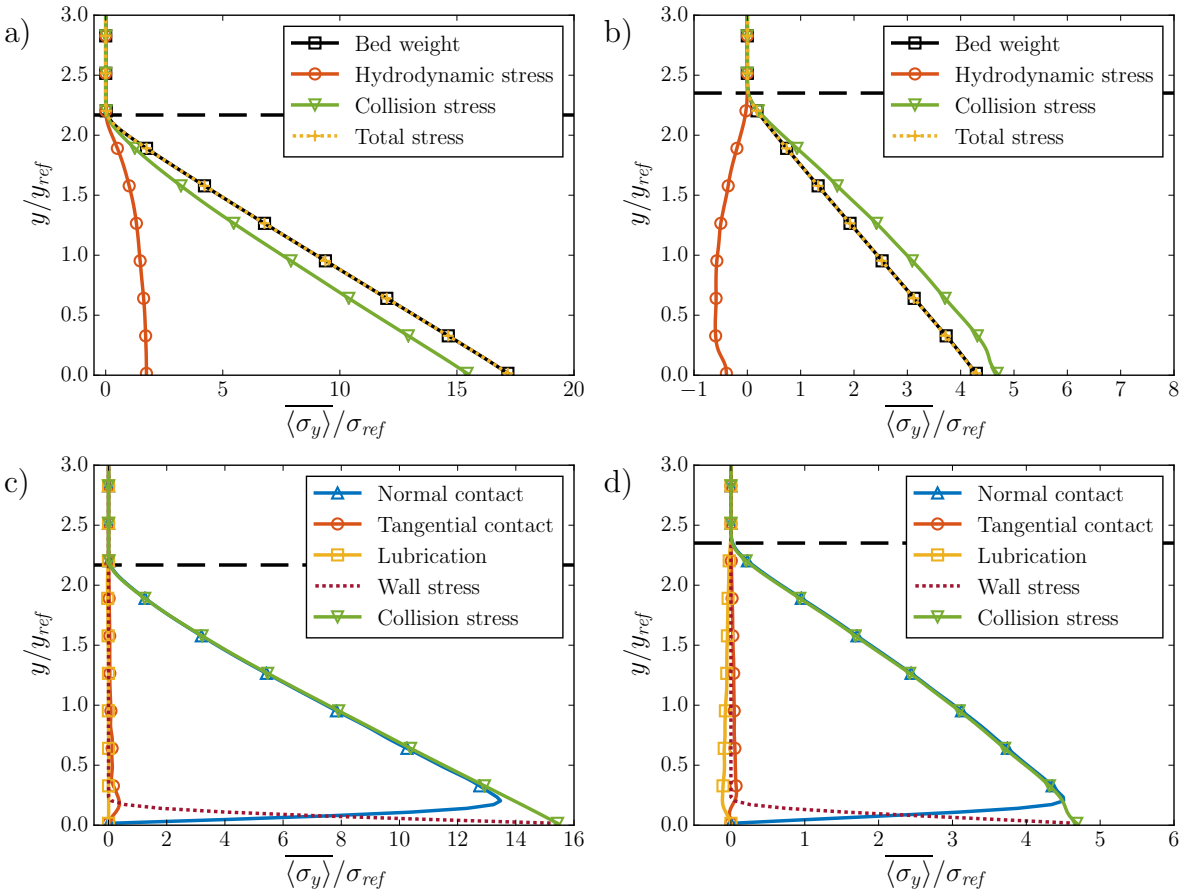

Figure 7.17: Particle bed stress balance of the particle phase in the y-direction according to (7.22). Subfigures (a) and (c) correspond to run Re8 while (b) and (d) correspond to run Re33. The total stress is the sum of the hydrodynamic and collision stresses. The components of the collision stresses in (a) and (b) are further broken down in (c) and (d) according to (7.18). The horizontal dashed line marks the height of the particle bed, h_p.

ranges. In our simulations, the bed weight is approximately the same for the two runs, but σ_{ref} is larger for Re33, resulting in a smaller scaled bed weight for Re33. Therefore, it should be easier for collision stresses to overcome the bed weight in run Re33 than in run Re8.

Figures 7.17c and 7.17d show the terms in (7.18) that contribute to the collision stresses for runs Re8 and Re33, respectively. In both simulations, the collision stress is almost completely a result of normal contacts, which contrasts with the collision stresses in the x-direction, which also had significant contributions from tangential contacts and lubrication. Tangential contacts contribute slightly to support the bed weight near the lower wall for run Re8 (Figure 7.17c) and throughout the bed for run Re33 (Figure 7.17d). A slight negative lubrication force is present throughout the Re33 bed, indicating a net motion of particles away from each other in the y-direction due to the fact that the lubrication force is dissipative and proportional to the relative velocity between particles. This observation is consistent with a dilating particle bed, where the space between particles increases.

From Figures 7.14 and 7.17, we have seen that the normal contact forces play a dominant role in both the x- and y-momentum balances for the particles, but these forces are coupled by the geometry of the particle bed. For instance, two particles colliding have a single normal contact force between them, but the relative force directed in the x-direction or y-direction depends on where the point of contact occurs in the coordinate system. In these simulations, the particle phase is driven in the x-direction by the pressure gradient and hydrodynamic forces. At equilibrium, collisions balance the driving force, and by geometry also provide a particle pressure in the y-direction opposing the weight of the bed. A collision stress larger than the bed weight, as seen for Re33 in Figure 7.17b, then causes the particle bed to dilate upwards. However, as seen in the same figure, the hydrodynamic stress balances the excess collision stress, keeping the

system in equilibrium and slowing the rate of dilation. Thus, the negative hydrodynamic stress for the particle phase, or negative pressure measured at the top wall for the fluid phase, indicates that a particle bed is still dilating in order to attain a collision geometry that allows collision stresses to balance in both x- and y-directions.

7.5 Conclusions

We have derived a momentum balance for particle-resolved IBM simulations in order to understand the stresses governing the motion of sheared particle beds. This balance differs from others in that it fully accounts for the particle stress using the fluid contained within the particles. We then validated the method against a simulation of a single rolling sphere, showing that it works for situations that do not have a statistically significant assemblage of particles. From this simulation, we found that the momentum balances for the fluid phase, (7.12) and (7.14), and the particle phase, (7.21) and (7.22), are valid for instantaneous flow fields at a steady-state relative to the particle. We have also shown that these momentum balances are valid on a particle-resolved scale in which the control volumes cut through a particle that is large relative to the total domain size. In contrast, the methods of Zhang and Prosperetti [108] and Vowinckel et al. [110] require control volumes that enclose many particles, functioning under a statistical-averaging framework. From these momentum balances, we determined that the collision between the particle and the wall played a large role in the flow, with friction slowing the flow from the reference Poiseuille case and with normal contact supporting the particle's weight. We also explored the significance of the various terms comprising the fluid phase balance, (7.12) and (7.14), which allowed us to simplify them into (7.25) and (7.26). Finally, we investigated the momentum balance for a fluid-particle mixture, given by (7.23), and found that it did not close because coarse-grained particle quantities cannot resolve

changes in stress along the particle surface.

We applied time averages to the momentum balances for the fluid phase, (7.12) and (7.14), and the particle phase, (7.21) and (7.22), finding that they close for simulations involving flows with many particles, even those that did not attain a statistical steady state. A reference case, a Poiseuille flow in the upper third of the domain where no particle are present initially, provided a reasonable scaling of the velocities and stresses in the x-direction, even when the entire particle bed was in motion.

We also investigated the terms comprising (7.12) and (7.14) for the simulations of the particle beds, finding only the viscous term to be important for the x-momentum fluid stress, only the IBM term to be important for the x-momentum particle stress, only the pressure term to be important for the y-momentum fluid stress, and both the pressure and IBM terms to be important for the y-momentum particle stress. Therefore, the simplified expressions from the single particle balance, (7.25) and (7.26), would be equally valid for these simulations, and could even be further simplified to exclude the viscous terms from the particle stress and the convective terms from the fluid and particle stresses. Furthermore, simulations involving similar flow conditions would be justified in using only the IBM term to calculate the x-momentum stress, as was done in Kidanemariam and Uhlmann [112] and Vowinckel et al. [109, 110]. In our experience, the viscous term contributes to the particle stress only for much more viscous flows. However, the pressure term must be included in the particle stress in the y-direction.

We also investigated the terms comprising the collision force, given by (7.18). For the flow conditions for the present simulations, the normal contact force dominates the x-momentum collision force and is nearly solely responsible for the y-momentum collision force. Lubrication and tangential contact forces contribute similarly small amounts to the collision forces in the x-direction.

With our scaling based on the reference Poiseuille flow, the x-momentum balances

were very similar qualitatively and quantitatively for the various flows over a particle bed, even though one of the simulations was in a transient state. We found that the y-momentum balances were crucial in revealing transient behavior of the particle beds. The fluid pressure at the top wall relative to the bottom wall (neglecting hydrostatics) indicated whether the bed was dilating (positive pressure) or contracting (negative pressure). Analyzing the forces on the particles within the bed also revealed fluid forces acting to oppose the upward motion of the particles in a dilating bed.

We also applied the x-momentum balance of the fluid/particle mixture, (7.23), to the sheared bed of particles. As with the case for the single sphere, we found that this balance does not close unless the entire domain is considered, but we did find that the gap in the closure is related to the local shear rate: higher shear rates led to larger gaps. Further studies should be carried to understand this dependence, which may allow for a closure of the mixture stress balance. It would then prove a powerful tool for measuring the stresses in dense particle-laden flows.

Another extension of this work would be to include the time-dependent terms. The real power in the accurate measurement of particle-fluid stresses would be to analyze unsteady flows on short time scales. This could, for instance, allow us to study the rheology of transient particle-laden flows, such as the onset or cessation of erosion. Finally, extending the time-averaged equations for use with turbulent flows would permit its use for a broad range of important sediment transport problems.

Chapter 8

Rheology of a sheared particle bed

8.1 Introduction

Having developed all the tools necessary to simulate flows over dense sediment beds and measure the stresses in the fluid and particle phases, we can now analyze the rheology of these flows. Rheological descriptions of particle-laden flows began with a dilute-regime asymptotic expansion by Einstein [113], which was further developed by Batchelor [114, 115]. However, theoretical frameworks do not work at higher particle concentrations unless the particle motions are extremely energetic, at which point kinetic theory can be applied [116, 14, 117]. Meanwhile, for flows involving high particle concentrations at low granular temperatures, researchers have relied on empirical fits to experimental data. Popular works include those of Eilers [118], Mooney [119], Krieger and Dougherty [120], and, more recently, Morris and Boulay [121]. These studies developed rheological models that specify an effective viscosity of the fluid/particle mixture, η_s, which depends on the particle concentration.

The granular community, on the other hand, developed a separate framework to describe granular flows (without fluid). The macroscopic friction coefficient, or $\mu(I)$

rheology, relates the shear stress to the nondimensional inertia number I, which relates the particle inertia to the confining pressure. This friction coefficient is different from the values μ_k and μ_s used for particle-particle contacts. Indeed, frictionless particles as a bulk medium can exhibit macroscopic friction due to normal contacts [122]. This framework achieved great success in describing the bulk behavior for different types of 3-D granular flows [123], and has even been successful when coupled with constitutive models for predicting granular flows down an incline [124]. However, this framework has not been able to describe all types of granular flow geometries [125].

Cassar et al. [126] began to apply the macroscopic friction concept to particle-laden flows with their study of submarine granular flows down inclined planes, which they related to dry granular flows down inclined planes. Dijksman et al. [18] investigated this approach for a "split-bottom" rheometer. Later, Boyer et al. [22] unified this framework with the effective viscosity, developing a rheological model that worked in both situations for their experimental data. DeGiuli et al. [24] have worked to unify the description of the macroscopic friction coefficient for submerged and dry granular flows.

Ideally, we should be able to use established particle/fluid mixture rheologies to predict particle-laden flow velocities and mass fluxes. Aussillous et al. [19] attempted to match the velocity profiles from their experiments with those from constitutive models, achieving only mixed success. We have been unsuccessful in our own attempts to predict our simulation flow profiles using constitutive models, so we have taken a step back to look more closely at the rheological models upon which the constitutive models heavily rely. Some fundamental questions still need to be answered before we can understand why the constitutive models currently do not work well as predictive tools. Most of these rheological models were developed using Couette flow experiments involving the shearing of neutrally-buoyant particles over a gap size of at least 10 particle diameters. Therefore, it is not clear if these models are applicable to our situation, which involves heavy

particles whose granular pressure varies with the bed depth. Nor is it clear if the models are applicable in a local sense, describing the flow everywhere instead of as a whole, or in situations where the shear rate varies on the scale of a particle diameter. Some researchers have begun to investigate these questions using heavy particles and measuring the local rheology. Maurin et al. [5] found their simulations to match the model of Boyer et al. [22], but they investigated a turbulent regime and did not fully resolve the particle-fluid interactions. Houssais et al. [20] found their laminar Couette flow experiments to match the Boyer et al. model, but they investigated creeping motion of the particle beds at very large time scales. In this chapter, we will provide our own contributions to the community for laminar flows using phase-resolved simulations. First we will describe the rheological frameworks in more detail and briefly discuss existing rheology models. Then we will calculate the local rheology from our own simulations of a pressure-driven over a particle bed and compare our results to the models and experiments.

8.2 Description of rheology

8.2.1 Effective viscosity vs. $\mu(I)$

Researchers have described particle/fluid mixtures within two different frameworks. The first, used by Morris and Boulay [121], describes the mixture shear stress, τ, using an effective shear viscosity, η_s:

$$\tau = \eta_s(\phi)\eta_f\dot{\gamma}, \tag{8.1}$$

where η_f is the fluid viscosity and $\dot{\gamma}$ is the shear rate. These authors also describe the particle pressure, p_p, using an effective normal viscosity, η_n:

$$p_p = \eta_n(\phi)\eta_f\dot{\gamma}. \tag{8.2}$$

These relationships assume that the effective viscosity depends only on the local volume fraction of particles, ϕ, and have been written here assuming a one-dimensional flow. In general, the mixture stress tensor, $\mathbf{\Pi}$, is given by

$$\mathbf{\Pi} = -p\mathbf{I} + 2\eta_f\dot{\boldsymbol{\gamma}} + \mathbf{\Pi}_p, \tag{8.3}$$

where p is the isotropic fluid pressure, $\mathbf{I}$ the identity tensor, $\dot{\boldsymbol{\gamma}} = \frac{1}{2}(\nabla\mathbf{u} + (\nabla\mathbf{u}^T))$ the shear rate tensor, and $\mathbf{\Pi}_p$ the stress tensor contributed by the particles [21]. The particle pressure is given by $p_p = -\frac{1}{3}\text{tr}(\mathbf{\Pi}_p)$, though in practice, it is often measured as $p_p = \Pi_{22}$. For simple shear flows, we can establish that $\tau = \Pi_{12}$. We can then obtain (8.1) from (8.3) by letting $\eta_s = 1 + \eta_{s,p}$ and assuming that $\Pi_{p,12} = \eta_{s,p}\eta_f\dot{\gamma}$.

On the other hand, Boyer et al. [22] and Aussillous et al. [19] used the $\mu(I)$ framework, which relates the shear stress,

$$\tau = \mu(I_v)p_p, \tag{8.4}$$

to the particle pressure, p_p, where μ is a macroscopic friction coefficient describing the fluid/particle mixture. The other constitutive relationship is for the particle volume fraction,

$$\phi = \phi(I_v). \tag{8.5}$$

These two relationships state that the friction coefficient and particle volume fraction are functions of the viscous inertia number

$$I_v = \frac{\eta_f\dot{\gamma}}{p_p}, \tag{8.6}$$

which is a dimensionless number relating the viscous shear stress, which causes the particles to slide past one another in uniform rows, to the particle pressure, which locks

the particles into tighter packing fractions. For large inertia numbers, particles follow ballistic trajectories, whereas for small inertia numbers, particles tend to maintain static contacts with their neighbors. This framework originated in the granular community, where the absence of an interstitial fluid leads to the use of the granular inertia number,

$$I = \frac{\dot{\gamma} D_p}{\sqrt{\rho_p p_p}}. \tag{8.7}$$

Cassar et al. [126] and Trulsson et al. [127] describe that the transition from the granular to the viscous inertia number depends on the Stokes number $St = \rho_p \dot{\gamma} D_p^2 / \eta_f$, where a high Stokes number corresponds to a granular regime. Trulsson et al. [127] found that particle collisions account for the stresses in the granular regime, whereas viscous forces account for the stresses in the viscous regime. As shown from the x-momentum stress balances in the previous chapter, our simulations reside in the viscous regime.

Boyer et al. [22] explained the equivalence of the two frameworks. To show this, we can rewrite (8.4) and (8.6) as

$$\tau = \frac{\mu(I_v(\phi))}{I_v(\phi)} \eta_f \dot{\gamma} \tag{8.8}$$

and

$$p_p = \frac{1}{I_v(\phi)} \eta_f \dot{\gamma}. \tag{8.9}$$

Thus, in terms of the effective viscosity,

$$\eta_s(\phi) = \frac{\mu(I_v(\phi))}{I_v(\phi)} \tag{8.10}$$

and

$$\eta_n(\phi) = \frac{1}{I_v(\phi)}. \tag{8.11}$$

Though an equivalence exists, it is not always straightforward to transfer models from one framework to the other. In the next section, we present a few existing models.

8.2.2 Rheology models

Many authors have developed rheological models based on a few theoretical principles with empirical constants to fit experimental data [118, 120, 128, 121, 22]. The general idea is that $\eta_s \to 1$ as $\phi \to 0$ and $\eta_s \to \infty$ as $\phi \to \phi_m$, where ϕ_m is the maximum packing fraction at which point the particles become locked in a structure that does not allow them to slide over one another. In practice, various authors have used the maximum packing fraction as another parameter to be tuned. Boyer et al. [22] found $\phi_m = 0.585$ to be the maximum volume fraction at which their suspensions could be sheared. Morris and Boulay [121], on the other hand, use $\phi_m = 0.63$ generally based on the random close packing fraction, but adjust their model to use $\phi_m = 0.68$ to match the experiments of Phillips et al. [129]. Stickel and Powell [21] explain that ϕ_m can even be expressed as a function of the shear rate, allowing for a model that depends both on the shear rate and on the volume fraction. Recent work with dense suspensions suggests that the maximum packing fraction decreases with increasing strength of frictional contacts between particles, which can result from rougher particles or higher particle pressures [25].

At the dilute limit ($\phi \to 0$), some researchers have developed analytical solutions. Einstein [113] derived a first-order approximation with

$$\eta_s = 1 + [\eta]\phi + \mathcal{O}(\phi^2), \tag{8.12}$$

where $[\eta] = \frac{5}{2}$ for hard spheres. Batchelor [114, 115] extended this to second order with

$$\eta_s = 1 + [\eta]\phi + B\phi^2 + \mathcal{O}(\phi^3), \tag{8.13}$$

where $B = 6.2$ for any Brownian suspension and $B = 7.6$ for non-Brownian suspensions in a pure straining flow. Other models generally try to obtain the behavior of (8.12) at the dilute limit. One such model is that of Krieger and Dougherty [120]:

$$\eta_s = \left(1 - \frac{\phi}{\phi_m}\right)^{-[\eta]\phi_m}. \tag{8.14}$$

Another is that of Morris and Boulay [121]:

$$\eta_s = 1 + \frac{5}{2}\phi_m \left(1 - \frac{\phi}{\phi_m}\right)^{-1} + K_s \left(\frac{\phi}{\phi_m - \phi}\right)^2 \tag{8.15}$$

$$\eta_n = K_n \left(\frac{\phi}{\phi_m - \phi}\right)^2, \tag{8.16}$$

where the values $K_s = 0.1$ and $K_n = 0.75$ were obtained from wide-gap Couette flow data.

Boyer et al. [22] derived their models for the $\mu(I_v)$ rheology:

$$\mu(I_v) = \mu_1 + \frac{\mu_2 - \mu_1}{1 + I_0/I_v} + I_v + \frac{5}{2}\phi_m I_v^{1/2} \tag{8.17}$$

$$\phi(I_v) = \frac{\phi_m}{1 + I_v^{1/2}}, \tag{8.18}$$

where $\mu_1 = 0.32$, $\mu_2 = 0.7$, $I_0 = 0.005$, and $\phi_m = 0.585$ are empirical values obtained from their shear flow data. This model can readily be transferred to an effective viscosity framework:

$$\eta_s = 1 + \frac{5}{2}\phi \left(1 - \frac{\phi}{\phi_m}\right)^{-1} + \mu^c(\phi) \left(\frac{\phi}{\phi_m - \phi}\right)^2 \tag{8.19}$$

$$\eta_n = \left(\frac{\phi}{\phi_m - \phi}\right)^2, \tag{8.20}$$

where

$$\mu^c(\phi) = \mu_1 + \frac{\mu_2 - \mu_1}{1 + I_0\phi^2(\phi_m - \phi)^{-2}}. \tag{8.21}$$

Notice how this model bears a strong resemblance to that of Morris and Boulay [121]. Next, we will compare the simulation results to these models.

8.3 Results

The simulations from the previous chapter involving flow over a sediment bed provide good cases for studying the rheology because we have already analyzed their stresses. In particular, we will investigate the rheology of runs Re8, Re17, and Re33, which are described in Section 7.2.2. Recall that runs Re8 and Re17 are at steady state and that the beds in runs Re17 and Re33 are fully-mobilized. Thus, these simulations represent different flow configurations. In the following sections, we will show our rheological measurements of these simulations under the two frameworks.

8.3.1 Effective viscosity

First, we will look at the effective viscosity of the particle beds. From the stress balance in Section 7.4.2, we have shown that the shear stress at a given y-coordinate is

$$\tau = \overline{\langle \tau_w \rangle} + f_{b,x}(L_y - y), \tag{8.22}$$

where τ_w is the shear stress at the top wall. We have also shown that the bed weight is in equilibrium with the collision and hydrodynamic stresses, giving us

$$p_p = -(\rho_p - \rho_f)\mathbf{g} \int_y^{L_y} \overline{\langle \phi \rangle}\, \mathrm{d}y. \tag{8.23}$$

Using these relationships together with the local shear rate obtained from the fluid velocity profiles (Figure 7.12) and the relationships (8.1) and (8.2), we can evaluate the local effective shear and normal viscosities for each y-coordinate, shown in Figures 8.1 and 8.2, respectively. For each simulation, we obtain a range of effective viscosities and volume fractions, with the lower viscosities and volume fractions corresponding to the particle data near the top of the bed, and the higher viscosities and volume fractions corresponding to the data deeper in the bed near the lower wall. We evaluated the volume fractions using the method described in Section 6.4 in order to produce smoother results. These plots also include experimental data from Boyer et al. [22], who used polymethyl methacrylate (PMMA) spheres and polystyrene (PS) spheres, and Dagois-Bohy et al. [130], who used polystyrene spheres. The reported maximum packing fractions are $\phi_m = 0.585$ for the Boyer et al. experiments and $\phi_m = 0.59$ for the Dagois-Bohy et al. experiments. We used a maximum packing fraction of $\phi_m = 0.59$ for all our simulation data based on where our effective viscosities appear to diverge.

In Figure 8.1, the simulation data for the different flow rates collapse onto the same curve for the effective shear viscosity. However, it does not match the curve following the model of Boyer et al. or the experimental data. Instead, the simulation data appears to compare more closely with the model of Morris and Boulay. Interestingly, the data matches very well with the models tending towards low volume fractions, where the effective viscosity is expected to approach $\eta_s = 1$. This is somewhat surprising, given that this range of volume fractions exists only across a height of one or two particle diameters (see Figure 6.6). Therefore, models for the effective shear viscosity do appear to function on small spatial scales relative to the particle size.

Figure 8.2 shows that the simulation data also collapses for the effective normal viscosity as a function of the volume fraction. However, the data again exhibits a systematic shift down from the models and experimental data. Though the measured viscosity is

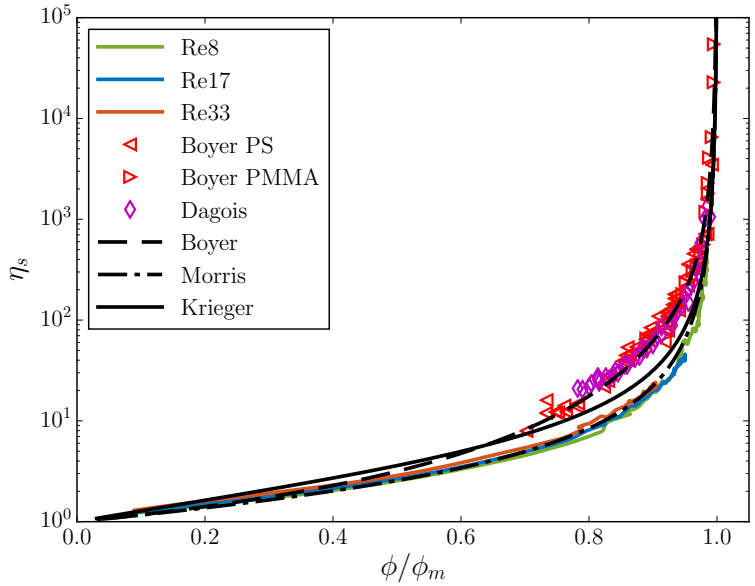

Figure 8.1: Effective shear viscosity evaluated from time-and-space-averaged simulation results. Colored lines represent simulation data, symbols represent experimental data, and black lines represent rheology models.

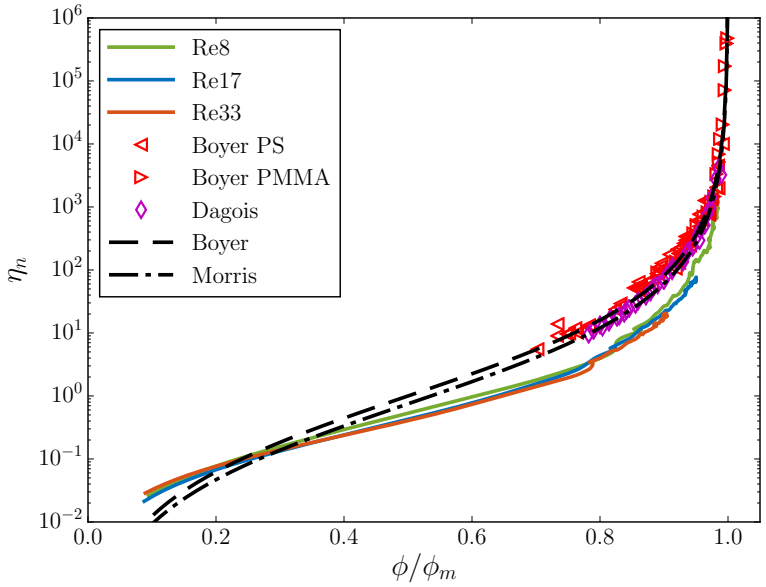

Figure 8.2: Effective normal viscosity evaluated from time-and-space-averaged simulation results. Colored lines represent simulation data, symbols represent experimental data, and black lines represent rheology models.

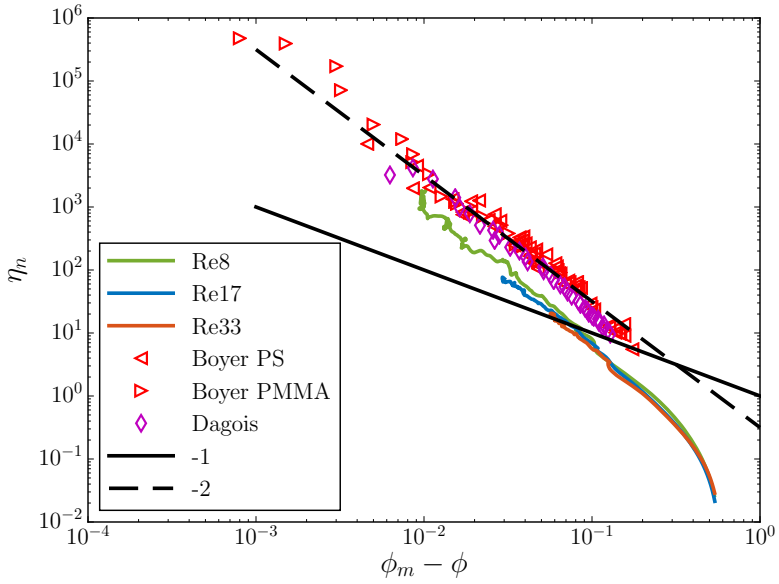

Figure 8.3: Effective normal viscosity evaluated from time-and-space-averaged simulation results. Colored lines represent simulation data, symbols represent experimental data, and black lines represent exponential slopes.

about an order of magnitude lower than the experimental data, the behavior at high volume fractions is similar. To see this more clearly, Figure 8.3 shows the same data with a different scaling of the volume fraction to emphasize the limit as the volume fraction approaches the maximum packing fraction. The offset is again clearly visible, but the scaling between the simulations and experiments is the same, given by the -2 slope, which corresponds to the exponent in (8.20).

At the lower volume fractions the simulation results differ both quantitatively and qualitatively from the models. The models were derived, however, using experimental data at high volume fractions only. Notice that experimental data only exists for $\phi/\phi_m > 0.7$. Thus, we cannot expect the models to behave well in this regime.

We do not know what causes the difference between the simulation data and experiments/models. One possibility is that the rheological measurements of the experiments are not valid for describing the local rheology of our simulations. Another possibility is

that the experimental data for neutrally-buoyant spheres is not applicable to situations involving heavy particles, though Maurin et al.[5] and Houssais et al. [20] found otherwise. However, these other works were in different regimes, the former in a turbulent flow and the latter using lighter particles ($\rho_p/\rho_f = 1.13$) at much longer time scales, so the question remains open for further exploration.

8.3.2 $\mu(I)$ rheology

We can alternatively look at the results in terms of the macroscopic friction coefficient framework, or $\mu(I)$ rheology. Using quantities measured from the simulations together with (8.4) and (8.6), we obtain Figures 8.4 and 8.5, where, again, each point represents time-and-space-averaged data from one y-coordinate of a simulation. In Figure 8.4, we do not see the same collapse of the data as we did for the effective viscosities, but the range of scatter is comparable to the scatter in the experiments. Indeed, the experiments of Dagois-Bohy et al. [130] differ quite a bit from the PS experiments of Boyer et al. [22], which were conducted with the same experimental configuration.

The inertia numbers we report here do extend to rather large values ($I_v > 1$), but these result from the low particle pressure, p_p, which scales inversely with I_v, near the top of the particle bed. This good match at high viscous inertia numbers is consistent with the good match of the effective shear viscosity at low volume fractions, since the models in both cases emulate the Einstein effective viscosity. We did not have to use an offset pressure P_0, as suggested by Houssais et al. [20], to obtain this collapse at high inertia numbers. We do see, however, that simulation Re8 asymptote towards a static friction coefficient $\mu_s = 0.3$ as $I_v \to 0$, which is similar to the value $\mu_s = 0.32$ measured in the experiments of Boyer et al. [22]. However, Maurin et al.[5] report that μ_s can vary depending on parameters such as the particle specific density or the flow Shields number

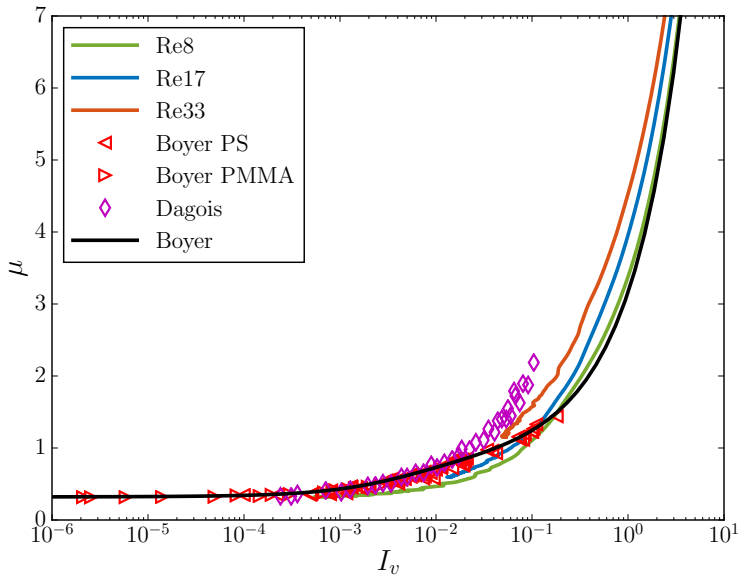

Figure 8.4: Friction coefficient evaluated from time-and-space-averaged simulation results. Colored lines represent simulation data, symbols represent experimental data, and black lines represent rheology models.

and that low inertia number conditions can exhibit particle creep, which is a non-local phenomenon. Houssais et al. [20] also observed creep, resulting in a $\mu(I_v)$ plot that did not converge to a constant value at low I_v, but they were able to take measurements to observe creep on a time scale much larger than that of the present simulations.

Figure 8.5, which shows the dependence of the volume fraction on the inertia number, once again shows a collapse of the simulation data to the same curve. Consistent with the results for the normal effective viscosity results, there is an offset between the simulation and experimental data, though the qualitative behavior is similar. Houssais et al. [20] experienced a poor comparison of their results to the $\phi(I_v)$ model of Boyer et al., but their data for this plot did not collapse the way that ours did. Again, the model does not represent the qualitative behavior at high inertia numbers (low volume fractions).

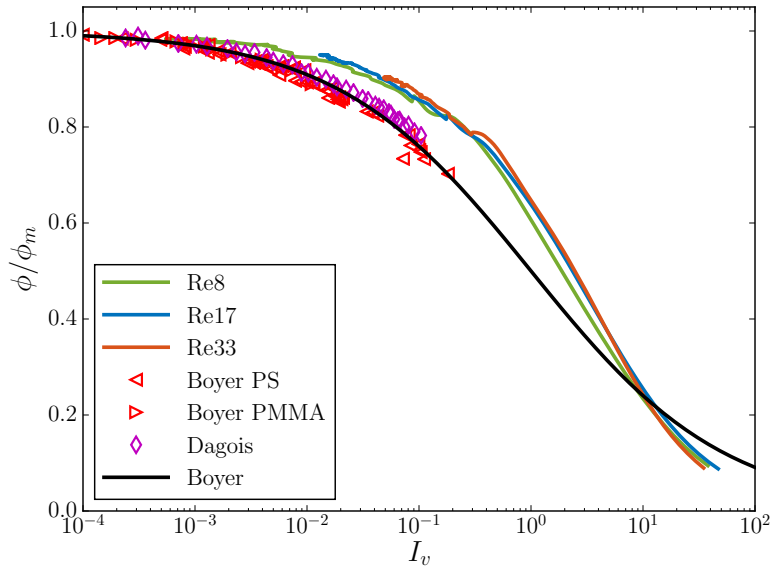

Figure 8.5: Volume fraction evaluated from time-and-space-averaged simulation results. Colored lines represent simulation data, symbols represent experimental data, and black lines represent rheology models.

8.4 Conclusions

Having examined the particle bed stresses in Chapter 7, we examined the rheology of the fluid-particle mixture. Despite difference flow conditions, the data for the different flows rates collapsed when observing the $\eta_s(\phi)$, $\eta_n(\phi)$, $\mu(I_v)$, and $\phi(I_v)$ relationships. There was, however, a systematic offset between our simulation results and the models/experiments. On the other hand, the simulation results did compare reasonably well to the effective shear viscosity proposed by Morris and Boulay [121], and to the $\mu(I_v)$ rheology of Boyer et al. [22]. The shear viscosity and friction coefficient of the simulations also behaved well near the fluid/bed interface where the particle volume fraction was low. The simulation results also exhibited the same qualitative behavior as the models for the $\eta_n(\phi)$ and $\phi(I_v)$ relationships at high volume fractions.

It is still not clear if the rheological measurements from Couette flows with neutrally-

buoyant spheres are applicable to our situations involving pressure-driven flows over sediment beds. Relationships for $\eta_s(\phi)$ and $\mu(I_v)$ appear to compare much better than those for $\eta_n(\phi)$ and $\phi(I_v)$. In fact, models for the latter relationships still require development to accurately handle low particle volume fractions. One advantage of the methods we use, however, is that they can easily be implemented to analyze, for instance, the experimental data of Aussillous et al. [19]. Such investigations could provide further insight into a rheological description of sediment beds, which could ultimately result in better predictive models.

Chapter 9

Outlook

Our goal was to make progress towards understanding flows interacting with sediment beds. To that end, we developed PARTIES, a DNS code that employs the IBM to resolve the flow around individual particles. Having validated the fluid-particle coupling against settling sphere experiments, we developed and validated a collision model to accurately simulate immersed particle-wall collisions while also accounting for situations involving a bed of particles. Next, we demonstrated the code's ability to reproduce experiments of a pressure-driven flow over a sediment bed. Using this same setup, we then established the tools necessary to analyze the flow in detail: the coarse-graining method for representing particles as a continuum and the momentum balance for measuring stresses. Finally, we applied these methods to measure the rheology of these sediment bed flows.

The momentum balance gave us a first glimpse at the mechanisms governing the time-evolution of a bed of particles. Imbalances between collision forces and the bed weight led to the bed dilating or contracting, but we still cannot *a priori* determine the equilibrium bed height. Instead, we only measured whether or not the system was in equilibrium. We hypothesized that changing the collisional geometry, i.e. the angles at which collisions occur, of the bed allows the system to reach equilibrium, but to test

and quantify this hypothesis we would need to implement other methods, such as a pair-distribution function to measure the probabilities of particles colliding at different angles.

We also found that the rheological measurements for three simulations with qualitatively-different velocity profiles collapsed onto the same curve. Thus, a rheology model might be able to provide some insight into what causes the velocity profiles to change from concave to linear to convex. The mismatch between our simulation rheology and experimental rheology requires further investigation. However, our approach to measuring the rheology can be easily applied to experimental data, which could lead to more insightful comparisons.

The phase-resolved momentum balance also revealed that fluid-particle hydrodynamic interactions are most important at the interface between the particle bed and the clear fluid layer above. Within the bed, particle-particle interactions largely govern the flow. Thus, we could try to develop a hybrid simulation method that uses the IBM only at the fluid/bed interface and relies on particle-particle interactions alone within the particle bed. Such a method could significantly increase the efficiency of the simulations, whose computational cost arises largely from the IBM.

PARTIES is also not limited to studying flows over sediment beds, but can also be applied to a wide range of problems that require careful treatment of flows around particles on a small scale. Furthermore, our group has already begun implementing additional methodologies to PARTIES, allowing it to simulate cohesive suspensions, active swimmers, and interactions between particles and passive scalar fields, such as temperature or salinity. Thus, we will be able to study a plethora of environmental, biological, and industrial particle-laden flows.

Appendix A

Nomenclature

Roman Symbols

D_p	diameter of particle p
d_n	normal contact damping coefficient
d_t	tangential contact damping coefficient
e_{dry}	coefficient of restitution for dry contact
$\mathbf{F}$	force acting on a particle's center of mass
$\mathbf{F}_l$	IBM force acting on Lagrangian marker l
$\mathbf{F}_{b,p}$	net body force acting on particle p
$\mathbf{F}_{c,p}$	net collision force acting on particle p
$\mathbf{F}_{f,p}$	net fluid force acting on particle p (hydrodynamic plus body force)
$\mathbf{F}_{g,p}$	net buoyancy force acting on particle p
$\mathbf{F}_{h,p}$	net hydrodynamic force acting on particle p
$\mathbf{F}_{IBM,p}$	net IBM force acting on particle p
$\mathbf{F}_{r,p}$	net rigid body force acting on particle p
$\mathbf{f}_b$	body force acting on fluid and particles (pressure gradient)
$\mathbf{f}_{IBM}$	IBM force acting on fluid
$\mathbf{g}$	gravity; relative velocity in a collision
h	grid spacing
h^{cg}	grid spacing for coarse-graining method
h_f	height of fluid layer above particle bed
h_m	height of layer of moving particles within the bed
h_p	height of particle bed
I	inertia number
$\mathbf{I}$	identity tensor
I_p	moment of inertia of particle p
I_v	viscous inertia number

Roman Symbols

k_n	normal contact stiffness
k_t	tangential contact stiffness
L_x	domain length in the x-direction
L_y	domain length in the y-direction
L_z	domain length in the z-direction
m_p	mass of particle p
N_l	number of Lagrangian markers for particle p
N_p	number of particles
$\mathbf{n}$	normal vector
p	fluid pressure (without hydrostatic pressure)
p_p	particle pressure
q_f	fluid flux per unit width
q_p	particle flux per unit width
q_v	velocity flux per unit width
R_p	radius of particle p
$\mathbf{r}$	position vector
$\mathbf{T}$	torque acting on a particle's center of mass
T_c	duration of collision
$\mathbf{T}_{c,p}$	net collision torque acting on particle p
$\mathbf{T}_{f,p}$	net fluid torque acting on particle p (hydrodynamic torque)
$\mathbf{T}_{h,p}$	net hydrodynamic torque acting on particle p
$\mathbf{T}_{IBM,p}$	net IBM torque acting on particle p
$\mathbf{T}_{r,p}$	net rigid body torque acting on particle p
t	time
$\mathbf{t}$	tangent vector
$\mathbf{U}_l$	fluid velocity at Lagrangian marker l
$\mathbf{U}_l^d$	rigid body velocity of Lagrangian marker l
u	x-component of fluid velocity
$\mathbf{u}$	fluid velocity
u_{in}	speed of particle before contact
u_{out}	speed of particle after contact
$\mathbf{u}_p$	translational velocity of particle p
V_l	volume of influence of Lagrangian marker l
V_p	volume of particle p
v	y-component of fluid velocity
$\mathcal{W}(\mathbf{r})$	coarse-graining function
w	coarse-graining width
$\mathbf{X}_l$	position of Lagrangian marker l
$\mathbf{x}$	domain coordinate
$\mathbf{x}_p$	position of particle p

Greek Symbols

α_k, γ_k, ζ_k	Runge-Kutta coefficients
γ	fluid volume fraction
$\dot{\gamma}$	shear rate
$\dot{\boldsymbol{\gamma}}$	shear rate tensor
Γ_p	surface domain of particle p
Γ_y	control volume surface at a height y
Γ_w	control volume surface at the upper wall of the domain
Δt	timestep
$\delta(r)$	Dirac delta function
$\delta_h(\mathbf{r})$	3-D interpolation function
$\delta_h^{1D}(r)$	1-D interpolation function
ζ_n	distance between surfaces in a collision
$\boldsymbol{\zeta}_t$	tangential displacement vector
η_f	fluid dynamic viscosity
η_s	effective shear viscosity
η_n	effective normal viscosity
μ	macroscopic friction coefficient
μ_f	fluid dynamic viscosity
μ_s	coefficient of static friction
ν	Poisson's ratio
ν_f	fluid kinematic viscosity
$\boldsymbol{\Pi}$	fluid/particle mixture stress tensor
$\boldsymbol{\Pi}_p$	particle stress tensor
ρ_f	fluid density
ρ_p	particle density
$\boldsymbol{\sigma}$	stress tensor
τ	fluid/particle mixture shear stress
$\boldsymbol{\tau}$	hydrodynamic stress tensor
τ_w	shear stress at the upper wall
ϕ	particle volume fraction; pressure correction variable
ϕ_m	maximum particle packing fraction
φ	level-set function
ψ_{in}	impact angle
ψ_{out}	rebound angle
Ω_p	volume domain of particle p
$\boldsymbol{\omega}_p$	angular velocity of particle p

Other Symbols

$\nabla(\cdot)$	gradient operator
$\nabla \cdot (\cdot)$	divergence operator
$\nabla^2(\cdot)$	Laplace operator
$\lvert \cdot \rvert$	absolute value
$\lvert\lvert \cdot \rvert\rvert$	Euclidian norm
$\langle \cdot \rangle$	averaging operator in the streamwise and spanwise directions
$\overline{\cdot}$	averaging operator in time

Subscripts

cp	property at contact point of two surfaces in a collision
CV	subdomain of the control volume
i, j, k	property at grid cell (i, j, k) of the Eulerian mesh
l	property at Lagrangian marker l of particle p
n	normal
p	property related to particle p
q	property related to particle q
ref	reference variable
t	tangential
x	x-component of a vector
y	y-component of a vector
z	z-component of a vector

Superscripts

$+$	property of the fluid outside particles
$-$	property of the fluid inside particles
cg	coarse-grained quantity
k	Runge-Kutta substep
T	vector/tensor transpose

Abbreviations

ACTM	Adaptive Collision Time Model
DEM	Discrete Element Method
DNS	Direct Numerical Simulation
IBM	Immersed Boundary Method
PARTIES	our code (PARTicle-laden flows via immersed boundarIES)
RHS	right-hand side
RK	Runge-Kutta
RP	repulsive potential

Appendix B

Parallelization of particles

B.1 IBM forcing

When a particle overlaps with a processor boundary, it encounters the problem of extending beyond the reach of the information its host processor possesses. For example, a particle whose center is on a processor boundary has half of its volume on one processor and half on the other. The host processor could evaluate the fluid forces acting on this particle only if it had enough ghost nodes to span the particle radius, which is impractical for most simulations of interest, where the grid resolution has at least 20 grid cells per diameter.

Instead, we implement a strategy in which each processor evaluates the IBM forces for the portion of the particle contained within its domain. Consider the particle shown in Figure B.1, which is owned by Processor 0 yet extends into Processor 1. The Lagrangian markers are indicated by black and gray dots, with two markers highlighted in red, which will be our example markers. The two important operations involving the Lagrangian markers are interpolation of the fluid velocity onto the markers, given by (3.2), and spreading of the Lagrangian forces onto the fluid field, given by (3.4). To minimize the

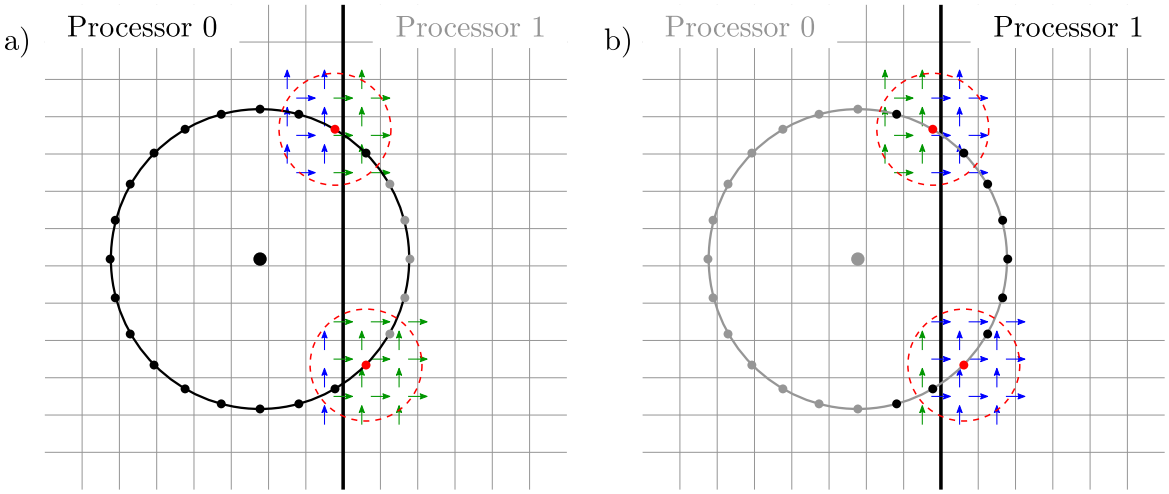

Figure B.1: A particle, owned by Processor 0, crossing the boundary with Processor 1. The interpolation and spreading operations are shown from the viewpoints of (a) Processor 0 and (b) Processor 1. Lagrangian markers that are close enough to influence the local velocity field are colored black, while those that have no effect are colored gray. For two markers colored red, the radius of influence due to the delta function is given by the dashed circles. The cell velocities (horizontal arrows for the u-velocity and vertical arrows for the v-velocity) influenced by the red markers are also shown and colored blue if owned by the local processor and green if ghost cells.

number of ghost nodes and prevent double-counting of forces, we do the following:

1. The interpolation step (3.2) is conducted for all markers that are within "near" the processor, i.e. within the radius of the delta function. These markers are colored black for the respective processors in Figure B.1.

2. Correction forces are calculated for all of these markers according to (3.3).

3. Correction forces are spread back to the Eulerian grid according to (3.4). This spreading only affects the processor's local grid points, indicated by the blue points in Figure B.1.

4. Correction forces are applied to the particle according to (3.5), but only if the marker is contained within the processor's boundaries.

As an example, consider the top red point in Figure B.1, which is contained within Processor 0. According to the method mentioned above, we would interpolate the velocity field onto this point, using both local velocities (colored in blue) and ghost cell velocities (colored in green). Then, we evaluate the IBM force from the mismatch between the interpolated velocity and the rigid body velocity. Next, we would spread this force onto just the local velocity field, indicated by the blue points. Finally, Processor 0 would also add this force to $\mathbf{F}_{IBM,p}$, the total IBM force acting on the particle, because this point is contained within its boundaries. Processor 1, on the other hand, would also interpolate the velocity field and evaluate the correction force for the same point using its ghost cells. Processor 1 would then spread the force onto its blue velocity nodes, but it would not add the force to $\mathbf{F}_{IBM,p}$ because the marker is not located within its boundaries.

The same procedure would be carried out for the lower red point in Figure B.1. Both processors would interpolate the velocity field from their respective blue and green points, evaluate the correction force, then spread the force onto their local blue velocity points. Processor 1 alone would then add the force to $\mathbf{F}_{IBM,p}$ because this point is located within its boundaries. This force is later added back onto Processor 0 when all these forces are reassimilated. This strategy thus ensures that the local velocity field is correctly modified by the Lagrangian markers and that the IBM force on the particle is not double-counted for markers at the boundary.

B.2 Particle communication

In order to move particles between processors and evaluate forces from collisions and the IBM, particles are moved within their lists in a systematic way, as shown in Figure B.2. In this section, a special font is used for variable and function names that are used within PARTIES. Shown is the perspective from Processor 0, where the left-hand column shows

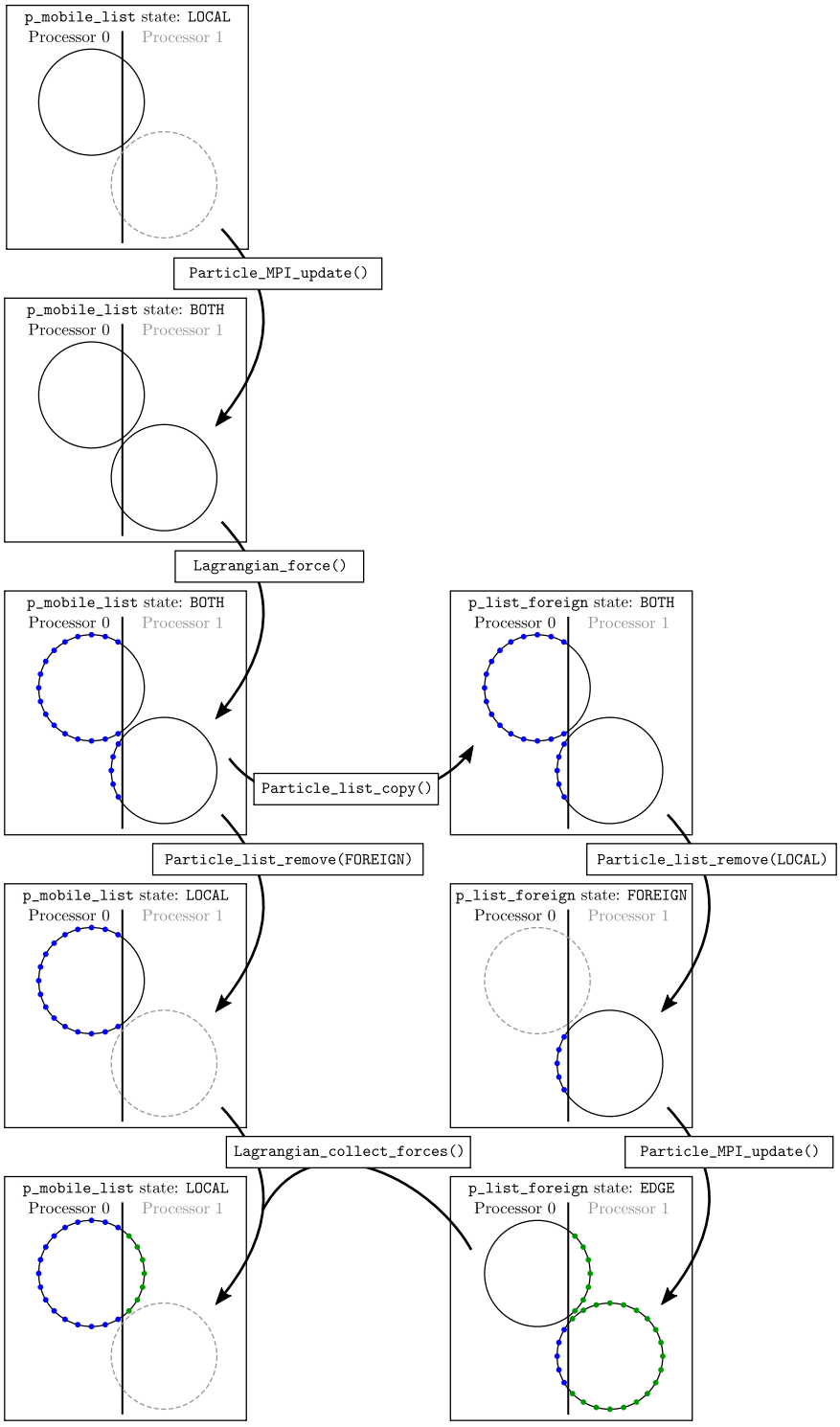

Figure B.2: Communication routine by which the total force from all Lagrangian markers acting on a particle is calculated, from the perspective of Processor 0.

the progress of the particle list `p_mobile_list`, while the right-hand column shows the progress of the foreign particle list `p_list_foreign`. Particles present within each list are colored black, while those that are absent are dashed gray. At first, only "local" particles are present on Processor 0, but a call to `Particle_MPI_update()` communicates "foreign," or neighboring, particles into the list. Calling `Lagrangian_force()` then evaluates the forces on the local markers, which are shown in blue, as explained in Appendix B.1. The mobile particle list is then separated into local and foreign lists, `p_mobile_list` and `p_list_foreign`, respectively, through calls to the functions `Particle_list_copy()` and `Particle_list_remove()`. Communicating the foreign list with `Particle_MPI_update()` then adds particles from Processor 1 to the list, where the forces on the green markers were evaluated. The function `Lagrangian_collect_forces()` then adds the green marker contributions to the blue marker contributions for the local particle. The result is that the total force acting on the top particle is evaluated on Processor 0. The same procedure is performed on Processor 1, where the total force is evaluated for the bottom particle.

B.3 Collisions

Collisions also require special treatment with multiple processors to ensure that they are evaluated for all cases of overlapping particles, but not double-counted. To prevent double-counting, we implemented collision ownership based on the point of contact. Consider the collisions between six particles shown in Figure B.3. If the contact point, indicated by the open circle at the intersection of two particles, is within a processor's boundaries, then it is responsible for calculating that collision. The different particle lists should all be checked: local-local, local-foreign, and foreign-foreign collisions are all possible. Processor 0 is responsible for all three collisions between the three particles in

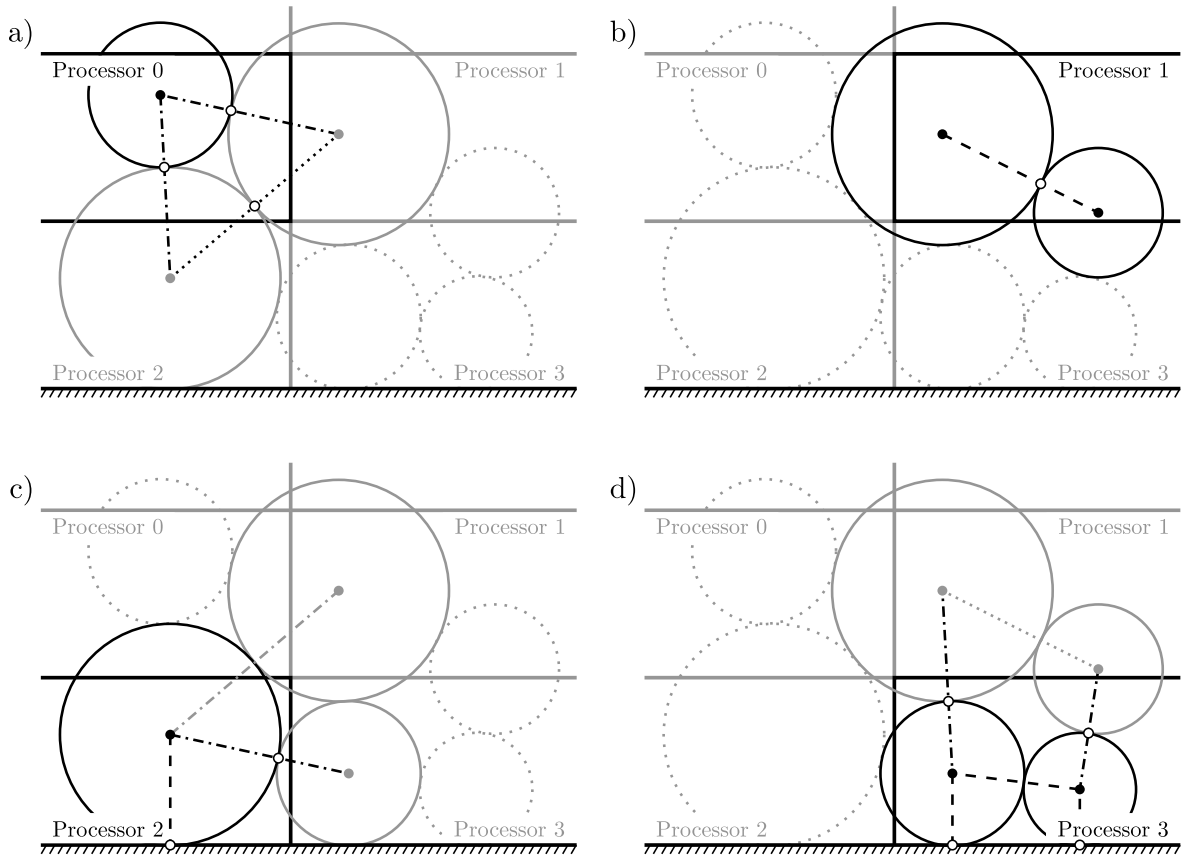

Figure B.3: Collision of a groups of particles from the perspective of (a) Processor 0, (b) Processor 1, (c) Processor 2, and (d) Processor 3. For the respective processors, black circles are local particles, gray circles are foreign particles, and dotted circles are unknown (non-communicated) particles. Black lines with open circles indicate collisions owned by the processor, while gray lines indicate possible collisions that were determined to be owned by another processor. Dashed lines indicate local-local collisions, dash-dot lines indicate local-foreign collisions, and dotted lines indicate foreign-foreign collisions.

the upper-left corner, which involve local-foreign and foreign-foreign collisions. Processor 1, meanwhile, is only responsible for a single local-local collision. Processors 2 and 3, on the other hand, are aware of other collisions occurring between particles in their lists, but have determined that they do not own all of those collisions. Wall collisions, however, only need to be evaluated for local particles.

Appendix C

Collision modeling

C.1 Definitions for particle-particle and particle-wall collisions

In order to discuss collisions in a general manner, we provide definitions for several variables that describe the contact. Some definitions will depend on whether the interaction is between particle p and a wall (particle-wall interaction, or P-W) or between particle p and particle q (particle-particle interaction, or P-P). For most of the definitions, collisions between a fixed particle and a mobile particle are handled identically to particle-particle collisions, unless indicated otherwise (particle-fixed, or P-F).

- R_{eff} – effective radius

$$R_{\mathit{eff}} = \frac{R_p\, R_q}{R_p + R_q} \qquad \text{(P-P)} \tag{C.1a}$$

$$R_{\mathit{eff}} = R_p \qquad \text{(P-W)} \tag{C.1b}$$

- m_{eff} – effective mass

$$m_{eff} = \frac{m_p\, m_q}{m_p + m_q} \qquad \text{(P-P)} \tag{C.2a}$$

$$m_{eff} = m_p \qquad \text{(P-W, P-F)} \tag{C.2b}$$

- $\mathbf{x}_w$ – point on wall closest to particle

- $\mathbf{n}$ – unit vector normal to the surface of contact, points from $\mathbf{x}_p$ to $\mathbf{x}_q$ (P-P) or directly towards the wall (P-W)

$$\mathbf{n} = \frac{\mathbf{x}_q - \mathbf{x}_p}{||\mathbf{x}_q - \mathbf{x}_p||} \qquad \text{(P-P)} \tag{C.3a}$$

$$\mathbf{n} = \frac{\mathbf{x}_w - \mathbf{x}_p}{||\mathbf{x}_w - \mathbf{x}_p||} \qquad \text{(P-W)} \tag{C.3b}$$

- ζ_n – distance between surfaces of the two bodies (negative value indicates overlap)

$$\zeta_n = ||\mathbf{x}_q - \mathbf{x}_p|| - R_p - R_q \qquad \text{(P-P)} \tag{C.4a}$$

$$\zeta_n = ||\mathbf{x}_w - \mathbf{x}_p|| - R_p \qquad \text{(P-W)} \tag{C.4b}$$

- $\mathbf{x}_{cp}$ – location of contact point between surfaces, halfway between surface overlap (P-P)

$$\mathbf{x}_{cp} = \mathbf{x}_p + \left(R_p + \frac{\zeta_n}{2}\right)\mathbf{n} \qquad \text{(P-P)} \tag{C.5a}$$

$$\mathbf{x}_{cp} = \mathbf{x}_w \qquad \text{(P-W)} \tag{C.5b}$$

- $R_{p,cp}$ – radius of particle p with respect to the contact point

$$R_{p,cp} = ||\mathbf{x}_{cp} - \mathbf{x}_p|| \tag{C.6}$$

- $\mathbf{g}$ – relative velocity between particle centers of mass

$$\mathbf{g} = \mathbf{u}_p - \mathbf{u}_q \qquad \text{(P-P)} \tag{C.7a}$$

$$\mathbf{g} = \mathbf{u}_p \qquad \text{(P-W)} \tag{C.7b}$$

- $\mathbf{g}_{cp}$ – relative velocity of surface contact point

$$\mathbf{g}_{cp} = \mathbf{g} + R_{p,cp}(\boldsymbol{\omega}_p \times \mathbf{n}) + R_{q,cp}(\boldsymbol{\omega}_q \times \mathbf{n}) \qquad \text{(P-P)} \tag{C.8a}$$

$$\mathbf{g}_{cp} = \mathbf{g} + R_{p,cp}(\boldsymbol{\omega}_p \times \mathbf{n}) \qquad \text{(P-W)} \tag{C.8b}$$

- $\mathbf{g}_{n,cp}$ – component of $\mathbf{g}_{cp}$ normal to surface

$$\mathbf{g}_{n,cp} = (\mathbf{g}_{cp} \cdot \mathbf{n})\mathbf{n} \tag{C.9}$$

- $\mathbf{g}_{t,cp}$ – component of $\mathbf{g}_{cp}$ tangent to surface

$$\mathbf{g}_{t,cp} = \mathbf{g}_{cp} - \mathbf{g}_{n,cp} \tag{C.10}$$

C.2 Calculating the normal contact model coefficients

In order to obtain the stiffness and damping coefficients k_n and d_n, Ray et al. [90] use nonlinear transformations and a series expansion of (4.7) to yield the following algebraic expressions:

$$\lambda = \frac{1}{\alpha^2 \tau_{c,0}^2} \left(-\frac{1}{2} C\eta + \sqrt{\frac{1}{4} C^2 \eta^2 + \alpha^2 \tau_{c,0}^2 \eta} \right), \tag{C.11a}$$

$$t_* = \frac{T_c}{\tau_{c,0}}\sqrt{1 - A\lambda - B\lambda^2}, \tag{C.11b}$$

$$d_n = \frac{2\lambda m_{\mathit{eff}}}{t_*}, \tag{C.11c}$$

and

$$k_n = \frac{m_{\mathit{eff}}}{\sqrt{u_{in} t_*^5}}, \tag{C.11d}$$

where $A = 0.716, B = 0.830$, $C = 0.744$, $\alpha = 1.111$, and $\tau_{c,0} = 3.218$ are constants. The parameter $\eta = (\ln e_{dry})^2$ accounts for the restitution coefficient, and we measure the impact velocity to be $u_{in} = \mathbf{g}_{n,cp} \cdot \mathbf{n}$ at the first occurrence of $\zeta_n \leq 0$.

C.3 The tangential displacement vector

Tangential models based on spring systems require a displacement as defined by (4.9), which represents the accumulated relative motion between two surfaces We calculate $\boldsymbol{\zeta}_t$ in a discrete sense as follows:

$$\widetilde{\boldsymbol{\zeta}}_t = \boldsymbol{\zeta}_t^{k-1} - \left(\boldsymbol{\zeta}_t^{k-1} \cdot \mathbf{n}\right)\mathbf{n} \tag{C.12a}$$

$$\widehat{\boldsymbol{\zeta}}_t = \frac{||\boldsymbol{\zeta}_t^{k-1}||}{||\widetilde{\boldsymbol{\zeta}}_t||}\widetilde{\boldsymbol{\zeta}}_t \tag{C.12b}$$

$$\boldsymbol{\zeta}_t^k = \widehat{\boldsymbol{\zeta}}_t + 2\alpha_k \Delta t\, \mathbf{g}_{t,cp}. \tag{C.12c}$$

Equations (C.12a) and (C.12b) rotate the displacement from the previous timestep onto a plane tangent to the two surfaces. Luding [95] implemented this rotation to account for the change in reference frame that can take place between two timesteps. Without this rotation, the linear spring could contribute to the normal force acting between two particles.

Furthermore, when the two surfaces slip according to the Coulomb friction criteria, the displacement vector should not grow as the two surfaces continue to slide past one another. Instead, we reset the displacement to that which achieves the Coulomb friction force:

$$\boldsymbol{\zeta}_t = -\frac{||\mu \mathbf{F}_n||\mathbf{t} + d_t \mathbf{g}_{t,cp}}{k_t} \qquad \text{if} \quad ||\mathbf{F}_{t,LS}|| > ||\mu \mathbf{F}_n||. \tag{C.13}$$

Bibliography

[1] E. Meiburg and B. Kneller, *Turbidity Currents and Their Deposits*, *Annual Review of Fluid Mechanics* **42** (jan, 2010) 135–156.

[2] G. Seminara, *Fluvial Sedimentary Patterns*, *Annual Review of Fluid Mechanics* **42** (jan, 2010) 43–66.

[3] J. P. Prancevic, M. P. Lamb, M. C. Palucis, and J. G. Venditti, *The Role of Three-Dimensional Boundary Stresses in Limiting the Occurrence and Size of Experimental Landslides*, *Journal of Geophysical Research: Earth Surface* **123** (jan, 2018) 46–65.

[4] P. Frey and M. Church, *Bedload: a granular phenomenon*, *Earth Surface Processes and Landforms* **36** (jan, 2011) 58–69.

[5] R. Maurin, J. Chauchat, and P. Frey, *Dense granular flow rheology in turbulent bedload transport*, *Journal of Fluid Mechanics* **804** (oct, 2016) 490–512.

[6] M. Houssais and D. J. Jerolmack, *Toward a unifying constitutive relation for sediment transport across environments*, *Geomorphology* **277** (jan, 2017) 251–264.

[7] M. Garcia and G. Parker, *Entrainment of bed sediment into suspension*, *Journal of Hydraulic Engineering* **117** (1991), no. 4 414–435.

[8] E. Lajeunesse, L. Malverti, and F. Charru, *Bed load transport in turbulent flow at the grain scale: Experiments and modeling*, *Journal of Geophysical Research* **115** (oct, 2010) F04001.

[9] L. C. van Rijn, *Sediment Transport, Part I: Bed Load Transport*, *Journal of Hydraulic Engineering* **110** (1984), no. 10 1431–1456.

[10] L. C. van Rijn, *Sediment Transport, Part II: Suspended Load Transport*, *Journal of Hydraulic Engineering* **110** (1984), no. 11 1613–1641.

[11] A. Shields, *Anwendung der Aehnlichkeitsmechanik und der Turbulenzforschung auf die Geschiebebewegung*, tech. rep., Soil Conservation Service, Pasadena, 1936.

[12] M. H. García, *Sediment Transport and Morphodynamics*, in *Sedimentation Engineering*, pp. 21–163. American Society of Civil Engineers, Reston, VA, may, 2008.

[13] J. M. Buffington and D. R. Montgomery, *A systematic analysis of eight decades of incipient motion studies, with special reference to gravel-bedded rivers*, *Water Resources Research* **33** (aug, 1997) 1993–2029.

[14] T.-J. Hsu, J. T. Jenkins, and P. L.-F. Liu, *On two-phase sediment transport: sheet flow of massive particles*, *Proceedings of the Royal Society A: Mathematical, Physical and Engineering Sciences* **460** (aug, 2004) 2223–2250.

[15] D. Berzi and L. Fraccarollo, *Intense sediment transport: Collisional to turbulent suspension*, *Physics of Fluids* **28** (feb, 2016) 023302.

[16] M. Ouriemi, P. Aussillous, and É. Guazzelli, *Sediment dynamics. Part 1. Bed-load transport by laminar shearing flows*, *Journal of Fluid Mechanics* **636** (sep, 2009) 295–319.

[17] L. A. E., A. V. Orpe, R. Molloy, A. Kudrolli, and D. H. Rothman, *Erosion of a granular bed driven by laminar fluid flow*, *Journal of Fluid Mechanics* **605** (jun, 2008) 47–58.

[18] J. A. Dijksman, E. Wandersman, S. Slotterback, C. R. Berardi, W. D. Updegraff, M. Van Hecke, and W. Losert, *From frictional to viscous behavior: Three-dimensional imaging and rheology of gravitational suspensions*, *Physical Review E - Statistical, Nonlinear, and Soft Matter Physics* **82** (2010), no. 6 2–5.

[19] P. Aussillous, J. Chauchat, M. Pailha, M. Médale, and É. Guazzelli, *Investigation of the mobile granular layer in bedload transport by laminar shearing flows*, *Journal of Fluid Mechanics* **736** (2013) 594–615.

[20] M. Houssais, C. P. Ortiz, D. J. Durian, and D. J. Jerolmack, *Rheology of sediment transported by a laminar flow*, *Physical Review E* **94** (dec, 2016) 062609.

[21] J. J. Stickel and R. L. Powell, *Fluid mechanics and rheology of dense suspensions*, *Annual Review of Fluid Mechanics* **37** (jan, 2005) 129–149.

[22] F. Boyer, É. Guazzelli, and O. Pouliquen, *Unifying suspension and granular rheology*, *Physical Review Letters* **107** (2011), no. 18 1–5.

[23] R. Seto, R. Mari, J. F. Morris, and M. M. Denn, *Discontinuous shear thickening of frictional hard-sphere suspensions*, *Physical Review Letters* **111** (2013), no. 21 1–5.

[24] E. DeGiuli, G. Düring, E. Lerner, and M. Wyart, *Unified theory of inertial granular flows and non-Brownian suspensions*, *Physical Review E* **91** (jun, 2015) 062206.

[25] R. Mari, R. Seto, J. F. Morris, and M. M. Denn, *Shear thickening, frictionless and frictional rheologies in non-Brownian suspensions*, *Journal of Rheology* **58** (2014), no. 6 32.

[26] A. Prosperetti, *Life and death by boundary conditions*, *Journal of Fluid Mechanics* **768** (2015) 1–4.

[27] R. Jain, B. Vowinckel, and J. Fröhlich, *Spanwise Particle Clusters in DNS of Sediment Transport Over a Regular and an Irregular Bed*, *Flow, Turbulence and Combustion* **99** (dec, 2017) 973–990.

[28] B. Vowinckel, T. Kempe, and J. Fröhlich, *Fluidparticle interaction in turbulent open channel flow with fully-resolved mobile beds*, *Advances in Water Resources* **72** (oct, 2014) 32–44.

[29] A. G. Kidanemariam and M. Uhlmann, *Interface-resolved direct numerical simulation of the erosion of a sediment bed sheared by laminar channel flow*, *International Journal of Multiphase Flow* **67** (dec, 2014) 174–188.

[30] S. Tschisgale, T. Kempe, and J. Fröhlich, *A non-iterative immersed boundary method for spherical particles of arbitrary density ratio*, *Journal of Computational Physics* **339** (jun, 2017) 432–452.

[31] T. Kempe and J. Fröhlich, *An improved immersed boundary method with direct forcing for the simulation of particle laden flows*, *Journal of Computational Physics* **231** (may, 2012) 3663–3684.

[32] M. Uhlmann, *An immersed boundary method with direct forcing for the simulation of particulate flows*, *Journal of Computational Physics* **209** (nov, 2005) 448–476.

[33] R. Glowinski, T. W. Pan, T. I. Hesla, and D. D. Joseph, *A distributed Lagrange multiplier/fictitious domain method for particulate flows*, *International Journal of Multiphase Flow* **25** (aug, 1999) 755–794.

[34] S. Takiguchi, T. Kajishima, and Y. Miyake, *Numerical scheme to resolve the interaction between solid particles and fluid turbulence*, *JSME International Journal Series B-Fluids and Thermal Engineering* **42** (1999), no. 3 411–418.

[35] N. Sharma and N. A. Patankar, *A fast computation technique for the direct numerical simulation of rigid particulate flows*, *Journal of Computational Physics* **205** (may, 2005) 439–457.

[36] S. V. Apte, M. Martin, and N. A. Patankar, *A numerical method for fully resolved simulation (FRS) of rigid particleflow interactions in complex flows*, *Journal of Computational Physics* **228** (may, 2009) 2712–2738.

[37] M. Vanella, A. Posa, and E. Balaras, *Adaptive Mesh Refinement for Immersed Boundary Methods*, *Journal of Fluids Engineering* **136** (feb, 2014) 040909.

[38] H. H. Hu, D. D. Joseph, and M. J. Crochet, *Direct simulation of fluid particle motions*, *Theoretical and Computational Fluid Dynamics* **3** (1992), no. 5 285–306.

[39] S. Haeri and J. S. Shrimpton, *On the application of immersed boundary, fictitious domain and body-conformal mesh methods to many particle multiphase flows*, *International Journal of Multiphase Flow* **40** (2012) 38–55.

[40] R. Mittal and G. Iaccarino, *Immersed boundary methods*, *Annual Review of Fluid Mechanics* **37** (jan, 2005) 239–261.

[41] N. A. Patankar, P. Singh, D. D. Joseph, R. Glowinski, and T. W. Pan, *A new formulation of the distributed Lagrange multiplier/fictitious domain method for particulate flows*, *International Journal of Multiphase Flow* **26** (sep, 2000) 1509–1524.

[42] S. V. Apte and J. R. Finn, *A variable-density fictitious domain method for particulate flows with broad range of particlefluid density ratios*, *Journal of Computational Physics* **243** (jun, 2013) 109–129.

[43] K. Taira and T. Colonius, *The immersed boundary method: A projection approach*, *Journal of Computational Physics* **225** (aug, 2007) 2118–2137.

[44] Z. Zhang and a. Prosperetti, *A Method for Particle Simulation*, *Journal of Applied Mechanics* **70** (2003), no. 1 64.

[45] Z. Zhang and A. Prosperetti, *A second-order method for three-dimensional particle simulation*, *Journal of Computational Physics* **210** (nov, 2005) 292–324.

[46] C. Peskin, *Flow patterns around heart valves: A numerical method*, *Journal of Computational Physics* **10** (1972), no. 2 252–271.

[47] J. Mohd-Yusof, *Combined Immersed-Boundary/B-spline methods for simulations of flow in complex geometries*, *Annual Research Briefs* (1997) 317–327.

[48] A. Mark and B. G. van Wachem, *Derivation and validation of a novel implicit second-order accurate immersed boundary method*, *Journal of Computational Physics* **227** (2008), no. 13 6660–6680.

[49] D. Kim and H. Choi, *Immersed boundary method for flow around an arbitrarily moving body*, *Journal of Computational Physics* **212** (2006), no. 2 662–680.

[50] W. P. Breugem, *A second-order accurate immersed boundary method for fully resolved simulations of particle-laden flows*, *Journal of Computational Physics* **231** (2012), no. 13 4469–4498.

[51] M. N. Ardekani, P. Costa, W. P. Breugem, and L. Brandt, *Numerical study of the sedimentation of spheroidal particles*, *International Journal of Multiphase Flow* **87** (2016) 16–34.

[52] G. Akiki and S. Balachandar, *Immersed boundary method with non-uniform distribution of Lagrangian markers for a non-uniform Eulerian mesh*, *Journal of Computational Physics* **307** (2016) 34–59.

[53] M. Mohan Rai and P. Moin, *Direct simulations of turbulent flow using finite-difference schemes*, *Journal of Computational Physics* **96** (sep, 1991) 15–53.

[54] A. Goza and T. Colonius, *A strongly-coupled immersed-boundary formulation for thin elastic structures*, *Journal of Computational Physics* **336** (may, 2017) 401–411.

[55] E. B. Saff and a. B. J. Kuijlaars, *Distributing many points on a sphere*, *The Mathematical Intelligencer* **19** (1997), no. 1 5–11.

[56] P. Leopardi, *A partition of the unit sphere into regions of equal area and small diameter*, *Electronic Transactions on Numerical Analysis* **25** (2006) 309–327.

[57] A. Roma, C. Peskin, and M. Berger, *An Adaptive Version of the Immersed Boundary Method*, *Journal of Computational Physics* **153** (1999), no. 2 509–534.

[58] T. Kempe and J. Fröhlich, *Collision modelling for the interface-resolved simulation of spherical particles in viscous fluids*, *Journal of Fluid Mechanics* **709** (oct, 2012) 445–489.

[59] N. Mordant and J. F. Pinton, *Velocity measurement of a settling sphere*, *The European Physical Journal B* **18** (2000), no. 2 343–352.

[60] A. ten Cate, C. H. Nieuwstad, J. J. Derksen, and H. E. a. Van den Akker, *Particle imaging velocimetry experiments and lattice-Boltzmann simulations on a single sphere settling under gravity*, *Physics of Fluids* **14** (2002), no. 11 4012–4025.

[61] P. P. Brown and D. F. Lawler, *Sphere Drag and Settling Velocity Revisited*, *Journal of Environmental Engineering* **129** (mar, 2003) 222–231.

[62] R. Natarajan and A. Acrivos, *The instability of the steady flow past spheres and disks*, *Journal of Fluid Mechanics* **254** (1993) 323–344.

[63] T. A. Johnson and V. C. Patel, *Flow past a sphere up to a Reynolds number of 300*, *Journal of Fluid Mechanics* **378** (jan, 1999) 19–70.

[64] J. J. Derksen, *Simulations of granular bed erosion due to laminar shear flow near the critical Shields number*, *Physics of Fluids* **23** (2011), no. 11.

[65] J. J. Derksen, *Simulations of granular bed erosion due to a mildly turbulent shear flow*, *Journal of Hydraulic Research* **53** (sep, 2015) 622–632.

[66] M. Uhlmann, *Interface-resolved direct numerical simulation of vertical particulate channel flow in the turbulent regime*, *Physics of Fluids* **20** (may, 2008) 053305.

[67] C. Santarelli and J. Fröhlich, *Direct Numerical Simulations of spherical bubbles in vertical turbulent channel flow*, *International Journal of Multiphase Flow* **75** (oct, 2015) 174–193.

[68] F. Lucci, A. Ferrante, and S. Elghobashi, *Modulation of isotropic turbulence by particles of Taylor length-scale size*, *Journal of Fluid Mechanics* **650** (may, 2010) 5.

[69] F. Picano, W. P. Breugem, and L. Brandt, *Turbulent channel flow of dense suspensions of neutrally buoyant spheres*, *Journal of Fluid Mechanics* **764** (2015) 463–487.

[70] S. Balachandar and J. K. Eaton, *Turbulent Dispersed Multiphase Flow*, *Annual Review of Fluid Mechanics* **42** (jan, 2010) 111–133.

[71] T. Kempe, B. Vowinckel, and J. Fröhlich, *On the relevance of collision modeling for interface-resolving simulations of sediment transport in open channel flow*, *International Journal of Multiphase Flow* **58** (jan, 2014) 214–235.

[72] R. Glowinski, T. W. Pan, T. I. Hesla, D. D. Joseph, and J. Périaux, *A Fictitious Domain Approach to the Direct Numerical Simulation of Incompressible Viscous Flow past Moving Rigid Bodies: Application to Particulate Flow*, *Journal of Computational Physics* **169** (2001), no. 2 363–426.

[73] J. D. Fenton and J. E. Abbott, *Initial movement of grains on a stream bed: the effect of relative protrusion*, *Proceedings of the Royal Society of London Series A* **352** (1977), no. 1671 523–537.

[74] Y. Niño and M. García, *Experiments on Saltation of Sand in Water*, *Journal of Hydraulic Engineering* **124** (oct, 1998) 1014–1025.

[75] X. Shao, T. Wu, and Z. Yu, *Fully resolved numerical simulation of particle-laden turbulent flow in a horizontal channel at a low Reynolds number*, *Journal of Fluid Mechanics* **693** (feb, 2012) 319–344.

[76] A. G. Kidanemariam, C. Chan-Braun, T. Doychev, and M. Uhlmann, *Direct numerical simulation of horizontal open channel flow with finite-size, heavy particles at low solid volume fraction*, *New Journal of Physics* **15** (2013) 0–42.

[77] G. G. Joseph, R. Zenit, M. L. Hunt, and A. M. Rosenwinkel, *Particle-wall collisions in a viscous fluid*, *Journal of Fluid Mechanics* **433** (2001) 329–346.

[78] J. A. Simeonov and J. Calantoni, *Modeling mechanical contact and lubrication in Direct Numerical Simulations of colliding particles*, *International Journal of Multiphase Flow* **46** (2012) 38–53.

[79] E. Izard, T. Bonometti, and L. Lacaze, *Modelling the dynamics of a sphere approaching and bouncing on a wall in a viscous fluid*, *Journal of Fluid Mechanics* **747** (2014) 422–446.

[80] P. Costa, B. J. Boersma, J. Westerweel, and W. P. Breugem, *Collision model for fully resolved simulations of flows laden with finite-size particles*, *Physical Review E - Statistical, Nonlinear, and Soft Matter Physics* **92** (2015), no. 5 1–14.

[81] A. J. Sierakowski and A. Prosperetti, *Resolved-particle simulation by the Physalis method: Enhancements and new capabilities*, *Journal of Computational Physics* **309** (2016) 164–184.

[82] P. Gondret, M. Lance, and L. Petit, *Bouncing motion of spherical particles in fluids*, *Physics of Fluids* **14** (2002), no. 2 643–652.

[83] H. P. Zhu, Z. Y. Zhou, R. Y. Yang, and a. B. Yu, *Discrete particle simulation of particulate systems: A review of major applications and findings*, *Chemical Engineering Science* **63** (2008), no. 23 5728–5770.

[84] S. Fukuoka, T. Fukuda, and T. Uchida, *Effects of sizes and shapes of gravel particles on sediment transports and bed variations in a numerical movable-bed channel*, *Advances in Water Resources* **72** (oct, 2014) 84–96.

[85] F. Charru, B. Andreotti, and P. Claudin, *Sand Ripples and Dunes*, *Annual Review of Fluid Mechanics* **45** (jan, 2013) 469–493.

[86] C. Thornton, S. J. Cummins, and P. W. Cleary, *An investigation of the comparative behaviour of alternative contact force models during inelastic collisions*, *Powder Technology* **233** (jan, 2013) 30–46.

[87] R. G. Cox and H. Brenner, *The slow motion of a sphere through a viscous fluid towards a plane surfaceII Small gap widths, including inertial effects*, *Chemical Engineering Science* **22** (dec, 1967) 1753–1777.

[88] H. Hertz, *Ueber die Verdunstung der Flüssigkeiten, insbesondere des Quecksilbers, im luftleeren Raume*, *Annalen der Physik* **253** (1882), no. 10 177–193.

[89] S. F. Foerster, M. Y. Louge, H. Chang, and K. Allia, *Measurements of the collision properties of small spheres*, *Physics of Fluids* **6** (1994), no. 3 1108.

[90] S. Ray, T. Kempe, and J. Fröhlich, *Efficient modelling of particle collisions using a non-linear viscoelastic contact force*, *International Journal of Multiphase Flow* **76** (feb, 2015) 101–110.

[91] C. Thornton, S. J. Cummins, and P. W. Cleary, *An investigation of the comparative behaviour of alternative contact force models during elastic collisions*, *Powder Technology* **210** (jul, 2011) 189–197.

[92] G. G. Joseph and M. L. Hunt, *Oblique particle-wall collisions in a liquid*, *Journal of Fluid Mechanics* **510** (2004) 71–93.

[93] B. Vowinckel, R. Jain, T. Kempe, and J. Fröhlich, *Entrainment of single particles in a turbulent open-channel flow: a numerical study*, *Journal of Hydraulic Research* **54** (mar, 2016) 158–171.

[94] P. M. Fishbane, S. Gasiorowicz, and S. T. Thornton, *Physics for scientists and engineers*. Pearson College Division, 1996.

[95] S. Luding, *Cohesive, frictional powders: contact models for tension*, *Granular Matter* **10** (mar, 2008) 235–246.

[96] J. H. Dieterich, *Time-dependent friction in rocks*, *Journal of Geophysical Research* **77** (jul, 1972) 3690–3697.

[97] B. Allen and A. Kudrolli, *Depth resolved granular transport driven by shearing fluid flow*, *Physical Review Fluids* **2** (feb, 2017) 024304.

[98] H. Capart and L. Fraccarollo, *Transport layer structure in intense bed-load*, *Geophysical Research Letters* **38** (oct, 2011).

[99] A. H. Clark, M. D. Shattuck, N. T. Ouellette, and C. S. O'Hern, *Onset and cessation of motion in hydrodynamically sheared granular beds*, *Physical Review E - Statistical, Nonlinear, and Soft Matter Physics* **92** (2015), no. 4 1–7.

[100] H. P. Zhu and A. B. Yu, *Averaging method of granular materials*, *Physical Review E - Statistical, Nonlinear, and Soft Matter Physics* **66** (2002), no. 2 1–10.

[101] I. Goldhirsch, *Stress, stress asymmetry and couple stress: From discrete particles to continuous fields*, *Granular Matter* **12** (2010), no. 3 239–252.

[102] T. Weinhart, A. R. Thornton, S. Luding, and O. Bokhove, *From discrete particles to continuum fields near a boundary*, *Granular Matter* **14** (2012), no. 2 289–294.

[103] T. Weinhart, R. Hartkamp, A. R. Thornton, and S. Luding, *Coarse-grained local and objective continuum description of three-dimensional granular flows down an inclined surface*, *Physics of Fluids* **25** (2013), no. 7.

[104] P. R. Nott, E. Guazzelli, and O. Pouliquen, *The suspension balance model revisited*, *Physics of Fluids* **23** (apr, 2011) 043304.

[105] T. Weinhart, S. Luding, and A. R. Thornton, *From discrete particles to continuum fields in mixtures*, *AIP Conference Proceedings* **1542** (2013) 1202–1205.

[106] R. Sun and H. Xiao, *Diffusion-based coarse graining in hybrid continuum-discrete solvers: Theoretical formulation and a priori tests*, *International Journal of Multiphase Flow* **77** (2015) 142–157.

[107] M. M. Denn and J. F. Morris, *Rheology of Non-Brownian Suspensions*, *Annual Review of Chemical and Biomolecular Engineering* **5** (jun, 2014) 203–228.

[108] Q. Zhang and A. Prosperetti, *Physics-based analysis of the hydrodynamic stress in a fluid-particle system*, *Physics of Fluids* **22** (mar, 2010) 033306.

[109] B. Vowinckel, V. Nikora, T. Kempe, and J. Fröhlich, *Momentum balance in flows over mobile granular beds: application of double-averaging methodology to DNS data*, *Journal of Hydraulic Research* **55** (mar, 2017) 190–207.

[110] B. Vowinckel, V. Nikora, T. Kempe, and J. Fröhlich, *Spatially-averaged momentum fluxes and stresses in flows over mobile granular beds: a DNS-based study*, *Journal of Hydraulic Research* **55** (mar, 2017) 208–223.

[111] V. Nikora, F. Ballio, S. Coleman, and D. Pokrajac, *Spatially Averaged Flows over Mobile Rough Beds: Definitions, Averaging Theorems, and Conservation Equations*, *Journal of Hydraulic Engineering* **139** (2013), no. 8 803–811.

[112] A. G. Kidanemariam and M. Uhlmann, *Formation of sediment patterns in channel flow: minimal unstable systems and their temporal evolution*, *Journal of Fluid Mechanics* **818** (may, 2017) 716–743.

[113] A. Einstein, *Investigations on the Theory of the Brownian Movement*. Dover, New York, 1956.

[114] G. K. Batchelor, *Sedimentation in a dilute dispersion of spheres*, *Journal of Fluid Mechanics* **52** (mar, 1972) 245–268.

[115] G. K. Batchelor, *The effect of Brownian motion on the bulk stress in a suspension of spherical particles*, *Journal of Fluid Mechanics* **83** (nov, 1977) 97.

[116] J. T. Jenkins and S. B. Savage, *A theory for the rapid flow of identical, smooth, nearly elastic, spherical particles*, *Journal of Fluid Mechanics* **130** (may, 1983) 187.

[117] D. Berzi and L. Fraccarollo, *Inclined, collisional sediment transport*, *Physics of Fluids* **25** (oct, 2013) 106601.

[118] H. Eilers, *Die Viskositäts-Konzentrationsabhängigkeit kolloider Systeme in organischen Lösungsmitteln*, *Kolloid-Zeitschrift* **102** (feb, 1943) 154–169.

[119] M. Mooney, *The viscosity of a concentrated suspension of spherical particles*, *Journal of Colloid Science* **6** (apr, 1951) 162–170.

[120] I. M. Krieger and T. J. Dougherty, *A Mechanism for NonNewtonian Flow in Suspensions of Rigid Spheres*, *Transactions of the Society of Rheology* **3** (mar, 1959) 137–152.

[121] J. F. Morris and F. Boulay, *Curvilinear flows of noncolloidal suspensions: The role of normal stresses*, *Journal of Rheology* **43** (sep, 1999) 1213–1237.

[122] E. DeGiuli, J. N. McElwaine, and M. Wyart, *Phase diagram for inertial granular flows*, *Physical Review E* **94** (jul, 2016) 012904.

[123] Y. Forterre and O. Pouliquen, *Flows of Dense Granular Media*, *Annual Review of Fluid Mechanics* **40** (jan, 2008) 1–24.

[124] P. Jop, Y. Forterre, and O. Pouliquen, *A constitutive law for dense granular flows*, *Nature* **441** (2006), no. 7094 727–730.

[125] GDR Midi, *On dense granular flows*, *European Physical Journal E* **14** (2004), no. 4 314–365.

[126] C. Cassar, M. Nicolas, and O. Pouliquen, *Submarine granular flows down inclined planes*, *Physics of Fluids* **17** (2005), no. 10 103301.

[127] M. Trulsson, B. Andreotti, and P. Claudin, *Transition from the Viscous to Inertial Regime in Dense Suspensions*, *Physical Review Letters* **109** (sep, 2012) 118305.

[128] N. Frankel and A. Acrivos, *On the viscosity of a concentrated suspension of solid spheres*, *Chemical Engineering Science* **22** (jun, 1967) 847–853.

[129] R. J. Phillips, R. C. Armstrong, R. A. Brown, A. L. Graham, and J. R. Abbott, *A constitutive equation for concentrated suspensions that accounts for shearinduced particle migration*, *Physics of Fluids A: Fluid Dynamics* **4** (jan, 1992) 30–40.

[130] S. Dagois-Bohy, S. Hormozi, É. Guazzelli, and O. Pouliquen, *Rheology of dense suspensions of non-colloidal spheres in yield-stress fluids*, *Journal of Fluid Mechanics* **776** (aug, 2015) R2.